Systematics of the Electric Dipole Response in Stable Tin Isotopes

Systematik der elektrischen Dipolanregung in stabilen Zinnisotopen

Zur Erlangung des Grades eines Doktors der Naturwissenschaften (Dr. rer. nat.)
genehmigte Dissertation von M.Sc. Sergej Bassauer aus Sergejewka, Kasachstan
Tag der Einreichung: 16.10.2019, Tag der Prüfung: 02.12.2019
Darmstadt — D 17

1. Gutachten: Prof. Dr. Peter von Neumann-Cosel
2. Gutachten: Prof. Dr. Thomas Aumann

TECHNISCHE UNIVERSITÄT DARMSTADT

Fachbereich Physik
Institut für Kernphysik

Supported by the DFG within SFB 1245.

Systematics of the Electric Dipole Response in Stable Tin Isotopes
Systematik der elektrischen Dipolanregung in stabilen Zinnisotopen

Genehmigte Dissertation von M.Sc. Sergej Bassauer aus Sergejewka, Kasachstan

1. Gutachten: Prof. Dr. Peter von Neumann-Cosel
2. Gutachten: Prof. Dr. Thomas Aumann

Tag der Einreichung: 16.10.2019
Tag der Prüfung: 02.12.2019

Darmstadt — D 17

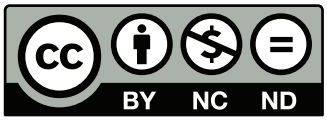

Erklärung gemäß §9 Promotionsordnung

Hiermit versichere ich, dass ich die vorliegende Dissertation selbstständig angefertigt und keine anderen als die angegebenen Quellen und Hilfsmittel verwendet habe. Alle wörtlichen und paraphrasierten Zitate wurden angemessen kenntlich gemacht. Die Arbeit hat bisher noch nicht zu Prüfungszwecken gedient.

Darmstadt, den 16. Oktober 2019

Sergej Bassauer

Dans la vie, rien n'est à craindre, tout est à comprendre.

Marie Skłodowska Curie

Abstract

The present thesis reports on the systematics of the electric dipole response in stable even mass tin isotopes. Inelastic proton scattering experiments were performed at the Research Center for Nuclear Physics (RCNP) in Osaka, Japan. Using a 295 MeV proton beam, scattered protons were detected under spectrometer angles of 0°, 2.5° and 4.5°. In two experimental campaigns data were taken in an excitation energy region of $5 - 26$ MeV.

Double differential cross sections were determined and by means of a multipole decomposition analysis the main contributions, namely E1 and M1, were extracted. In order to determine the electric dipole strength, the obtained double differential cross sections were converted to photoabsorption cross sections using the equivalent photon method. The photoabsorption cross sections are in fair agreement with (γ,x) results around the maximum of the giant dipole resonance. However, deviations towards the neutron threshold were observed. The most recent (γ,n) data, available for ^{116,118,120,124}Sn, are in a good agreement with results obtained in this work.

B(E1) strength distributions were determined and compared to available data from nuclear resonance fluorescence experiments for ^{112,116,124}Sn, below the neutron threshold. The present results show considerably more strength, confirming previous findings for ^{120}Sn. Furthermore, an accumulation of strength is found around 6.5 MeV, which is also observed in experiments with isoscalar probes.

The dipole polarisability in even-even stable tin isotopes $^{112-120,124}$Sn was extracted. The polarisability of ^{120}Sn was found to be lower than in a previous work, but compatible within the uncertainties, if corrected for the quasideuteron effect. Some of the model calculations based on the nuclear energy density functional theory able to reproduce the polarisability of ^{120}Sn are not compatible with the new value. A systematic comparison to one of the model calculations was carried out for different parametrisations of the symmetry energy parameters.

Using the so-called unit cross section technique electromagnetic B(M1) strength distributions and features of the spin M1 resonance are provided for the first time for stable even-even tin isotopes $^{112-120,124}$Sn.

The total gamma strength function was determined including E1 and M1 contributions. In the giant dipole resonance region fair agreement with photoabsorption experiments is found. In the pygmy dipole resonance region data on ^{116}Sn and ^{118}Sn are available from (^{3}He,^{3}He'γ) and (^{3}He,$\alpha\gamma$) experiments. Results for ^{116}Sn are in excellent agreement. In ^{118}Sn good agreement is found within the uncertainties. However, a prominent peak is found in all isotopes around 6.5 MeV which is not seen in (^{3}He,^{3}He'γ) and (^{3}He,$\alpha\gamma$) experiments, indicating a possible violation of the Brink-Axel hypothesis.

Finally, using a fluctuation analysis, level densities were extracted for ^{124}Sn in an excitation energy region of $6 - 15\,\mathrm{MeV}$ for 1^- states. These level densities were converted to the total level density and compared to results from (^{3}He,^{3}He$'\gamma$) and (^{3}He,$\alpha\gamma$) experiments, where level densities for ^{116,118,122}Sn are available. A fair agreement between these level densities is found.

Zusammenfassung

Die vorliegende Arbeit beschäftigt sich mit der Systematik der elektrischen Dipolstärke in stabilen Zinnisotopen gerader Massenzahl. Inelastische Protonenstreuexperimente wurden am Research Center for Nuclear Physics (RCNP) in Osaka, Japan durchgeführt. Mit Hilfe eines 295 MeV-Protonenstrahls wurden gestreute Protonen unter Spektrometerwinkeln von 0°, 2,5° und 4,5° gemessen. In zwei Experimentierkampagnen wurden Daten in einem Anregungsenergiebereich von $5 - 26$ MeV aufgenommen.

Doppelt differentielle Wirkungsquerschnitte wurden bestimmt und mit Hilfe einer Multipolentfaltung wurden die Hauptbeiträge, E1 und M1, extrahiert. Um die Dipolstärke zu bestimmen, wurden die erhaltenen doppelt differentiellen Wirkungsquerschnitte unter Benutzung der äquivalenten Photonenmethode in Photoabsorptionsquerschnitte konvertiert. Die so bestimmten Photoabsorptionsquerschnitte sind in guter Übereinstimmung mit Ergebnissen aus (γ,x)-Experimenten im Bereich des Maximums der Riesenresonanz. Abweichungen werden jedoch im Bereich der Neutronenschwelle beobachtet. Die kürzlich gemessenen Wirkungsquerschnitte aus (γ,n)-Experimenten für ^{116,118,120,124}Sn sind in guter Übereinstimmung mit Ergebnissen aus dieser Arbeit.

B(E1)-Stärkeverteilungen wurden bestimmt und mit verfügbaren Daten aus Kernresonanzfluoreszensexperimenten für ^{112,116,124}Sn verglichen. Unter der Neutronenschwelle wurde deutlich mehr Stärke in Experimenten mit inelastischer Protonenstreuung gesehen, was frühere Ergebnisse für ^{120}Sn bestätigt. Des Weiteren wurde in allen Isotopen eine Ansammlung von Stärke um 6,5 MeV gefunden, welche auch in Experimenten mit isoskalaren Proben beobachtet wird.

Die Dipolpolarisierbarkeit wurde in stabilen gerade-gerade Zinnisotopen $^{112-120,124}$Sn bestimmt. Die Polarisierbarkeit für ^{120}Sn ist kleiner als in einer vorherigen Arbeit, jedoch kompatibel innerhalb der Unsicherheiten nach einer Korrektur des Quasideuteroneffekts. Einige der Modellrechnungen, die im Stande waren Polarisierbarkeitsdaten in schweren Kernen systematisch zu reproduzieren sind inkompatibel mit dem neuen Wert für ^{120}Sn. Ein systematischer Vergleich mit einer der Modellrechnungen mit unterschiedlichen Parametrisierungen der Symmetrieenergieparameter wurde durchgeführt.

Unter der Verwendung der sogenannten Einheitsquerschnittmethode wurden die elektromagnetischen B(M1)-Stärkeverteilungen und Charakteristiken der Spin-M1-Resonanz zum ersten mal für die stabilen gerade-gerade Zinnisotope $^{112-120,124}$Sn bestimmt.

Die totale Gammastärkefunktion inklusive E1- und M1-Beiträgen wurde aus den Stärkeverteilungen bestimmt. Im Riesenresonanzbereich gibt es hierbei gute Übereinstimmungen mit Photoabsorptionsexperimenten. Im Bereich der Pygmyresonanz sind auch Daten für ^{116}Sn und

^{118}Sn aus (^{3}He,^{3}He'γ)- und (^{3}He,$\alpha\gamma$)-Experimenten verfügbar. Ergebnisse für ^{116}Sn sind in einer exzellenten Übereinstimmung. In ^{118}Sn wurde im Rahmen der Unsicherheiten eine gute Übereinstimmung gefunden. Jedoch wurde ein prominenter Peak in allen Isotopen um die 6,5 MeV gefunden, der nicht in (^{3}He,^{3}He'γ)- und (^{3}He,$\alpha\gamma$)-Experimenten gesehen wird. Dies könnte auf eine Verletzung der Brink-Axel-Hypothese hinweisen.

Schließlich wurden Zustandsdichten mit Hilfe einer Fluktuationsanalyse für ^{124}Sn in einem Energiebereich von $6 - 15$ MeV für 1^- Zustände extrahiert. Diese Zustandsdichten wurden dann in totale Zustandsdichten umgerechnet und mit Ergebnissen aus (^{3}He,^{3}He'γ)- und (^{3}He,$\alpha\gamma$)-Experimenten, für Zustandsdichten in ^{116,118,122}Sn verglichen. Hierbei wurde eine gute Übereinstimmung beobachtet.

Contents

List of Figures

List of Tables

1 Introduction

The electric dipole response is a fundamental observable to understand properties of nuclei. In Fig. 1.1 a schematic overview of a typical dipole response in medium and heavy mass nuclei near shell closure is shown. Up to the neutron threshold discrete states are excited and distinct peaks in the energy excitation spectrum can be observed. First collective phenomena emerge already at an excitation energy of a few MeV, namely a two-phonon state, which can be interpreted as the coupling of collective surface vibrations [1]. Around the neutron threshold one encounters the pygmy dipole resonance (PDR) [2], which is usually thought of as an oscillation of the neutron skin against an isospin saturated core. However, the true nature of the PDR is still under discussion [3, 4]. At even higher energies the electric dipole response is dominated by the giant dipole resonance (GDR) [5], which is described as an oscillation of neutrons against protons. Traditionally, the low-energy region below the neutron threshold is investigated via nuclear resonance fluorescence experiments (NRF), while the high-energy region above the neutron threshold can be accessed by photoabsorption experiments. In this work, inelastic proton scattering experiments under small scattering angles including 0° are used [6, 7]. Inelastic proton scattering has a great advantage as it can cover both, the PDR and the GDR regions at the same time, so that these excitation modes can be measured simultaneously in one experimental campaign. Furthermore, the PDR and GDR are measured with comparable uncertainties.

What can be learned from the electric dipole response in the tin isotope chain? The tin isotope chain is particularly suited for a systematic study of the dependence of the electric dipole response on neutron excess as it provides a wide mass range of accessible isotopes with little change of the underlying structure. Measurement and precise knowledge of the electric dipole response can contribute to a better understanding of several physical questions. Physical quantities, such as the reduced transition probability $B(E1)$, the dipole polarisability α_D, the gamma strength function $f(E_x)$ and the nuclear level density $\rho(E_x)$ can all be derived from the electric dipole response. In the following, the role of these observables within a greater physical context will be discussed.

The reduced transition probability, often also referred to as transition strength, contains information concerning the structure of a nucleus. The low-energy electric dipole strength became a hot topic of research in recent years aiming to unveil the true nature of the PDR [8]. Furthermore, dipole strength in the vicinity of the neutron threshold may lead to significant changes of neutron capture rates in the astrophysical r-process [9–11]. In order to test the picture of the PDR as an oscillation of a neutron skin against an isospin saturated core, systematic studies on nuclei with increasing neutron number such as the tin isotope chain are advanta-

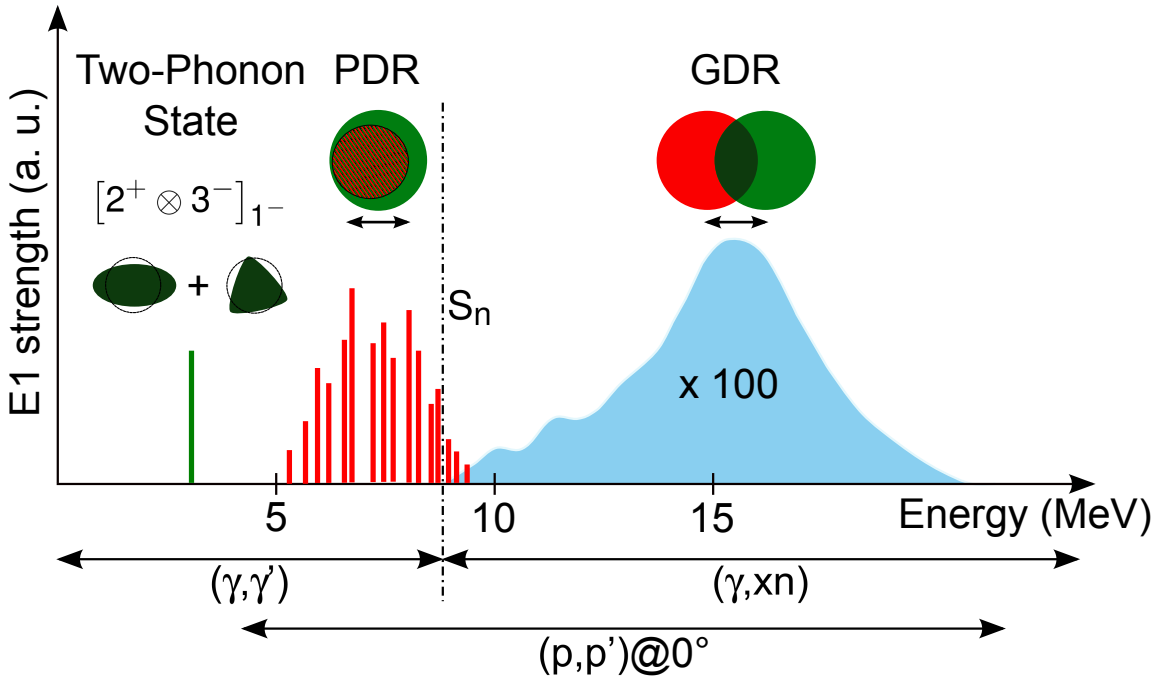

Figure 1.1: Schematic overview of the dipole response in medium and heavy mass nuclei near shell closure.

geous. In Fig. 1.2 a model calculation for several tin isotopes is shown which illustrates the behaviour of the low-energy strength with increasing neutron number. The fraction of the energy weighted sum rule (EWSR) contained in the low-energy region ($5-10\,\mathrm{MeV}$) relative to that in the high-energy region ($10-25\,\mathrm{MeV}$) is plotted against the neutron skin. One can see that the PDR contribution increases gradually with increasing neutron number until it saturates around ^{120}Sn. Other systematic studies for the tin isotope chain were undertaken in Refs. [13–15].

Another phenomenon discovered recently is the splitting of the PDR, which can be observed by comparing experiments conducted with isoscalar and isovector probes [16–19]. While in experiments using isovector probes the strength below the neutron threshold is broadly distributed, in experiments using isoscalar probes only a part of the strength is found up to a certain excitation energy depending on the nucleus. Beyond this excitation energy, isoscalar dipole excitations seem to be suppressed. Hence, the low-lying part of the E1 strength appears to be of mixed isoscalar/isovector nature stemming from a neutron oscillation on the surface of the nucleus, whereas the higher lying dipole transitions seemingly belong to a transitional region on the tail of the isovector giant dipole resonance.

The dipole polarisability is a crucial quantity as it allows to extract important constraints on neutron skin thickness [12, 13, 20–22] in heavy nuclei and parameters of the symmetry energy [20, 23–25]. The latter, determines the properties of the equation of state (EoS) in neutron-rich matter governing the structure of neutron stars as well as the collapse and explosion of giant stars in a supernova [26]. The observation of gravitational waves from merging neutron

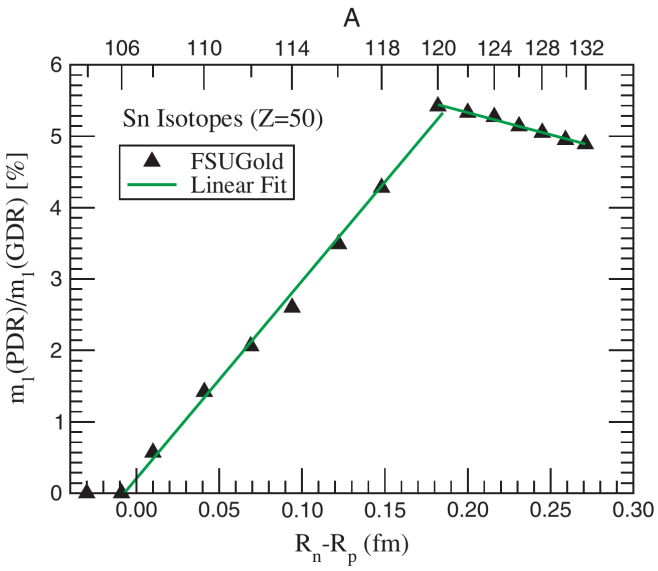

Figure 1.2: Fraction of the energy weighted sum rule contained in the low-energy region relative to that in the high-energy region as a function of the neutron skin of the various tin isotopes [12].

stars [27] provided new experimental constraints on the EoS of neutron-rich matter at high density. In Refs. [24, 28] a mass-radius relation for the observed neutron star mergers was derived and constraints on the neutron skin of ^{208}Pb [24]. The EoS therefore plays a crucial role in understanding phenomena in both nuclear physics and astrophysics.

The EoS is given for the lowest order of expansion by the following equation [29]

$$E(\rho,\delta) = E(\rho) + S(\rho)\delta^2 + \mathcal{O}(\delta^4), \tag{1.1}$$

where ρ is the sum of proton ρ_p and neutron ρ_n densities and $\delta = (\rho_p - \rho_n)/\rho$ is the asymmetry. The first term $E(\rho)$ corresponds to the EoS of symmetric nuclear matter and can be well constrained from the ground-state properties of finite nuclei, but also from the incompressibility of nuclear matter, which is proportional to the curvature of the symmetric nuclear matter EoS. The incompressibility can be derived from isoscalar giant monopole and dipole resonances [29]. The second term of the EoS is the so-called symmetry energy and can be written as [29]

$$S(\rho) = J + \frac{(\rho-\rho_0)}{3\rho_0}L + \mathcal{O}((\rho-\rho_0)^2), \tag{1.2}$$

where ρ_0 denotes the saturation density, i.e. the nuclear density in the interior of a nucleus. The symmetry energy is determined basically by two parameters, namely J and L. Thus to obtain a reliable parametrisation of the symmetry energy, one needs to constrain these parameters. In Fig. 1.3 a correlation between different observables is shown as predicted by an energy density

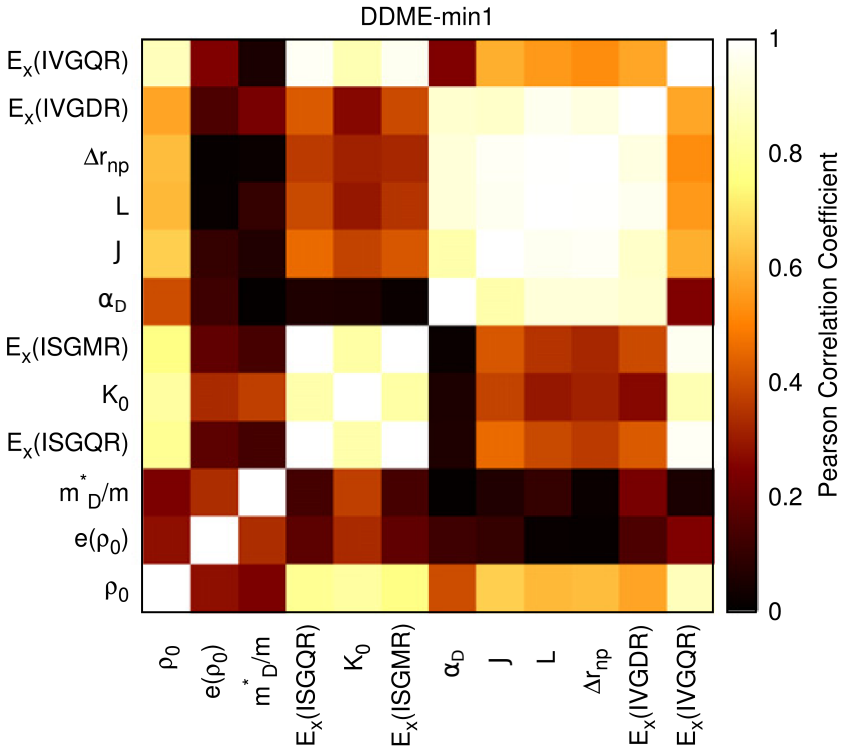

Figure 1.3: Correlation between different observables for finite nuclei and EoS parameters as predicted by the DDME-min1 energy density functional [30, 31].

functional (EDF). One can see that the parameters J and L are highly correlated to the neutron skin Δr_{pn} and the dipole polarisability α_D as well as the centroid energy of the isovector giant dipole resonance. Although these correlations are shown for a specific model (DDME-min1), these results are of general validity. However, absolute values can differ considerably for different models. Hence, a systematic comparison of the experimental dipole polarisabilities for many nuclei with model calculations is important to constrain J and L. First attempt to do so was undertaken in Ref. [32] using presently available α_D values for ^{68}Ni, ^{120}Sn and ^{208}Pb.

Besides the dominant E1 excitations, inelastic proton scattering experiments discussed in this work can also excite the isovector spin M1 (IVSM1) mode. The IVSM1 is a fundamental excitation mode of nuclei [33]. It is important for the description of neutral-current neutrino interactions in supernovae [34, 35], for modelling of reaction cross sections in large-scale nucleosynthesis network calculations [36] and the evolution of single-particle properties leading to shell closures in neutron-rich nuclei [37]. The precise knowledge of the IVSM1 contributes also to the solution of the so-called quenching problem, which describes the observation that the experimentally found isovector spin response, i.e Gamow-Teller and the isospin-analogue IVSM1 strength is systematically smaller than all model predictions [38]. Understanding of the quenching problem is a prerequisite for reliable calculations of nuclear matrix elements

needed e.g. to determine absolute neutrino masses from a positive neutrinoless double beta decay experiment [39].

Another physical quantity which can be extracted from knowledge of the electric and magnetic dipole response is the gamma strength function (GSF) [40]. In general, GSF is the distribution of the average reduced width for transitions summed over all particular multipole types as a function of gamma energy. GSFs serve as input in calculations of cross sections in astrophysics [41], reactor design [42] and waste transmutation [43] within statistical model reaction cross section calculations. The systematics of the low-energy GSFs in the tin isotopes allow an important test of the generalised Brink-Axel hypothesis [44, 45], which states that the GSF is independent of the properties of the initial and final states. Although there is strong evidence for E1 [46–50] and M1 [48, 51, 52] transitions which question the validity of the Brink-Axel hypothesis, it is still widely used for the derivation of GSFs not only in the GDR but also in the low-energy region, where the GSF is affected by excitation modes such as the pygmy dipole resonance [2, 8], the M1 scissors mode in deformed nuclei [53], or the spin M1 resonance [33].

Using a fluctuation analysis [54, 55], nuclear level densities (NLD) can be determined from the present high-resolution data in the PDR and GDR regions. This method allows to extract level densities in a model independent way by analysing cross section fluctuations in the excitation spectra. In the excitation energy regions investigated in this work, data on level densities are virtually non-existing in the literature. Therefore, results on level densities obtained in this work are an important test for commonly used level density models. Furthermore, they also provide an independent test of basic assumptions underlying the so-called Oslo method [56], where only the product of GSF and NLD can be determined.

This thesis is structured in the following way. In Chapter 2, theoretical concepts are presented which are essential for the proper understanding and interpretation of the experimental data. In Chapter 3 the experimental facility is introduced where the experiments discussed in this work were carried out. The experimental set-up as well as the technique are described and technical details concerning the used spectrometers and detectors are provided. Details on the used targets and on the conduction of the experiments are also given. In Chapter 4, the main steps of the data analysis are presented and particularly crucial aspects of the analysis are pointed out. The obtained cross sections are presented in Chapter 5 and a method to decompose them into individual E1, M1 and other contributions is illustrated. B(E1)/B(M1) strength distributions are extracted in Chapter 6 and results on the dipole polarisability, gamma strength function and nuclear level density as well as their comparison to results from different experiments are discussed. Finally, a summary and an outlook on future prospects is given in Chapter 7.

2 Theoretical considerations

In this chapter theoretical models and concepts will be introduced, which are required for the analysis and interpretation of the inelastic proton scattering data discussed in this work. Unless stated otherwise commonly used physical quantities are defined as shown in Tab. 2.1.

Table 2.1: Nomenclature for commonly used physical quantities.

c	Speed of light in vacuum
e	Elementary charge
$\hbar$	Reduced Planck constant
k	Wave number
α	Fine structure constant
β	Speed in units of c
γ	Lorentz factor
μ	Reduced mass

2.1 Inelastic proton scattering

The experiments discussed in this work were performed using inelastic proton scattering. In inelastic proton scattering the projectile can interact with the target nucleus mainly via two different processes, by nucleon-nucleon or by Coulomb interaction. In the (p,p') experiments examined in this work, the former is uniquely responsible for spin-flip excitations, while the latter is dominant under extreme forward angles and induces electromagnetic excitations. In the following subsections the scattering formalism for inelastic proton scattering will be briefly described based on Refs. [57–59].

2.1.1 Nucleon-nucleon interaction

The nucleon-nucleon interaction can be described by a time independent Schrödinger equation

$$(H_0 + V)\psi = E\psi, \tag{2.1}$$

where H_0 describes the unperturbed system, V the nucleon-nucleon interaction and E the energy in the center of mass frame. The eigenfunction ψ is given by the Lippmann-Schwinger equation

$$\psi^{\pm} = \phi^{\pm} + G_0^{\pm} V \psi^{\pm}, \tag{2.2}$$

with the Green's function

$$G_0^{\pm} = \frac{1}{E - H_0 \pm i\epsilon}, \tag{2.3}$$

where $\phi^{\pm}$ is the eigenfunction of the unperturbed system and $\pm$ denote the incoming and outgoing waves, respectively. The transition probability between perturbed and unperturbed states is given by the transition operator

$$T^{\pm} = V + VG_0^{\pm}T^{\pm}. \tag{2.4}$$

The transition operator can be expanded in a series as follows

$$T^{\pm} = V + VG_0^{\pm}V + VG_0^{\pm}VG_0^{\pm}V + \cdots. \tag{2.5}$$

By taking into account the first n terms one obtains the so-called Born approximation of n-th order. The physical meaning is that only n scattering processes are taken into account. In the case of $n = 1$ multiple scattering is not considered. The transition operator is related to the differential cross section in the following way

$$\frac{\mathrm{d}\sigma}{\mathrm{d}\Omega}(\vec{k}_i, \vec{k}_f) = \frac{\mu_i \mu_f}{(2\pi\hbar^2)^2} \frac{|\vec{k}_f|}{|\vec{k}_i|} |T(\vec{k}_f, \vec{k}_i)|^2, \tag{2.6}$$

with the momentum $\vec{k}$ and the reduced mass μ before (i) and after (f) the scattering process, respectively.

So far, the distortion of the outgoing waves after the scattering was neglected. However, in the vicinity of the nucleus incoming and outgoing waves are usually distorted by the nuclear mean field. To account for this, the distorted wave born approximation (DWBA) should be used. Within the DWBA the Lippmann-Schwinger equation is modified by the distorted wave basis as follows

$$\chi^{\pm} = \phi^{\pm} + G_0^{\pm} V_0 \ \chi^{\pm}, \tag{2.7}$$

where $\chi^{\pm}$ are now distorted incoming and outgoing waves, respectively. The potential V_0 describes the interaction between the incoming projectile and the nucleus. A local representation of the potential can be obtained by convolving it with the ground state density $\rho_0(\vec{r}_N)$ of the nucleus. The result is called the optical potential and is given by

$$U_0(\vec{r}) = \int \rho_0(\vec{r}_N) V_0(\vec{r} - \vec{r}_N) \mathrm{d}^3 r_N. \tag{2.8}$$

In first order Born approximation the transition matrix T can be expressed in the distorted wave basis via

$$T \simeq \langle \chi_f^- | V | \chi_i^+ \rangle \simeq \langle \chi_f^- | \sum_{n=1}^{A} v_n | \chi_i^+ \rangle \simeq \langle \chi_f^- | \sum_{n=1}^{A} t_n | \chi_i^+ \rangle, \tag{2.9}$$

where v_n are two-body interactions between the projectile and the n-th nucleon of the target nucleus and t_n is obtained from a kinematic transformation of the free-nucleon scattering transition matrix. Love and Franey [60] determined a phenomenological description of the free nucleon-nucleon t-matrix for projectile energies of $100 - 800$ MeV. The t-matrix is given in the nucleon-nucleon system by

$$t_{NN} = \int e^{-i\vec{k}_f \cdot \vec{r}} V[1 + (-1)^\lambda P] e^{i\vec{k}_i \cdot \vec{r}} \mathrm{d}^3 r, \tag{2.10}$$

where P is the parity operator and λ denotes the relative angular momentum in the nucleon-nucleon system. The local potential V has the following form

$$V = V^C(r) + V^{LS}(r) \vec{L} \cdot \vec{S} + V^T(r) S_{12}, \tag{2.11}$$

where $V^C(r)$ is the central term, $V^{LS}(r)$ the spin-orbit term and $V^T(r)$ the tensor term with the usual spin-orbit $\vec{L} \cdot \vec{S}$ and tensor S_{12} operators. The radial parts of the central, spin-orbit and tensor terms are taken to be a sum of Yukawa forms with an additional factor r^2 in the case of the tensor term

$$V^C(r) = \sum_{i=1}^{N_C} V_i^C \frac{\exp(-r/R_i)}{r/R_i}, \tag{2.12}$$

$$V^{LS}(r) = \sum_{i=1}^{N_{LS}} V_i^{LS} \frac{\exp(-r/R_i)}{r/R_i}, \tag{2.13}$$

$$V^T(r) = \sum_{i=1}^{N_T} V_i^T r^2 \frac{\exp(-r/R_i)}{r/R_i}. \tag{2.14}$$

The variables V_i are complex strengths and R_i the range parameters. For the central term these parameters are fixed to be that of the long-range part of the one-pion-exchange potential.

For small momentum transfer the central term is dominant. In Fig. 2.1 contributions of the nucleon-nucleon t-matrix are presented in the small momentum transfer limit. t_0^C indicates the isoscalar spin independent part, $t_{\sigma\tau}^C$ the isovector spin dependent part, t_τ^C the isovector spin independent part and t_σ^C the isoscalar spin dependent part. A minimum for the isoscalar spin independent part t_0^C is observed around 300 MeV, which provides good conditions for studies

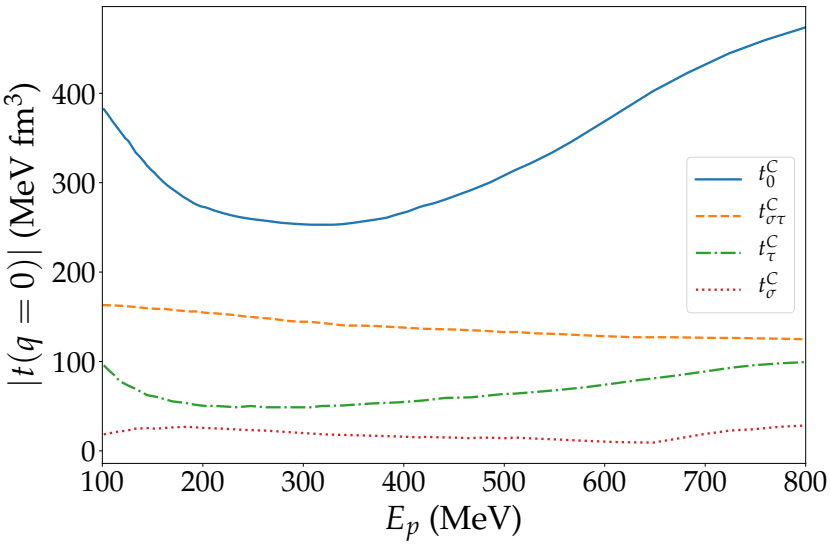

Figure 2.1: Energy dependence of the magnitude of the central parts of the nucleon-nucleon t-matrix in the small momentum transfer limit as determined by Love and Franey [60].

of isovector spin-flip transitions, because of the relatively strong $t_{\sigma\tau}^C$ part as compared to t_τ^C and t_σ^C parts.

2.1.2 Coulomb interaction

Due to the charged projectile and target nucleus, Coulomb interaction plays an important role in inelastic proton scattering. It is dominant if the impact parameter is larger than the sum of the projectile and target nucleus radii. This is the case for small scattering angles, where in the classical picture the point-like projectile is moving along a hyperbolic trajectory in the electric field of the target nucleus. The differential cross section for elastic scattering is the well known Rutherford formula [61]

$$\left(\frac{\mathrm{d}\sigma}{\mathrm{d}\Omega}\right)_{Ruth} = \left(\frac{Z_1 Z_2 e^2}{4E}\right)^2 \frac{1}{\sin^4\left(\frac{\theta}{2}\right)}, \tag{2.15}$$

where Z_1 and Z_2 are the charges of the projectile and the target nucleus, respectively, E the projectile energy and θ the scattering angle. In the case of inelastic scattering, both the projectile as well as the target nucleus can be excited in principle. However, the first excited state of the proton is the delta resonance around 300 MeV. So that in the experiments discussed in this work only the target nucleus is excited. The differential cross section for exciting a final state $|f\rangle$ from an initial state $|i\rangle$ is given by

$$\left(\frac{\mathrm{d}\sigma}{\mathrm{d}\Omega}\right) = \left(\frac{\mathrm{d}\sigma}{\mathrm{d}\Omega}\right)_{Ruth} P_{i\to f}. \tag{2.16}$$

The transition probability $P_{i\to f} = |a_{i\to f}|^2$ can be evaluated in perturbation theory assuming the time-dependent electromagnetic field $V(\vec{r}(t))$ generated by the projectile excites the target nucleus only weakly

$$a_{i\to f} = \frac{1}{i\hbar}\int_{-\infty}^{\infty} e^{i\omega t}\langle f|V(\vec{r}(t))|i\rangle \,\mathrm{d}t. \tag{2.17}$$

Here, ω is the transition frequency. The multipole expansion of $V(\vec{r}(t))$ yields for the excitation amplitude

$$a_{i\to f} = i\sum_{\lambda}\chi^{\pi\lambda}_{i\to f} f_\lambda(\xi). \tag{2.18}$$

The function $f_\lambda(\xi)$ describes the dependence of the cross section on the adiabaticity parameter $\xi = \omega b/\gamma v$, where b is the impact parameter and v is the velocity of the projectile. One finds $f_\lambda(\xi) = 1$ for $\xi = 0$ and $f_\lambda(\xi) \sim \exp(-\pi\xi)$ for $\xi \gg 1$. The parameter $\chi^{\pi\lambda}_{i\to f}$ is a measure for the interaction strength and is given by

$$\chi^{\pi\lambda}_{i\to f} = \frac{Z_1 e\langle f|\mathcal{M}(\pi\lambda\mu)|i\rangle}{\hbar c b^\lambda}, \tag{2.19}$$

where $\mathcal{M}(\pi\lambda\mu)$ is the multipole moment for the electric or magnetic transition $\pi \in \{E, M\}$ with the multipolarity λ and the magnetic quantum number μ. The total cross section for exciting a state $|f\rangle$ can then be calculated as

$$\sigma = 2\pi\int_R^{b_a} |\chi^{\pi\lambda}_{i\to f}(b)|^2 b \,\mathrm{d}b. \tag{2.20}$$

The lower limit R of the integral is the sum of the projectile and target nucleus radii. This ensures that only pure Coulomb excitations are considered. The upper limit b_a is the impact parameter corresponding to the adiabaticity parameter $\xi = 1$. Inserting Eqn. (2.19) in Eqn. (2.20) yields an expression for the total cross section for the excitation of a state $|f\rangle$ from the ground state of an even-even nucleus

$$\sigma_{\pi\lambda} \approx \left(\frac{Z_1 e^2}{\hbar c}\right)^2 \frac{B(\pi\lambda, 0\to\lambda)}{e^2 R^{2\lambda}}\pi R^2 \begin{cases} (\lambda-1)^{-1} & \text{for } \lambda \geq 2, \\ 2\ln(b_a/R) & \text{for } \lambda = 1. \end{cases} \tag{2.21}$$

The last equation entails that by measuring the total cross section the reduced transition probability $B(\pi\lambda)$ can be extracted from experiments. On the other hand reduced transition probabilities from model calculations can be used to estimate the total cross section for a given transition.

2.2 Equivalent photon method

From the quantum electrodynamical point of view Coulomb excitation can be described as an absorption of virtual photons by the target nucleus. The number of virtual photons absorbed by the nucleus corresponds then to the number of real photons which would have the same effect on the nucleus. The theory behind this picture is the so-called equivalent photon method, which goes back to Fermi's ideas [62] and was later on developed by Weizsäcker [63] and Williams [64,65]. Extensive reviews of the method can be found in Refs. [66,67].

Within the equivalent photon method the cross section for Coulomb excitation can be written as

$$\sigma_{i\to f} = \sum_{\pi\lambda} \int N_{\pi\lambda}(\omega)\sigma_{abs}^{\pi\lambda}(\omega)\frac{1}{\omega}\mathrm{d}\omega, \tag{2.22}$$

where $\sigma_{abs}^{\pi\lambda}(\omega)$ is the photoabsorption cross section and $N_{\pi\lambda}(\omega)$ the virtual photon number given by

$$N_{\pi\lambda}(\omega) = Z_1^2\alpha\frac{\lambda[(2\lambda+1)!!]^2}{(2\pi)^3(\lambda+1)}\sum_{\mu}\left|G_{\pi\lambda\mu}\left(\frac{c}{v}\right)\right|^2 g_\mu(\omega). \tag{2.23}$$

This equation can be evaluated using the functions $G_{\pi\lambda\mu}$ and g_μ tabulated in Ref. [59]. The differential virtual photon numbers for E1, M1 and E2 transitions (other multipolarities can be neglected) are then given by the following expressions

$$\frac{\mathrm{d}N_{E1}}{\mathrm{d}\Omega} = \frac{Z_1^2\alpha\varepsilon^4}{4\pi^2}\left(\frac{\zeta}{\gamma\beta}\right)^2\left(K_1^2+\frac{1}{\gamma^2}K_0^2\right), \tag{2.24}$$

$$\frac{\mathrm{d}N_{M1}}{\mathrm{d}\Omega} = \frac{Z_1^2\alpha\varepsilon^4}{4\pi^2}\left(\frac{\zeta}{\gamma}\right)^2\exp\left(-\frac{\pi\zeta}{\gamma}\right)K_1^2, \tag{2.25}$$

$$\frac{\mathrm{d}N_{E2}}{\mathrm{d}\Omega} = \frac{Z_1^2\alpha\varepsilon^2}{4\pi^2}\left(\frac{1}{\beta}\right)^4\exp\left(-\frac{\pi\zeta}{\gamma}\right)\left(\frac{4}{\gamma^2}(K_1^2+xK_0K_1+x^2K_0^2)+x^2\left(2-\beta^2\right)^2K_1^2\right). \tag{2.26}$$

Here, $\varepsilon = 1/\sin(\theta/2)$ with the scattering angle θ and $\zeta = \omega a/v$ with $a = Z_1Z_2e^2/\mu v^2$. K_n are modified Bessel functions of n-th order with the argument $x = \varepsilon\zeta\gamma^{-1}\cos(\theta/2)$.

In Fig. 2.2 differential virtual photon numbers are shown for E1, M1 and E2 transitions induced by a 295 MeV proton incident on a ^{120}Sn target as a function of the scattering angle θ, exemplary for two different virtual photon energies E_γ. It can be seen that the differential virtual photon number decreases for E1 and M1 transitions with increasing scattering angle while it is rather constant for E2 transitions. The maximum of the differential virtual photon number

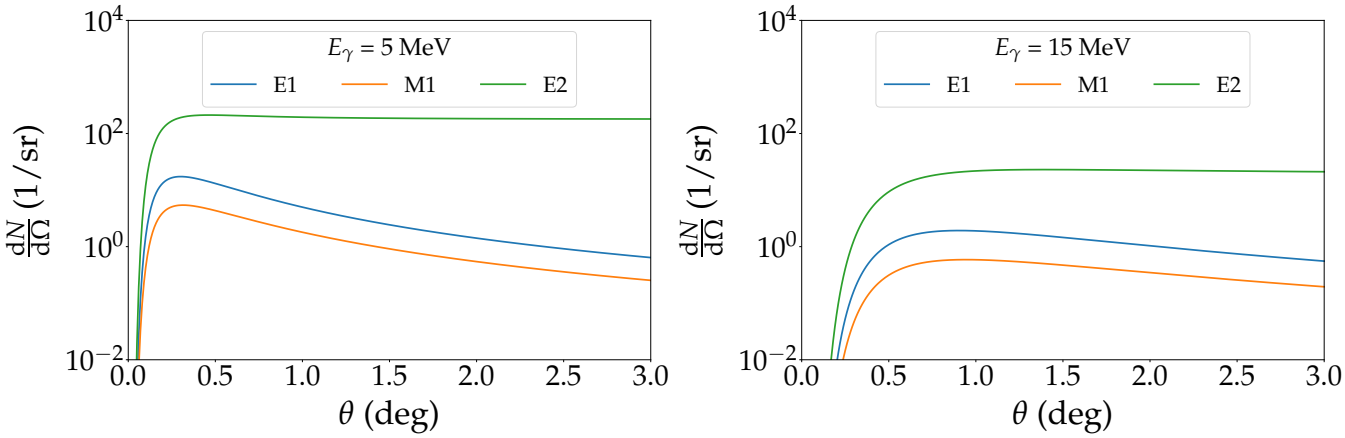

Figure 2.2: Semi-classical calculation of differential virtual photon numbers for E1, M1 and E2 transitions induced by a 295 MeV proton incident on a ^{120}Sn target for virtual photon energies of 5 MeV and 15 MeV, respectively.

is energy dependent for dipole transitions shifting from 0.3° to 0.5° in the examples shown. The semi-classical calculations with a sharp lower impact parameter show a significant decrease in the differential virtual photon number for small angles eventually leading to a singularity at 0°. Although this problem can be circumvented to some extent by convolving the differential virtual photon numbers with the experimental scattering angle resolution, it still poses a serious problem for the analysis of inelastic proton scattering data, since these data are measured at scattering angles close to 0°. In fact it was shown in Ref. [68] that these semi-classical calculations are only valid for the heaviest nuclei such as ^{208}Pb and for rather low virtual photon energies due to the shift of the maximum of the differential virtual photon number towards smaller scattering angles with decreasing energy.

Bertulani and Nathan [69] tackled this problem by developing a closed-form theory of Coulomb excitation based on the eikonal approximation, where effects of strong absorption, relativity and retardation are included from the outset. Equation (2.23) can be rewritten in differential form as

$$\frac{dN_{\pi\lambda}}{d\Omega} = Z_1^2\alpha\left(\frac{\omega k}{\gamma v}\right)^2 \frac{\lambda[(2\lambda+1)!!]^2}{(2\pi)^3(\lambda+1)} \sum_\mu \left|G_{\pi\lambda\mu}\left(\frac{c}{v}\right)\right|^2 \left|\Omega_\mu(q)\right|^2, \tag{2.27}$$

where $q = 2k\sin(\theta/2)$ is the momentum transfer. The function $\Omega_\mu(q)$ is given by

$$\Omega_\mu(q) = \int_0^\infty J_\mu(qb) K_\mu\left(\frac{\omega b}{\gamma v}\right) \exp(i\chi(b)) b db, \tag{2.28}$$

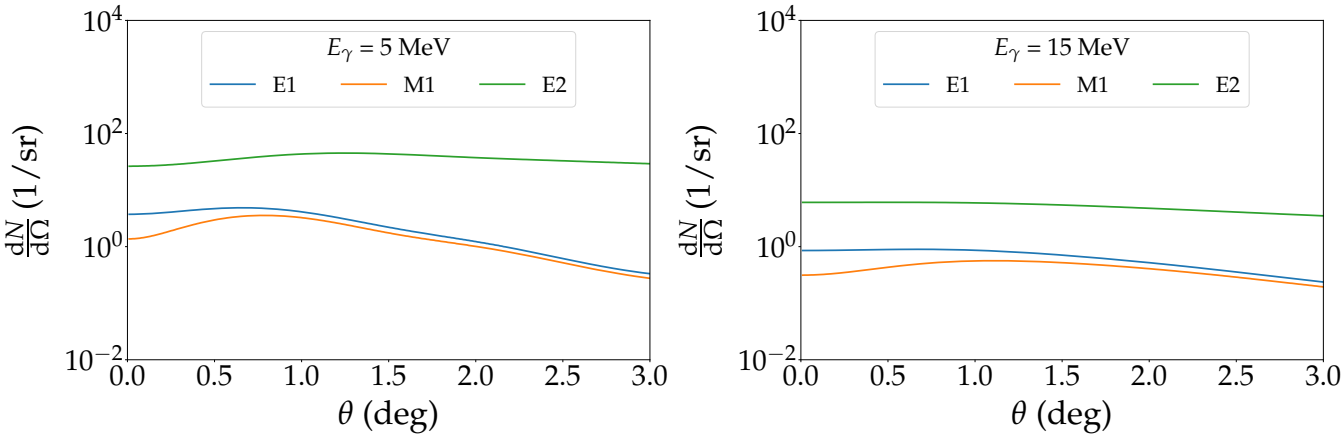

Figure 2.3: Eikonal approximation calculation of differential virtual photon numbers for E1, M1 and E2 transitions for the same kinematics as in Fig. 2.2.

where J_μ are Bessel functions and K_μ modified Bessel functions of μ-th order. The eikonal phase $\chi(b)$ is expressed as

$$\chi(b) = -\frac{1}{\hbar v}\int_0^\infty U_N^{opt}(z', b)\mathrm{d}z' + \psi_C(b), \tag{2.29}$$

where U_N^{opt} is the nuclear optical potential and ψ_C is the Coulomb phase. The nuclear optical potential can either be obtained from fits to available elastic scattering data or constructed in terms of the nucleon-nucleon t-matrix discussed in Section 2.1.1.

Calculations of differential virtual photon numbers using the eikonal approximation are shown in Fig. 2.3. It is apparent that the singularity around 0° has disappeared, so that this calculations provide an improved description of the Coulomb excitation process within the equivalent photon method. An absolute comparison between the semi-classical and the eikonal approximation calculation of the differential virtual photon number for E1 transitions is shown in Fig. 2.4. Both calculations agree reasonably well besides the obvious deviation at 0°, although at higher virtual photon energies the semi-classical calculation yields a slightly larger differential photon number even for larger scattering angles.

The double differential cross section can be expressed as a function of the differential virtual photon number and the photoabsorption cross section

$$\frac{\mathrm{d}^2\sigma}{\mathrm{d}\Omega\mathrm{d}E} = \frac{1}{E}\sum_{\pi\lambda}\frac{\mathrm{d}N_{\pi\lambda}}{\mathrm{d}\Omega}\sigma_{abs}^{\pi\lambda}. \tag{2.30}$$

This equation provides a relatively simple way to convert inelastic proton scattering cross sections (or any other cross sections involving Coulomb excitation) into photoabsorption cross

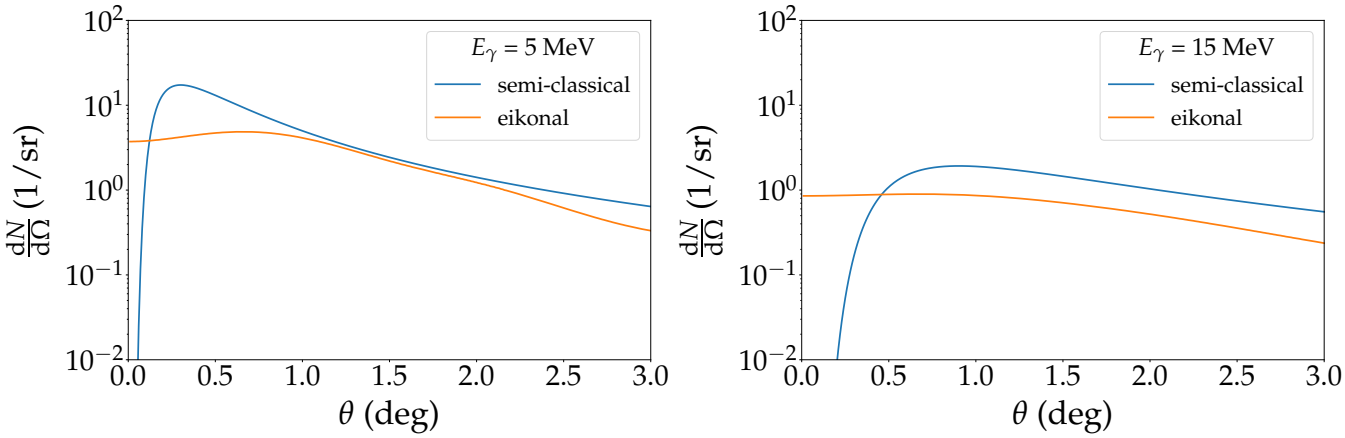

Figure 2.4: Comparison between the semi-classical and the eikonal approximation calculation of the differential virtual photon number for E1 transitions for the same kinematics as in Figs. 2.2 and 2.3.

sections and vice versa. By this means experiments with real photons can be directly compared to Coulomb excitation experiments.

2.3 Quasiparticle phonon model

In the framework of this thesis, DWBA calculations were performed using transition amplitudes and single particle wave functions, which were obtained from the quasiparticle phonon model (QPM). The QPM is a phenomenological microscopic model proven to be very successful in the past to describe collective excitations in medium and heavy mass nuclei [70–73]. Within this model excitations of nuclei are described via creation and annihilation of particle-hole pairs. Particle-hole transitions entail always an integer change of quantum numbers, so that such transitions can be described by creation and annihilation of phonons which follow Bose-Einstein statistics. One-phonon excitations are the most simple ones within this model. Although multi-phonon excitations are possible in principle, calculations involving more than three phonons are not feasible in terms of diagonalising the corresponding model spaces.

The QPM calculation can be divided in four steps. In the first step, single-particle energies and wave functions using a Wood-Saxon potential are calculated. Thereafter, the canonical Bogoliubov transformations are carried out to convert particle operators into quasiparticle operators. In the third step the phonon basis is constructed using quasiparticle random phase approximation (QRPA) calculations. Finally, in the last step the quasiparticle phonon interaction is included. In the following each of these steps will be covered briefly. The formalism presented here follows closely the representation of Bertulani and Ponomarev [74]. An in-depth description can be found in Ref. [75].

The Hamiltonian for even-even nuclei with nucleons moving in a mean field and interacting with each other by means of a residual interaction is given as

$$H = H_{s.p.} + H_{pair} + H_{r.i.}. \tag{2.31}$$

The first term $H_{s.p.}$ describes the mean field which protons and neutrons are exposed to. By means of the second quantisation this term can be expressed via creation $a^{+}_{jm\tau}$ and annihilation $a_{jm\tau}$ operators in the following form

$$H_{s.p.} = \sum_{\tau}^{n,p} \sum_{j,m} E_{j\tau} a^{\dagger}_{jm\tau} a_{jm\tau}, \tag{2.32}$$

where $j \equiv [n, l, j]$ and m are quantum numbers of the single-particle basis and $E_{j\tau}$ is the energy of the single-particle state. The index τ distinguishes between protons p and neutrons n. The second term H_{pair} in Eqn. (2.31) accounts for the pairing energy in non-magic nuclei. It is represented by

$$H_{pair} = \sum_{\tau}^{n,p} \sum_{j,j'} G^{(0)}_{\tau} \sqrt{(2j+1)(2j'+1)} [a^{\dagger}_{jm\tau} a^{\dagger}_{j-m\tau}]_{00} [a_{j'-m'\tau} a_{j'm'\tau}]_{00}, \tag{2.33}$$

with

$$[a^{\dagger}_{j} a^{\dagger}_{j'}]_{\lambda\mu} = \sum_{m,m'} C^{\lambda\mu}_{jmj'm'} a^{\dagger}_{jm}\, a^{\dagger}_{j'm'}, \tag{2.34}$$

where $C^{\lambda\mu}_{jmj'm'}$ is the Clebsch-Gordan coefficient and $G^{(0)}_{\tau}$ is a constant matrix element describing the monopole field of the pairing force. $G^{(0)}_{\tau}$ is chosen in such a way that the experimental pairing energy is reproduced properly.

The residual interaction $H_{r.i.}$ in Eqn. (2.31) is taken in form of a multipole decomposition and expressed in a separable form

$$H^{(p-h)}_{r.i.} = \sum_{\lambda\mu} \sum_{\tau\rho}^{\pm 1} (\kappa^{(\lambda)}_{0} + \rho\kappa^{(\lambda)}_{1}) M^{\dagger}_{\lambda\mu}(\tau) M_{\lambda\mu}(\tau\rho). \tag{2.35}$$

The model parameters $\kappa_i^{(\lambda)}$ determine the strength of the isoscalar and isovector residual interaction and $\rho = \pm 1$ distinguishes between isoscalar and isovector transitions, respectively. For states with natural parity the multipole operator $M^\dagger_{\lambda\mu}(\tau)$ has the form

$$M^\dagger_{\lambda\mu}(\tau) = \sum_{j,m,j',m'} \langle jm\tau | i^\lambda f^\tau_\lambda(r) Y_{\lambda\mu}(\Omega) | j'm'\tau \rangle a^\dagger_{jm\tau} a_{j'm'\tau} \tag{2.36}$$

and for states with unnatural parity

$$M^\dagger_{\lambda\mu}(\tau) = \sum_{j,m,j',m',lm_1} \langle jm\tau | i^l f^\tau_l(r) [\vec{\sigma} \cdot \vec{Y}_{lm_1}(\Omega)]_{\lambda\mu} | j'm'\tau \rangle a^\dagger_{jm\tau} a_{j'm'\tau}. \tag{2.37}$$

The function $f^\tau_\lambda(r)$ is the radial form factor which is usually taken as r^λ or as the derivative of the central potential of the mean field $f^\tau_\lambda(r) = \mathrm{d}U^\tau(r)/\mathrm{d}r$. To obtain the basic QPM calculations, the Hamiltonian from Eqn. (2.31) needs to be diagonalised. The single-particle and the pairing Hamiltonians will be diagonalised first. For this purpose the particle operators are transformed into quasiparticle operators by means of the canonical Bogoliubov transformation

$$a^\dagger_{jm\tau} = u_j \, \alpha^\dagger_{jm\tau} + (-1)^{j-m} v_j \, \alpha_{j-m\tau}, \tag{2.38}$$

where the quantities u_j^2 and v_j^2 correspond to occupation probabilities in the state j for particles and holes, respectively. The ground state of the nucleus is assumed to be a quasiparticle vacuum with $\alpha_{jm\tau}|\rangle_q \equiv 0$, so that the minimisation of the ground state energy

$$\delta \left\{ {}_q\langle | H_{s.p.} + H_{pair} | \rangle_q + \sum_j \mu_j (u_j^2 + v_j^2 - 1) \right\} = 0, \tag{2.39}$$

using the Lagrange multipliers μ_j yields the BCS equations [76] known from the theory of superconductivity, which in turn lead to correlation functions $C_\tau = G^{(0)}_\tau \sum_j u_j v_j$ and chemical potentials λ_τ for proton and neutron systems. The coefficients of the Bogoliubov transformation can then be determined in the following way

$$v_j^2 = \frac{1}{2} \left(1 - \frac{E_{j\tau} - \lambda_\tau}{\epsilon_{j\tau}} \right), \tag{2.40}$$

$$u_j^2 = 1 - v_j^2, \tag{2.41}$$

with the quasiparticle energy $\epsilon_{j\tau} = \sqrt{C_\tau^2 + (E_{j\tau} - \lambda_\tau)^2}$. The first two terms of Eqn. (2.31) can now be written in the following form

$$H_{s.p.} + H_{pair} = \sum_{\tau}^{n,p} \sum_{j,m} \epsilon_{j\tau} \alpha^\dagger_{jm\tau} \alpha_{jm\tau}. \tag{2.42}$$

Since the ground state was determined as the quasiparticle vacuum, the simplest excited states of a nucleus are two-quasiparticle states $\alpha^\dagger_{jm\tau}\alpha^\dagger_{j'm'\tau}|\rangle_q$ corresponding to particle-hole transitions for vanishing monopole pairing. Both quasiparticles are fermions, but couple to an integer total angular momentum and hence follow Bose-Einstein statistics. This allows for an introduction of a more convenient phonon operator with multipolarity λ and projection μ

$$Q^\dagger_{\lambda\mu i} = \frac{1}{2} \sum_{\tau}^{n,p} \sum_{j,j'} \left\{ \psi^{\lambda i}_{jj'\tau} [\alpha^\dagger_{j\tau} \alpha^\dagger_{j'\tau}]_{\lambda\mu} - (-1)^{\lambda-\mu} \phi^{\lambda i}_{jj'\tau} [\alpha_{j'\tau} \alpha_{j\tau}]_{\lambda-\mu} \right\}, \tag{2.43}$$

where the index i counts the phonons which couple to the same multipolarity. The coefficients $\psi^{\lambda i}_{jj'\tau}$ and $\phi^{\lambda i}_{jj'\tau}$ are obtained by diagonalising the Hamiltonian in the space of one-phonon states $Q^\dagger_{\lambda\mu i}|\rangle_{ph}$ by means of a variation procedure

$$\delta \left\{ {}_{ph}\langle | Q_{\lambda\mu i} H Q^\dagger_{\lambda\mu i} | \rangle_{ph} - \frac{\omega_{\lambda i}}{2} \left[\sum_{jj'} \{ (\psi^{\lambda i}_{jj'\tau})^2 - (\phi^{\lambda i}_{jj'\tau})^2 \} - 2 \right] \right\} = 0, \tag{2.44}$$

where $\omega_{\lambda i}$ is the energy of i-th phonon. The procedure yields the RPA equations whose solutions for every multipolarity λ^π lead to a one-phonon spectrum.

Calculations at this level already provide good results for the description of global properties of giant resonances. The energy weighted sum rule (EWSR) and the centroid energy are reproduced rather well. Adding multi-phonon configurations barely influence these global properties. Multi-phonon configurations are however extremely important for the description of the well-known 1^-_1 state, which has a dominant two-phonon component $[2^+_1 \times 3^-_1]_{1^-}$ [1]. The experimentally observed strength fragmentation is another feature which can only be explained by inclusion of multi-phonon configurations.

To include the mixing between simple and complex configurations, the model Hamiltonian is rewritten in the space of one-phonon states

$$H = \sum_{\lambda\mu i} \omega_{\lambda i} Q^\dagger_{\lambda\mu i} Q_{\lambda\mu i} + H_{int}, \tag{2.45}$$

with H_{int} expressed in the space of phonon operators as

$$H_{int} = \sum_{\lambda\mu i} \sum_{\lambda_1\mu_1 i_1} \sum_{\lambda_2\mu_2 i_2} U^{\lambda_1 i_1}_{\lambda_2 i_2}(\lambda i) Q^{\dagger}_{\lambda\mu i} \left[Q_{\lambda_1\mu_1 i_1} Q_{\lambda_2\mu_2 i_2} \right]_{\lambda\mu} + \text{h.c.}, \tag{2.46}$$

where $U^{\lambda_1 i_1}_{\lambda_2 i_2}$ is the matrix element of the interaction between one- and two-phonon configurations, which can be calculated using the coefficients $\psi^{\lambda i}_{jj'\tau}$ and $\phi^{\lambda i}_{jj'\tau}$. Finally, the wave function of excited states in the most general form as a mixture of one-phonon, two-phonon, etc. configurations is given by the following equation

$$\begin{aligned} \Psi^{\nu}(JM) &= \left\{ \sum_{\alpha_1} S^{\nu}_{\alpha_1}(J) Q^{\dagger}_{\alpha_1} + \sum_{\alpha_2\beta_2} \frac{D^{\nu}_{\alpha_2\beta_2}(J)}{\sqrt{1+\delta_{\alpha_2\beta_2}}} \left[Q^{\dagger}_{\alpha_2} Q^{\dagger}_{\beta_2} \right]_{JM} \right. \\ &+ \left. \sum_{\alpha_3\beta_3\gamma_3} \frac{T^{\nu}_{\alpha_3\beta_3\gamma_3}(J)}{\sqrt{1+\delta_{\alpha_3\beta_3\gamma_3}}} \left[Q^{\dagger}_{\alpha_3} Q^{\dagger}_{\beta_3} Q^{\dagger}_{\gamma_3} \right]_{JM} + \cdots \right\} \Big| \Big\rangle_{ph}, \end{aligned} \tag{2.47}$$

$$\delta_{\alpha_3\beta_3\gamma_3} = \delta_{\alpha_3\beta_3} + \delta_{\alpha_3\gamma_3} + \delta_{\beta_3\gamma_3} + 2\delta_{\alpha_3\beta_3}\delta_{\alpha_3\gamma_3}, \tag{2.48}$$

where α, β and γ indicate the phonon multipolarities and order number λi. The index ν labels whether the state J is the first, second, etc. state in the total energy spectrum of the system. The wave function coefficients $S^{\nu}_{\alpha_1}$, $D^{\nu}_{\alpha_2\beta_2}$ and $T^{\nu}_{\alpha_3\beta_3\gamma_3}$ can be obtained from a diagonalisation of the Hamiltonian (2.45).

3 Experiment

The experiments presented in this work were performed at the Research Center for Nuclear Physics (RCNP) in Osaka, Japan. A layout of the facility is shown in Fig. 3.1. In the various experimental halls (ES, EN, N0, WS) different experiments can be carried out. In the east south (ES) hall experiments with ultra cold neutrons can be performed [78]. Experiments with unstable nuclei can be conducted in the east north (EN) hall [79]. In the north (N0) section spin-isospin excitations can be investigated using a time of flight (ToF) set-up [80]. Finally, the inelastic proton scattering experiments discussed in this work are performed in the west south (WS) hall.

This facility allows to perform experiments with polarised and unpolarised protons and heavier particles. For polarised proton scattering experiments the HIPIS (High Intensity Polarised Ion Source) can be used [81], while the NéoMAFIOS (Machine Fabriquant Ions Strippé) ion source provides unpolarised protons [82, 83]. The protons are accelerated by the azimuthally varying field (AVF) cyclotron to an energy of 54 MeV. The ring cyclotron is then used to accelerate the proton beam further to the final energy of 295 MeV. Finally, the beam is guided to the west south (WS) experimental hall where it can be used to perform inelastic proton scattering experiments.

3.1 Spectrometers

The proton scattering experiments were performed using the Grand Raiden (GR) Spectrometer [84] and the Large Acceptance Spectrometer (LAS) [85]. The latter was used in this experiment to monitor the vertical beam position, which is important for a precise calibration of the scattering angle as discussed in Section 4.3. Both spectrometers are shown in Fig. 3.2.

The Grand Raiden Spectrometer has a Q-S-Q-D-M-D-DSR magnet configuration, where D denotes dipole magnets, Q quadrupole magnets, S sextupole magnets and M stands for a multipole magnet. The DSR (dipole magnet for spin rotation) is a special magnet which is usually used for polarised proton scattering experiments. The spectrometer has a high momentum resolution achieved by applying complete dispersion matching including lateral and angular dispersion as well as focus matching [86]. The detector system consists of two vertical drift chambers (VDC) [87] with two wire planes each and two plastic scintillators used as trigger detectors. For polarised proton scattering experiments a focal plane polarimeter (FPP) [88] is used in addition consisting of a thick carbon analyser target, four multi-wire proportional chambers (MWPC) and two plastic scintillator hodoscopes.

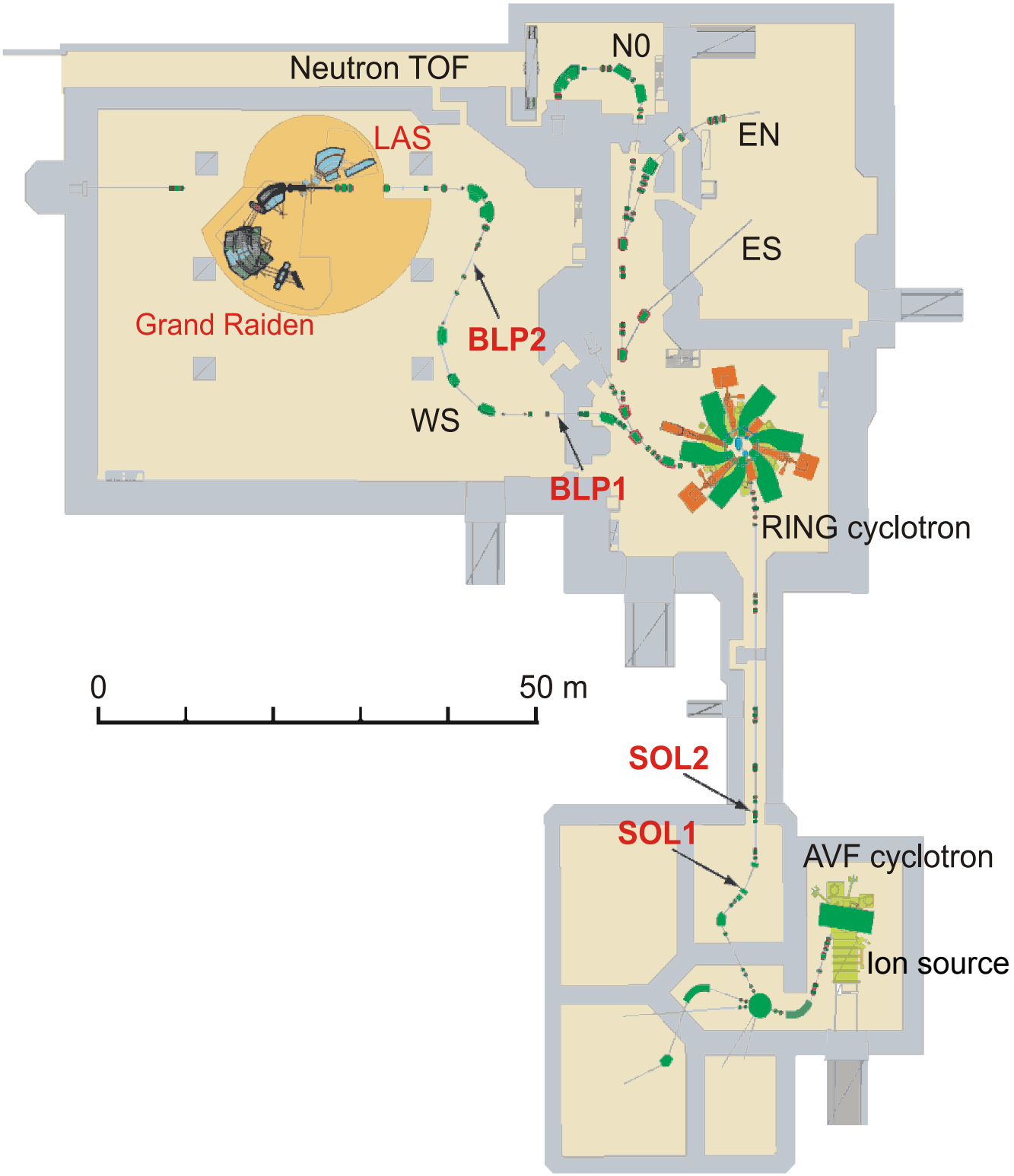

Figure 3.1: Schematic overview of the RCNP facility [77].

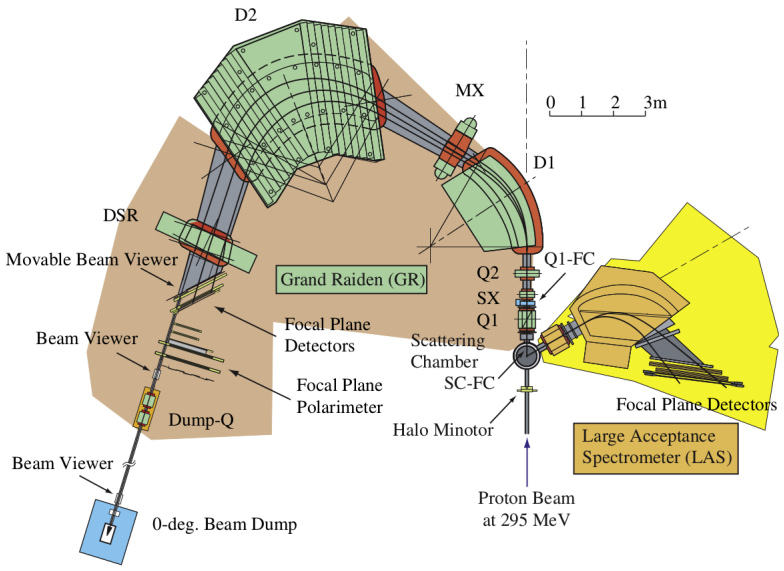

Figure 3.2: The Grand Raiden and Large Acceptance spectrometers in the 0° set-up [6].

The Large Acceptance Spectrometer consists of a quadrupole and a dipole magnet. It provides a high momentum and solid angle acceptance. Similar to the GR spectrometer the detector system of LAS is composed of three vertical drift chambers and two plastic scintillators. The spectrometer is very sensitive to the vertical beam position due to its large vertical magnification. Beam shifts of ± 0.01 mm can be detected. Detailed specifications for both spectrometers are given in Tab. 3.1.

Table 3.1: Specification of the Grand Raiden and Large Acceptance spectrometers [84, 85].

	GR	LAS
Magnet configuration	Q-S-Q-D-M-D-DSR	Q-D
Mean orbit radius	3 m	1.75 m
Total deflection angle	162°	70°
Focal plane inclination	45°	57°
Magnetic rigidity	5.4 Tm	3.2 Tm
Vertical magnification	5.98	-7.3
Horizontal magnification	-0.417	-0.4
Momentum acceptance	±2.5 %	±15 %
Momentum resolution	37076	4980
Horizontal angle acceptance	±20 mr	±60 mr
Vertical angle acceptance	±70 mr	±100 mr

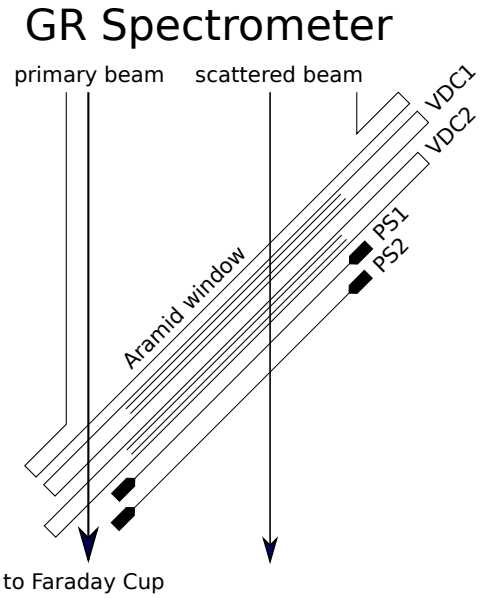

Figure 3.3: The focal plane detector system of the Grand Raiden Spectrometer.

3.2 Focal plane detectors

The focal plane detector system of the Grand Raiden and the Large Acceptance spectrometers consists of vertical drift chambers and plastic scintillators. Each VDC consists of two, or in the case of the LAS detector system, three anode wire planes sandwiched between cathode planes. To increase the uniformity of the electric field produced between the anode wires and the cathode plane, additional field wires are embedded. The applied voltage is typically around -5.7 kV at the cathode plane and -0.3 kV at the field wires respectively, while the sense wires remain at ground level. Each plastic scintillator has two photomultiplier tubes (PMT) attached to both sides. A mean timer generates a signal, if a particle passes through a scintillator. A coincident signal between the two scintillators provides a trigger signal which starts the whole data acquisition system. In Fig. 3.3 the focal plane detector system of the Grand Raiden Spectrometer is shown. Details concerning the drift chambers can be found in Tab. 3.2.

Inelastically scattered protons are deflected stronger by the dipoles of the Grand Raiden Spectrometer compared to the primary beam. Entering the drift chambers these protons ionise along their ways the argon-isobutane-isopropyl-alcohol gas mixture and produce free electron-ion pairs. In the electric field inside of the VDC the produced electrons drift then with a constant velocity to the nearest sense wires. Combining the four wire planes (X1, X2, U1, U2) and the two plastic scintillators, the trajectory of the incident scattered protons can be reconstructed. The first VDC contains two wire planes X1 and X2 oriented perpendicular to the beam direction and the dispersive direction of the spectrometer, respectively. It provides information on the horizontal position x_{fp} and the horizontal scattering angle θ_{fp} of the incident protons.

Table 3.2: Vertical drift chamber properties of the Grand Raiden and Large Acceptance spectrometers.

	Grand Raiden Spectrometer	Large Acceptance Spectrometer
Wire configuration	X (0°), U (-48.19°)	X (0°), U (-31°), V (31°)
Active area	1150 mm × 120 mm	1700 mm × 350 mm
Number of sense wires	192 (X), 208 (U)	272 (X), 256 (U, V)
Anode-cathode gap	10 mm	10 mm
Anode wire spacing	2 mm	2 mm (X), 2.33 mm (U, V)
Sense wire spacing	6 mm (X), 4 mm (U)	6 mm (X), 7 mm (U, V)
Applied voltage	-5.7 kV (cath.), -0.35 kV (pot.)	-4.3 kV (cath.), -0.3 kV (pot.)
Entrance and exit windows	12.5 µm carbon aramid film	25 µm carbon aramid film
Sense wires	20 µm gold-plated tungsten wire	
Potential wires	50 µm gold-plated beryllium copper wire	
Cathode	10 µm carbon aramid film	
Gas mixture	argon (70 %) + isobutane (30 %) + isopropyl alcohol	

The second VDC contains the U1 and U2 planes oriented again perpendicular to the beam direction but tilted to an angle of 48.19° relative to the X planes. This configuration provides information on the vertical position y_{fp} and on the vertical angle ϕ_{fp}, respectively.

3.3 Details of the experiment

The inelastic proton scattering experiments were performed in June 2015 and in December 2017. In 2015, data on ^{112,116,124}Sn and with less statistics on ^{118,120}Sn were taken. In the second experiment, in 2017, ^{112,116,124}Sn were measured again to improve statistics. Additionally ^{114,118,120,122}Sn with less statistics were measured. In both experiments data were taken at spectrometer angles of 0°, 2.5° and 4.5°. Typical beam intensity was $2 - 20$ nA, depending on the angle of the spectrometer. The incident proton beam was unpolarised and had an energy of 295 MeV. The energy resolution was $30 - 40$ keV full width at half maximum (FWHM).

3.3.1 Targets

A summary of the used targets is given in Tab. 3.3. All tin targets were self-supporting metallic foils. Most of the targets were highly enriched ($\geq$95 %) and had a thickness between 3.4 mg/cm^2 and 10.3 mg/cm^2. However, in some cases the enrichment was unknown. In the case of ^{112}Sn, a second target with a known enrichment was used therefore, but could only be measured in achromatic mode with corresponding worse resolution due to its shape and target thickness. Details on the determination of the enrichment of the ^{112,118,122}Sn targets will be described in Section 4.8. ^{120}Sn was measured to check the consistency with a previous experiment [73, 89]. Before and after each measurement of a main target for one hour, a short

Table 3.3: Targets used during the experiments.

Target	Thickness (mg/cm^2)	Enrichment (%)	Purpose
^{112}Sn	3.38	unknown	main target
^{112}Sn	10.3	95.1	calibration
^{114}Sn	7.51	87.1	main target
^{116}Sn	4.98	95.5	main target
^{116}Sn	4.65	97.8	main target
^{118}Sn	4.50	unknown	main target
^{120}Sn	6.50	98.4	consistency check
^{122}Sn	5.20	unknown	main target
^{124}Sn	5.00	97.0	main target
^{124}Sn	4.67	97.4	main target
^{197}Au	1.68	unknown	beam tuning
^{26}Mg	1.16	unknown	energy calibration
^{58}Ni	100.1	unknown	sieve slit measurement
^{12}C	1.01	98.9	energy calibration
C_2H_4	2.30	–	energy calibration and beam tuning

measurement of ^{12}C was performed for energy calibration purposes and to account for possible energy shifts. To improve the energy calibration even further, ^{26}Mg and C_2H_4 (polyethylene) were measured occasionally. Sieve slit measurements, which are required for a precise angle calibration, were performed using a thick ^{58}Ni target. ^{197}Au was used for beam tuning. The target thickness was remeasured for all tin targets. The uncertainty of the target thickness was determined to be around 5 %. The uncertainty of the target enrichment is typically less than 1 %.

4 Data analysis

To process the raw data of the GR and LAS spectrometers, the *ANALYZER* [90] computer program was used. This program produces an *HBOOK* file containing histograms of the analysed data. The *HBOOK* file can then be read by the program *PAW* [91] developed at CERN to visualise the data. *PAW* provides a good starting point for basic analysis of the data. More complex analysis was performed using the open-source package manager *Anaconda* [92] which provides over 1500 open-source *Python/R* packages. The data analysis consists of several steps, described in the following sections.

- Particle identification
- Track reconstruction
- Scattering angle calibration
- Kinematical correction
- Energy calibration
- Background subtraction
- Determination of the double differential cross sections

4.1 Particle identification

The desired reaction for the experiments discussed in this work is inelastic proton scattering (p,p'). However, transfer reactions such as (p,d) or (p,t) are in principle possible albeit presumably small. To exclude such reactions a particle identification analysis was employed.

According to the Bethe-Bloch formula [93] the energy loss of a charged particle is mainly dependent on its velocity and charge. Hence, protons, deuterons and tritons can be discriminated by investigating the deposited energy of aforementioned particles in one of the plastic scintillators. On the other hand, these particles can also be discriminated by their time of flight (ToF). The ToF information can be obtained from the trigger signal generated by one of the scintillators and from the knowledge of the radio frequency (RF) of the AVF cyclotron. To improve the particle identification, the ToF information was corrected in such a way that it is independent of the horizontal position x_{fp} and of the horizontal scattering angle θ_{fp}. The corrected ToF is then given by the equation

$$\mathrm{ToF_c} = \mathrm{ToF} - 0.114(1)x_{fp} + 9.9(3)\theta_{fp}. \tag{4.1}$$

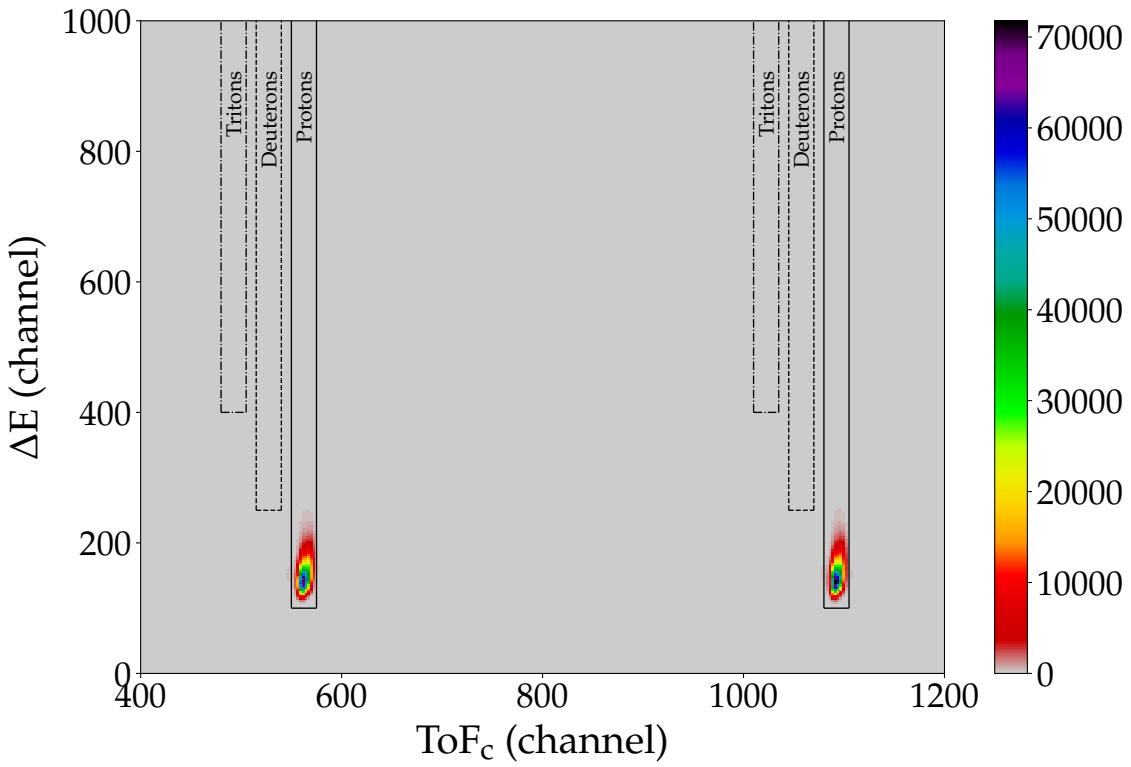

Figure 4.1: Particle identification via energy loss and time of flight (ToF) measurements. Two beam bunches are shown. The time difference between the two bunches corresponds to a beam pulse period of ca. 60 ns.

In Fig. 4.1 a two dimensional plot is shown, where energy loss ΔE in the plastic scintillator is plotted against the time of flight $\mathrm{ToF_c}$. The proton scattering events, framed by solid lines, can be clearly identified. Predicted regions for deuteron and triton events are indicated by dashed and dot-dashed lines respectively. However, neither deuterons nor tritons were detected in this experiment.

4.2 VDC data analysis

The detector system of the Grand Raiden Spectrometer was already introduced in Section 3.2. In the following subsections the ray tracking and the efficiency of the drift chambers will be discussed in detail.

4.2.1 Track reconstruction

In Fig. 4.2 a schematic view of a VDC plane is shown. Charged particles passing through a drift chamber produce electron-ion pairs along their tracks by ionising the working gas within the drift chamber. The electrons drift in the electric field of the drift chamber with a constant velocity to the nearest sense wires and produce a measurable signal there. The drift time, which

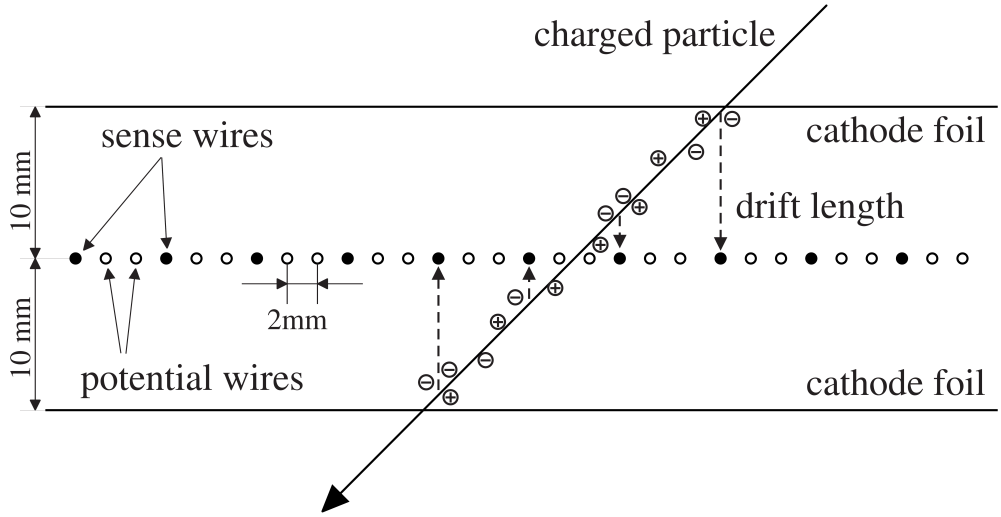

Figure 4.2: Schematic view of a VDC plane. The track of a charged particle passing through the drift chamber is indicated [90].

is the time difference of the trigger signal of the plastic scintillator and the wire signal, is measured using time to digital converters (TDC). The vertical drift length can then be calculated from the drift times. An example for such a conversion is shown in Fig. 4.3. Usually the inelastically scattered protons enter the drift chambers under a tilted angle so that a signal at multiple wires is detected. Those multiple wire hits are grouped into clusters with a minimum of 2 hits and a maximum of 5 hits per cluster. The position of the proton where it crosses the wire plane is calculated from the drift lengths to the hit wires by performing a least-squares fit analysis. Finally, the trajectory of the incident proton is calculated by combining the deduced positions at all four wire planes of the drift chambers.

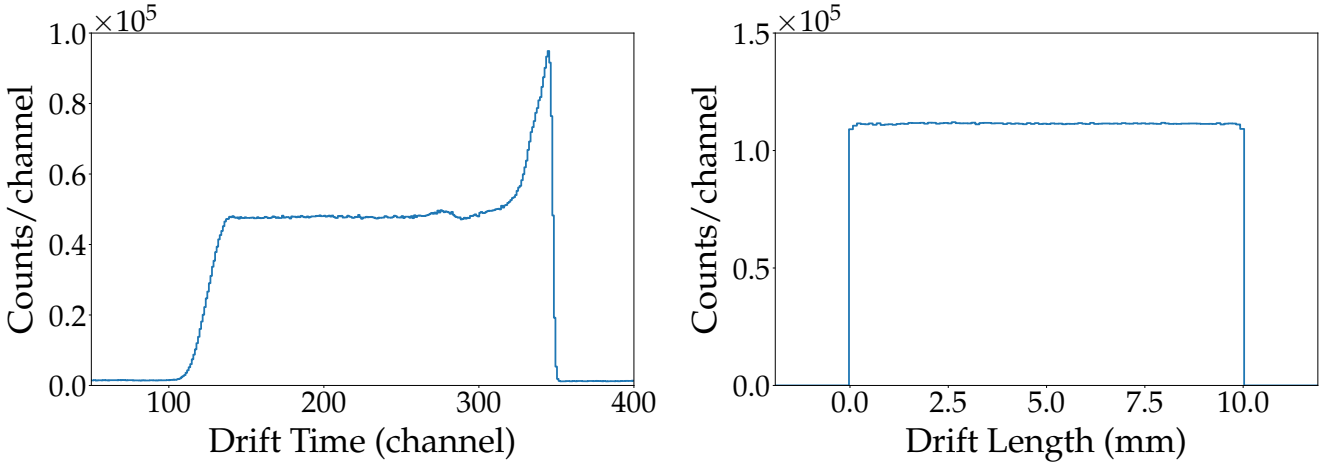

Figure 4.3: An example for a drift time to drift length conversion. The prominent peak in the left plot around channel 345 is formed due to the inhomogeneity of the electric field close to the anode wires.

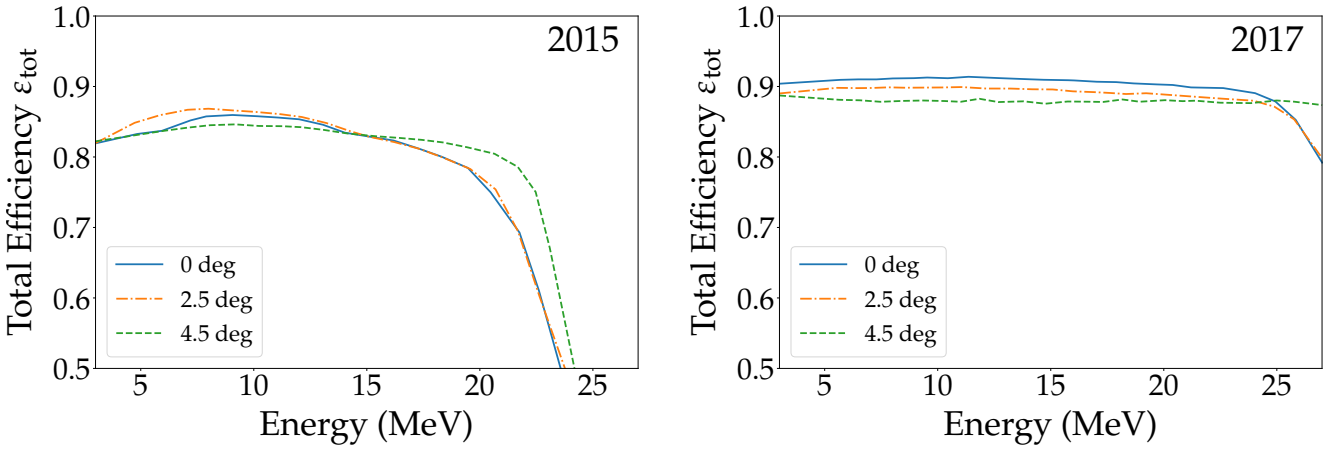

Figure 4.4: Total tracking efficiency as a function of the excitation energy.

4.2.2 Tracking efficiency

The efficiency for each drift chamber plane was calculated separately. As an example the efficiency calculation for the X1 plane is given by the equation

$$\varepsilon_{\mathrm{X1}} = \frac{N_{\mathrm{X1,X2,U1,U2}}}{N_{\mathrm{X1,X2,U1,U2}} + N_{\overline{\mathrm{X1}},\mathrm{X2,U1,U2}}}, \tag{4.2}$$

where $N_{\mathrm{X1,X2,U1,U2}}$ is the number of events with successfully reconstructed position of the proton in all four planes and $N_{\overline{\mathrm{X1}},\mathrm{X2,U1,U2}}$ is the number of events with successfully reconstructed position of the proton in all planes except the X1 plane. The product of the efficiencies of all four planes yields the total tracking efficiency

$$\varepsilon_{\mathrm{tot}} = \varepsilon_{\mathrm{X1}}\varepsilon_{\mathrm{X2}}\varepsilon_{\mathrm{U1}}\varepsilon_{\mathrm{U2}}. \tag{4.3}$$

In previous experiments [90, 94] it was shown and in later experiments [95–99] assumed that the total efficiency is approximately constant over the measured energy range. However, this is not always the case as was recently shown in Ref. [100]. Fig. 4.4 shows the typical efficiency for different scattering angles as a function of the excitation energy for the experimental campaigns in 2015 and 2017. Indeed the efficiency was rather constant over the whole energy range in the 2017 campaign. During the experimental campaign in 2015 the efficiency had a considerable dependence on the excitation energy. Therefore the analysis of the measured data was performed using an energy dependent efficiency instead of a constant one.

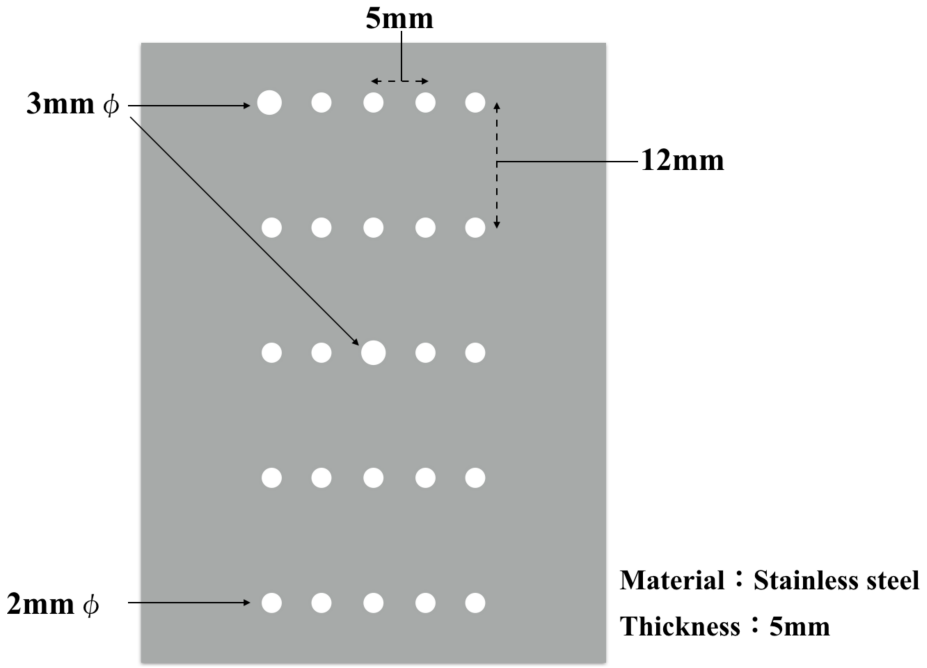

Figure 4.5: Schematic drawing of the used sieve slit. The centre hole and the upper left hole are slightly bigger in diameter for better handling [101].

4.3 Scattering angle calibration

Due to the complex ion-optical properties of the Grand Raiden Spectrometer, a calibration of the scattering angle is necessary. For this purpose sieve slit measurements were performed during both experimental campaigns. In these measurements a ^{58}Ni target was used and the spectrometer was set to an angle of 16°. The sieve slit is a metal plate with a total of 25 holes arranged in a 5×5 matrix. During the measurements it was mounted at the GR entrance 585 mm downstream of the target. A schematic drawing of the sieve slit is depicted in Fig. 4.5.

In order to investigate the dependence of the scattering angle on the horizontal position at the focal plane, several measurements with different settings of the magnetic field were performed. In 2015 the magnetic field was increased by 1.2 %, 1.8 %, 2.6 %, 3.2 % and 4.2 % with respect to the magnetic field used normally during the experiment. In 2017 the magnetic field was increased by 0 %, 1.2 %, 1.8 %, 2.6 % and 3.4 %. With these measurements the entire momentum acceptance of the spectrometer could be covered. Additionally, the vertical beam position at the target was changed by 0 and ± 1 mm relative to the centre, so that three measurements per magnetic field setting were realised. In total 15 measurements per experimental campaign were taken.

With the help of the sieve slit data, the horizontal θ_t and vertical ϕ_t scattering angles at the target position can be reconstructed by a multidimensional least-squares fitting analysis. For this analysis the knowledge of five parameters is required, namely the horizontal θ_{fp} and

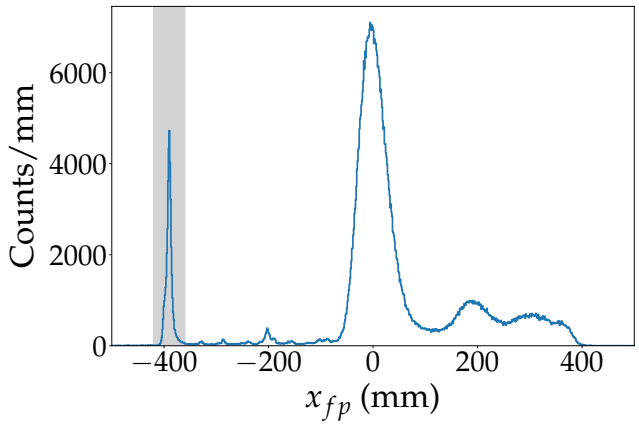

(a) Horizontal position spectrum. The gate on elastic scattering events used for the sieve slit analysis is shaded in gray.

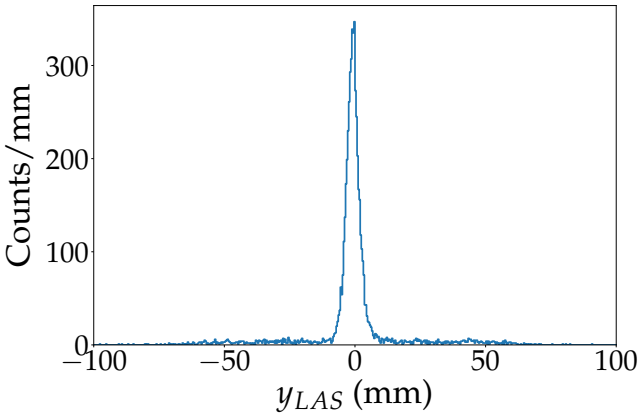

(b) Vertical beam spot position at the target was obtained with the Large Acceptance Spectrometer.

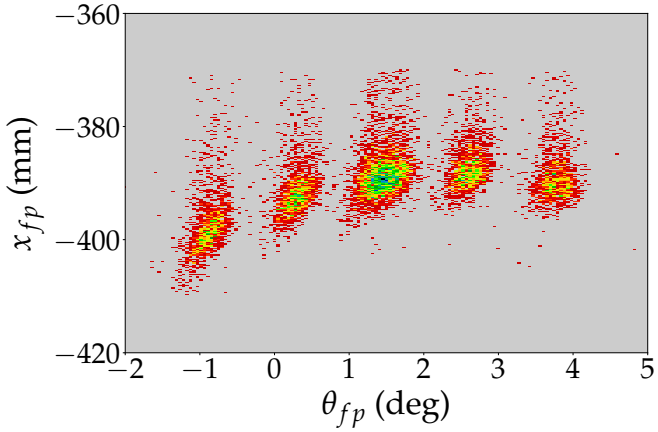

(c) Horizontal position and incidence angle were extracted using a two-dimensional asymmetric Gaussian fit. A gate on ϕ_{fp} is applied.

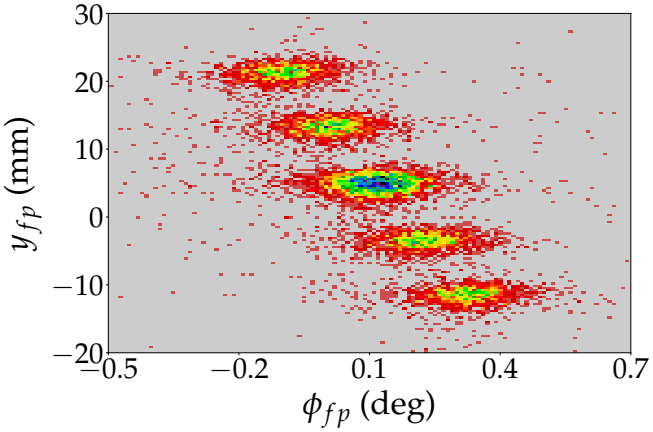

(d) Same as c), but for vertical position and incidence angle. A gate on θ_{fp} is applied.

Figure 4.6: Extraction of the parameters θ_{fp}, ϕ_{fp}, x_{fp}, y_{fp} and y_{LAS} necessary for the sieve slit analysis.

vertical ϕ_{fp} incidence angles at the focal plane, the horizontal x_{fp} and vertical y_{fp} positions at the focal plane as well as the vertical beam spot position at the target y_{LAS}, which was measured using the Large Acceptance Spectrometer. Prior to the extraction of these parameters a gate on elastic scattering events was set as shown in Fig. 4.6(a). The vertical beam spot position at the target y_{LAS} was measured by the LAS and was extracted by fitting a Gaussian to the data shown in Fig. 4.6(b). The parameters x_{fp} and θ_{fp} were determined using a two-dimensional asymmetric Gaussian function, cf. Fig. 4.6(c). The two-dimensional Gaussian function was defined as

$$f(x,y) = A\exp[-(a(x-x_0)^2 + 2b(x-x_0)(y-y_0) + c(y-y_0)^2)], \tag{4.4}$$

with

$$a = \frac{\cos^2\theta}{2\sigma_x^2} + \frac{\sin^2\theta}{2\sigma_y^2}, \quad b = -\frac{\sin 2\theta}{4\sigma_x^2} + \frac{\sin 2\theta}{4\sigma_y^2}, \quad c = \frac{\sin^2\theta}{2\sigma_x^2} + \frac{\cos^2\theta}{2\sigma_y^2}, \tag{4.5}$$

where A, x_0, y_0, σ_x, σ_y and θ were fit parameters. In the same way y_{fp} and ϕ_{fp} were determined, cf. Fig. 4.6(d). With the extracted parameters, the horizontal and vertical scattering angles at the target can be determined via a multidimensional least-squares fitting analysis using the following equations

$$\theta_t = \sum_{i=0}^{1}\sum_{j=0}^{1} a_{ij} x_{fp}^i \theta_{fp}^j, \tag{4.6}$$

$$\phi_t = \sum_{i=0}^{1}\sum_{j=0}^{1}\sum_{k=0}^{1}\sum_{l=0}^{1} b_{ijkl} x_{fp}^i \theta_{fp}^j y_{fp}^k \phi_{fp}^l + \sum_{m=0}^{1} c_m x_{fp}^m y_{LAS}, \tag{4.7}$$

where a_{ij}, b_{ijkl} and c_m were fit parameters. The resulting coefficients are listed in Table 4.1 for both experimental campaigns. Fig. 4.7 shows an example of the reconstruction of the horizontal and vertical scattering angles. The data shown correspond to magnetic field settings of +1.2 %, +1.8 % and +2.6 % with respect to the magnetic field used normally during the experiment in 2017. It can be seen that the reconstruction process works very well over the whole momentum acceptance of the spectrometer. Similar results were obtained for the experimental campaign in 2015. By fitting a two dimensional Gaussian to each of the reconstructed holes one can estimate the resolution for both, the horizontal θ_t and vertical ϕ_t scattering angles. During both experimental campaigns similar resolutions were achieved with 0.15 ± 0.01 deg (FWHM) for the horizontal scattering angle and 0.5 ± 0.1 deg (FWHM) for the vertical scattering angle. The systematic uncertainties were determined in the following way. The areas spanned by four neighbouring holes were calculated for the reconstructed hole positions and for the true hole positions, respectively. The comparison of these areas gave then an estimation for the systematic uncertainties. These were around 4 % in 2015 and 5 % in 2017.

Table 4.1: Coefficients a_{ij}, b_{ijkl} and c_m from Eqs. (4.6) and (4.7) for the reconstruction of the horizontal and vertical scattering angles. The numbers of i, j, k and l represent the exponent of x_{fp}, y_{fp}, θ_{fp}, and ϕ_{fp}, respectively. All angles are given in radian and all distances in millimetres.

ij	a_{ij} (2015)	a_{ij} (2017)
00	2.970×10^{-2}	2.134×10^{-2}
01	-4.214×10^{-1}	-4.435×10^{-1}
10	3.917×10^{-5}	2.686×10^{-5}
11	2.222×10^{-5}	-3.340×10^{-6}

$ijkl$	b_{ijkl} (2015)	b_{ijkl} (2017)
0000	-3.739×10^{-4}	1.523×10^{-3}
0001	$2.443 \times 10^{+0}$	$1.712 \times 10^{+0}$
0010	-1.586×10^{-3}	-2.598×10^{-3}
0011	-1.667×10^{-2}	9.648×10^{-3}
0100	9.676×10^{-3}	9.773×10^{-3}
0101	$2.373 \times 10^{+1}$	$2.455 \times 10^{+1}$
0110	8.664×10^{-3}	8.873×10^{-3}
0111	1.912×10^{-1}	-2.223×10^{-1}
1000	1.440×10^{-5}	8.486×10^{-6}
1001	-5.290×10^{-3}	-4.624×10^{-3}
1010	-2.143×10^{-6}	-1.938×10^{-6}
1011	-5.492×10^{-5}	3.167×10^{-5}
1100	2.212×10^{-4}	4.693×10^{-6}
1101	3.869×10^{-3}	2.699×10^{-2}
1110	-4.128×10^{-6}	4.031×10^{-6}
1111	5.909×10^{-4}	-2.755×10^{-4}

m	c_m (2015)	c_m (2017)
0	-6.870×10^{-4}	-1.297×10^{-3}
1	-8.405×10^{-7}	-4.388×10^{-7}

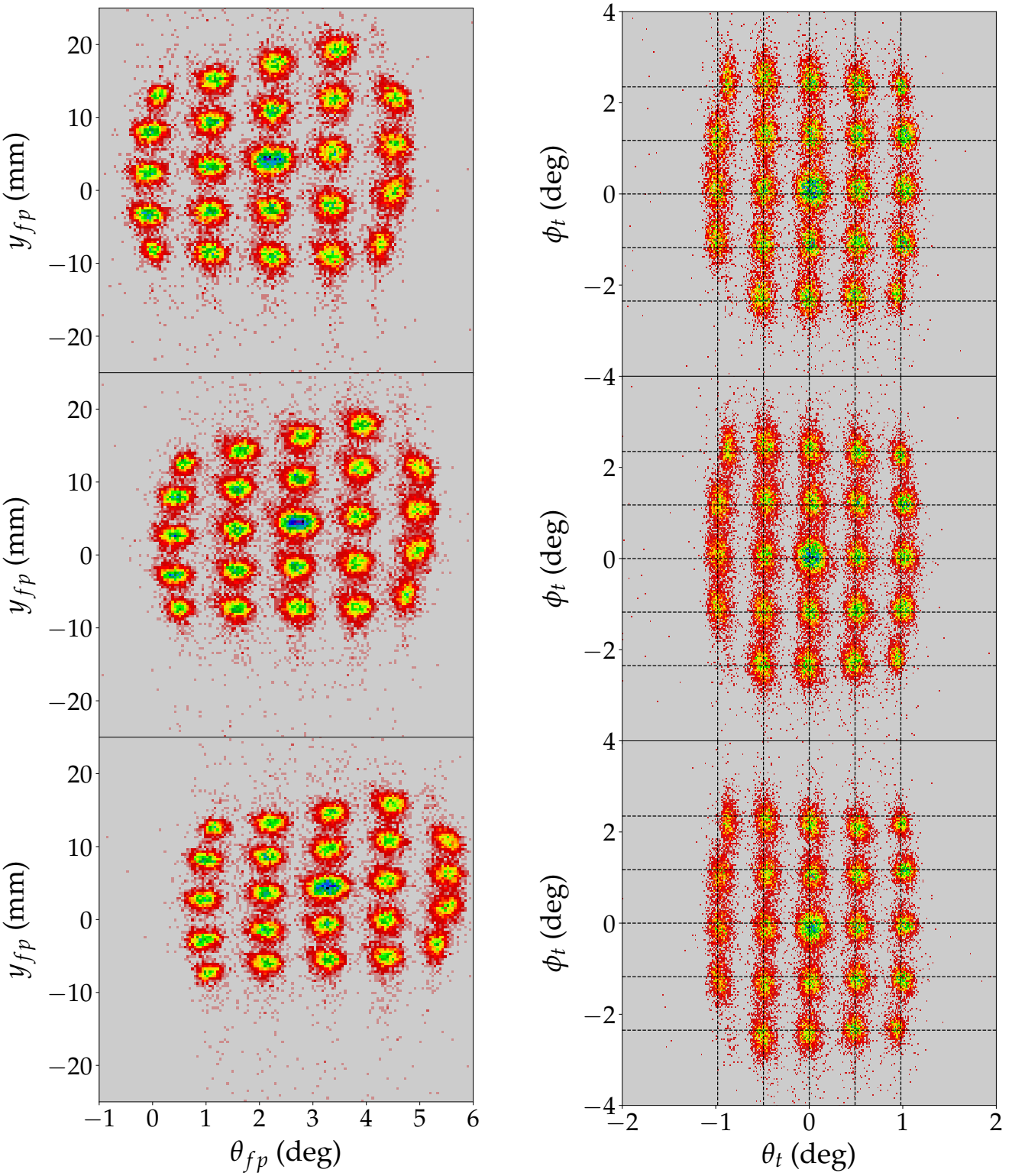

Figure 4.7: Example of the reconstruction of the horizontal and vertical scattering angles. Two dimensional sieve slit data before (left) and after (right) the reconstruction of the scattering angles at the target position are shown. The intersections of the dashed lines indicate the true positions of the sieve slit holes.

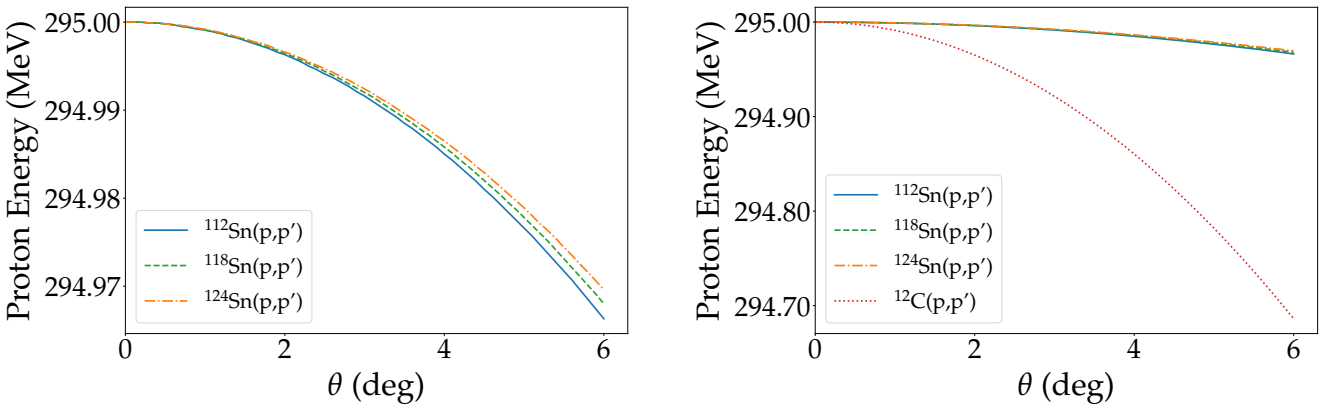

Figure 4.8: Energy dependence of scattered protons on the scattering angle due to recoil effects of different nuclei. For better visibility only three selected tin isotopes are shown.

4.4 Energy calibration

Before the energy calibration can be applied, certain corrections have to be employed to reach the best possible energy resolution, namely the kinematical correction and the aberration correction.

The energy of scattered protons depends on the scattering angle due to recoil effects of the target nuclei in the reaction kinematics. To investigate this recoil effects, calculations for different nuclei were performed using the reaction code *KINMAT* [102]. Results are shown in Fig. 4.8. The recoil off tin nuclei is almost negligible even for higher angles. However, in light nuclei such as carbon, which was used for the energy calibration, the recoil effect is appreciable as shown in the picture. To account for the dependence of the proton energy on the scattering angle, a second order polynomial was fitted to the calculated curves

$$E(\theta) = a\theta^2 + b\theta + c, \tag{4.8}$$

where a, b and c were fit parameters. The obtained parameters are summarised in Table 4.2. The recoil effect was then corrected via the equation

$$x_k = x_{fp} + \frac{a\theta^2 + b\theta}{k} \quad \text{with} \quad \theta = \sqrt{(\theta_t + \theta_{gr})^2 + \phi_t^2}, \tag{4.9}$$

where a and b are the parameters from Table 4.2 and x_{fp} is the position of the scattered proton at the focal plane. θ_t and ϕ_t are the horizontal and vertical scattering angles at the target position and θ_{gr} indicates the angle at which the Grand Raiden Spectrometer was set. The

Table 4.2: Fit parameters for Eqn. (4.8).

Isotope	a in MeV/deg^2	b in MeV/deg	c in MeV
^{112}Sn	-9.356×10^{-4}	-4.961×10^{-6}	2.950×10^{2}
^{114}Sn	-9.175×10^{-4}	-1.217×10^{-5}	2.950×10^{2}
^{116}Sn	-9.003×10^{-4}	-2.006×10^{-5}	2.950×10^{2}
^{118}Sn	-8.869×10^{-4}	-9.583×10^{-6}	2.950×10^{2}
^{120}Sn	-8.716×10^{-4}	-1.055×10^{-5}	2.950×10^{2}
^{122}Sn	-8.569×10^{-4}	-1.096×10^{-5}	2.950×10^{2}
^{124}Sn	-8.422×10^{-4}	-2.011×10^{-5}	2.950×10^{2}
^{26}Mg	-4.026×10^{-3}	-2.128×10^{-5}	2.950×10^{2}
^{58}Ni	-1.773×10^{-3}	-3.780×10^{-4}	2.950×10^{2}
^{12}C	-8.711×10^{-3}	-6.563×10^{-5}	2.950×10^{2}

parameter k was obtained from a preliminary energy calibration. It was determined to be $k = 0.0235\,\mathrm{MeV/mm}$ for the experimental campaign in 2015 and $k = 0.0233\,\mathrm{MeV/mm}$ in 2017.

A correlation between the horizontal position x_k and the horizontal scattering angle θ_{fp} at the focal plain still remains due to ion-optical properties of the Grand Raiden Spectrometer and needs to be corrected accordingly. On the left side of Fig. 4.9 data for ^{12}C are shown in the $\theta_{fp} - x_k$-plane as well as their projection on the abscissa. One can clearly see the most prominent excited states in ^{12}C around 7.6 MeV, 12.7 MeV and 15.1 MeV. However, they appear as curved lines, which deteriorates the position resolution and hence the energy resolution. To improve the resolution and straighten these lines a polynomial function defined as

$$x_c = \sum_{i=0}^{2} \sum_{j=0}^{4} d_{ij} x_k^i \theta_{fp}^j \tag{4.10}$$

was fitted to each of the lines. The obtained fit parameters d_{ij} are summarised in Table. 4.3. The result of the correction is depicted on the right side of Fig. 4.9. One can see that the resolution is improved considerably after the aberration correction.

For the energy calibration the exact positions x_c of the excited states in ^{12}C were extracted by Gaussian fits. The corresponding energies were taken from Ref. [103]. The relationship between x_c and excitation energy E_x was best described by a second order polynomial

$$\text{2015: } E_x(x_c) = 1.60(8) \times 10^{-6}\,\frac{\mathrm{MeV}}{\mathrm{mm}^2} \cdot x_c^2 + 2.435(4) \times 10^{-2}\,\frac{\mathrm{MeV}}{\mathrm{mm}} \cdot x + 16.426(4)\,\mathrm{MeV} \tag{4.11}$$

$$\text{2017: } E_x(x_c) = 0.30(6) \times 10^{-6}\,\frac{\mathrm{MeV}}{\mathrm{mm}^2} \cdot x_c^2 + 2.333(2) \times 10^{-2}\,\frac{\mathrm{MeV}}{\mathrm{mm}} \cdot x + 16.739(2)\,\mathrm{MeV} \tag{4.12}$$

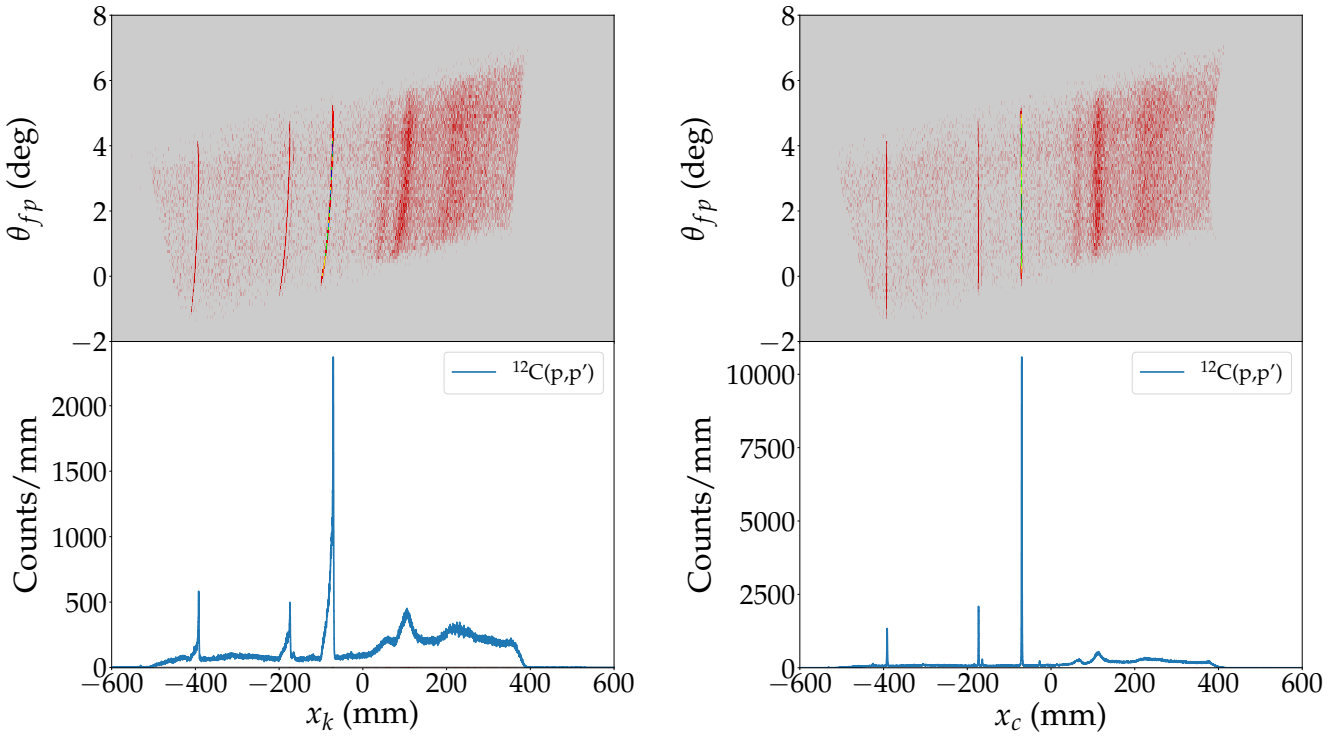

Figure 4.9: ^{12}C data before (left) and after (right) the aberration correction with Eqn. 4.10 using the coefficients from Tab. 4.3.

Table 4.3: Coefficients d_{ij} from Eqn. (4.10) for the aberration correction of the Grand Raiden Spectrometer. The numbers of i and j represent the exponent of x_k and θ_{fp}, respectively. All angles are given in radian and all distances in millimetres.

$i\,j$	d_{ij} (2015)	d_{ij} (2017)
00	$1.167 \times 10^{+2}$	$3.457 \times 10^{+1}$
01	$-4.981 \times 10^{+1}$	$-1.978 \times 10^{+1}$
02	$1.160 \times 10^{+1}$	$5.685 \times 10^{+0}$
03	$-1.539 \times 10^{+0}$	-9.866×10^{-1}
04	7.857×10^{-2}	7.322×10^{-2}
10	$1.295 \times 10^{+0}$	$1.099 \times 10^{+0}$
11	-1.531×10^{-1}	-5.891×10^{-2}
12	3.422×10^{-2}	1.554×10^{-2}
13	-2.426×10^{-3}	-1.486×10^{-3}
20	2.922×10^{-4}	9.123×10^{-5}
21	-1.646×10^{-4}	-5.809×10^{-5}
22	2.603×10^{-5}	1.134×10^{-5}

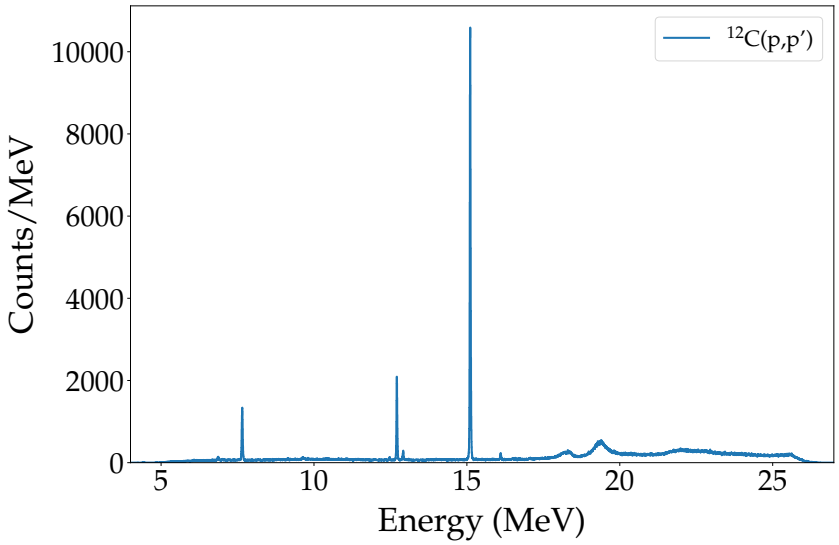

Figure 4.10: Energy calibrated ^{12}C spectrum. The energy resolution is 30 keV (FWHM).

in the experimental campaigns 2015 and 2017, respectively. Using these calibration functions, the reference energies of the known transitions can be reconstructed with an uncertainty of ± 4 keV in the excitation energy region from 5 MeV to 18 MeV. Figure 4.10 shows an energy calibrated ^{12}C spectrum. The achieved energy resolution was 40 keV (FWHM) in 2015 and 30 keV (FWHM) in 2017. As already mentioned in Section 3.3.1, ^{12}C was measured before and after every run of the main targets. On one hand this procedure allows to perform energy calibrations for the main targets, on the other hand possible energy shifts due to instabilities of the proton beam can be detected. The energy shifts were found to be less than 3 keV, which is within the energy calibration uncertainty.

4.5 Background subtraction

To extract background free spectra, a careful and thorough treatment of the experimental background was essential during this analysis. The main contribution of the experimental background came from multiple scattering of incident protons in the target material. But scattering off the beam pipes could also be detected occasionally, especially during the 0° measurements. Due to the statistical nature of multiple scattering, a flat distribution of background events is expected in non-dispersive direction, while true events are concentrated around $y_{fp} = 0$. However, during both experimental campaigns the Grand Raiden Spectrometer was operated in the so called under-focus mode [104] to increase the resolution of the vertical angle. Hence,

Table 4.4: Coefficients e_{ijk} from Eqn. (4.13) for the restoration of the focusing condition at the focal plane. The numbers of i, j and k represent the exponent of x_{fp}, θ_{fp} and ϕ_{fp}, respectively. All angles are given in radian and all distances in millimetres.

ijk	e_{ijk} (2015)	e_{ijk} (2017)
000	$-1.434 \times 10^{+0}$	$-3.607 \times 10^{+0}$
001	$6.658 \times 10^{+2}$	$9.958 \times 10^{+2}$
010	$-3.003 \times 10^{+1}$	$-7.382 \times 10^{+1}$
011	$7.444 \times 10^{+2}$	$8.192 \times 10^{+3}$
100	2.273×10^{-3}	7.444×10^{-3}
101	-1.000×10^{-1}	$-1.624 \times 10^{+0}$
110	3.009×10^{-2}	4.868×10^{-2}
111	$-1.283 \times 10^{+1}$	$-4.875 \times 10^{+0}$
	f (2015)	f (2017)
	6.757×10^{-1}	$1.000 \times 10^{+0}$

before the background can be determined, a correction of y_{fp} needs to be carried out to restore the focusing condition at the focal plane. This can be achieved using the following equations

$$y_c = y_{fp} + \sum_{i=0}^{1}\sum_{j=0}^{1}\sum_{k=0}^{1} e_{ijk} x_{fp}^i \theta_{fp}^j \phi_{fp}^k + f y_{LAS}, \tag{4.13}$$

$$\phi_c = \phi_{fp} + \sum_{i=0}^{1} g_i y_{fp}^i, \tag{4.14}$$

where e_{ijk}, f and g_i are fit parameters. The correction of ϕ_{fp} ensures that the background events are distributed symmetrically around $\phi_c = 0$. This correction has to be applied for every data run separately, though. The obtained fit parameters for the y_{fp} correction are shown in Table 4.4. In Fig. 4.11 the discussed correction is illustrated.

After the correction, the background was determined in the following way. Three data sets were generated as shown in Fig. 4.12. In the first data set a gate was set, so that it contains the true events plus the background events. The second and the third data sets were analysed in exactly the same way as the first one, except that the data were shifted by a constant value along the y_c axis. After the shift, the shown gate only contained background events. The background events from the shifted data sets were then averaged and finally subtracted from the first data set. In such a way a background free spectrum was obtained as depicted in Fig. 4.13. As expected the background from the two shifted data sets was basically the same. It should be noted however, that this was not always the case during this analysis. Deviations in the background between the different shifts occurred in some of the 0° data sets, probably caused by scattering off beam pipes, which leads to contributions in the spectra localised in y_c. In such

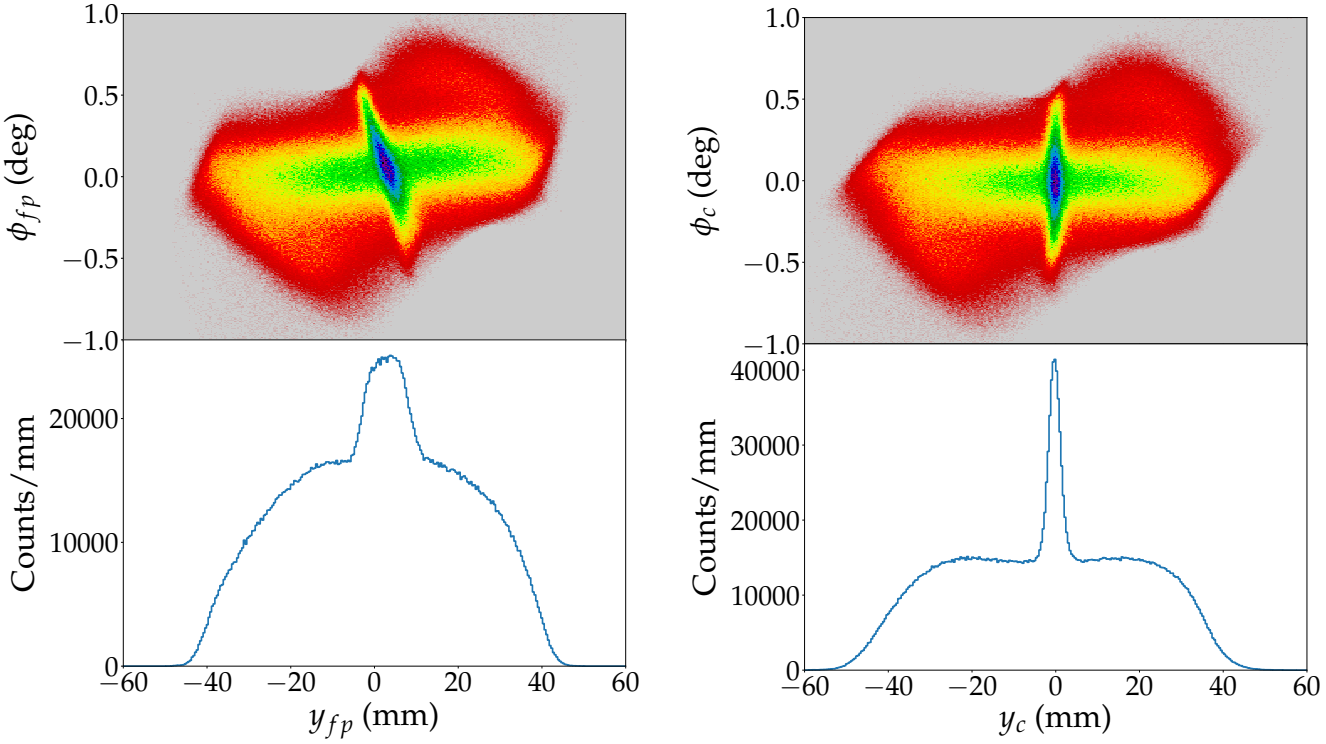

Figure 4.11: Before (left) and after (right) the restoration of the focusing condition at the focal plane. The vertical angle ϕ_{fp} was corrected in such a way that the background events are distributed symmetrically around $\phi_c = 0$.

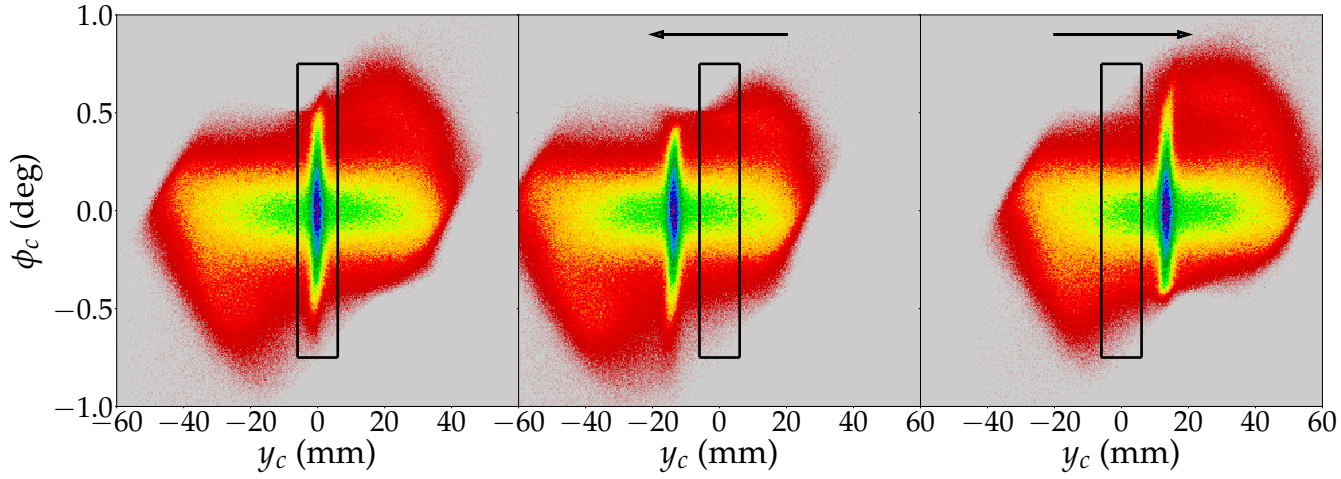

Figure 4.12: Background subtraction procedure. To determine the background, the data were shifted by a constant value in the y_c direction to the left and right, respectively. The black rectangle indicates the chosen gate for the analysis.

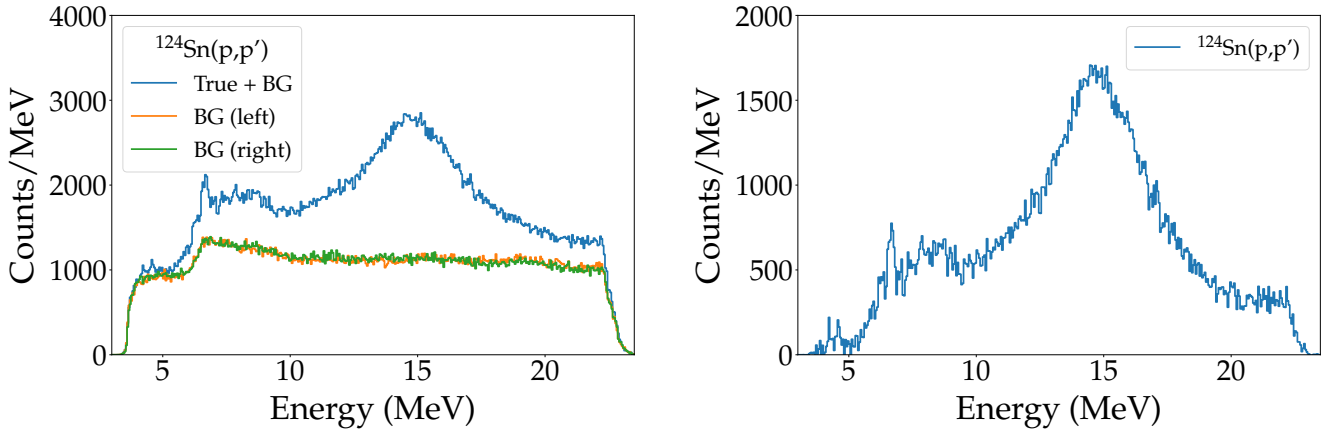

Figure 4.13: Excitation energy spectrum before (left) and after (right) the background subtraction.

cases the background procedure was still applied and the result was compared to data sets, where the background had a flat distribution to verify if the whole background subtraction procedure still works. In most cases the deviations were small and the background procedure was still working satisfactorily. Yet, in some extreme cases data sets were discarded.

4.6 Faraday cup calibration

The experimental set-up contained three different Faraday cups (FC). The 0°-FC was mounted 12 m downstream of the focal plane detector system and was used during the measurements under 0°. The Q1-FC was mounted right behind the first quadrupole magnet placed at the entrance of the Grand Raiden Spectrometer and was used for the 2.5° and 4.5° measurements. Finally, the SC-FC was a moveable Faraday cup, which could be placed directly in the scattering chamber for charge calibration. The SC-FC was calibrated in a previous work [105] and had an absolute efficiency of $c_{SCFC} = 0.986 \pm 0.008$. To account for possible charge loss due to incomplete beam transmission, the charge collections measured with the 0°-FC or the Q1-FC were compared to that of the SC-FC. As it was not possible to obtain the collected charge at all three Faraday cups simultaneously, an indirect measurement was carried out. Beam line polarimeters (BLP) mounted at the entrance of the experimental hall were used to count the scattered protons while a polyethylene target was inserted. The counted BLP events are proportional to the beam charge, so that this proportionality can be used to check the transmission of the beam. During the experiments the BLP target was inserted periodically every 100 s and the scattered protons were counted by the BLP detectors for 10 s. At the end of the beam time, the SC-FC was used under 0°, 2.5° and 4.5° to measure the collected charge while the BLP target was inserted. Then the proportionality factor $x = \frac{\text{BLP counts}}{\text{Charge}}$ was calculated and compared to the regular measurements, where the 0°-FC (Q1-FC) was used. Beam loss could then be determined by calculating the ratio c_{rel} of the 0°-FC (Q1-FC) proportionality factor relative to

Table 4.5: Experimental parameters used to extract the double differential cross sections.

N	measured counts per bin
e	elementary charge
m_A	mass of the target isotope
J	Jacobian determinant for the transformation from lab to c.m. frame
ΔE	energy bin size
Ω	solid angle in the laboratory frame
Q	collected charge
c_{SCFC}	absolute efficiency of the SC-FC
c_{rel}	charge correction relative to the SC-FC due to beam loss
t	target thickness
η	target enrichment
ε	tracking efficiency
L	live time ratio of the data acquisition system

the SC-FC proportionality factor. This ratio should be $c_{rel} = 1$ in the case of a perfect beam transmission and $c_{rel} > 1$ in the case of incomplete beam transmission, respectively. Typical values were $c_{rel} = 1.01$ for the Q1FC and 1.02 for the 0°FC.

4.7 Double differential cross section extraction

The double differential cross sections as well as their statistical and systematic uncertainties were determined using the following equations

$$\frac{\mathrm{d}^2\sigma}{\mathrm{d}\Omega \mathrm{d}E} = \frac{Nem_A J}{\Delta E \Omega Q c_{SCFC} c_{rel} t \eta \varepsilon L}, \tag{4.15}$$

$$\Delta \left.\frac{\mathrm{d}^2\sigma}{\mathrm{d}\Omega \mathrm{d}E}\right|_{stat} = \frac{1}{\sqrt{N}} \frac{\mathrm{d}^2\sigma}{\mathrm{d}\Omega \mathrm{d}E}, \tag{4.16}$$

$$\Delta \left.\frac{\mathrm{d}^2\sigma}{\mathrm{d}\Omega \mathrm{d}E}\right|_{sys} = \sqrt{\sum_i \left(\frac{\Delta X_i}{X_i}\right)^2} \frac{\mathrm{d}^2\sigma}{\mathrm{d}\Omega \mathrm{d}E}, \tag{4.17}$$

where X_i are all uncertainty afflicted experimental parameters from Table 4.5. Major contributions to the systematic uncertainties originate from the solid angle determination ($4-5\,\%$), target thickness ($5\,\%$) and charge collection ($3\,\%$), whereas all other contributions to the systematic uncertainty are below $1\,\%$.

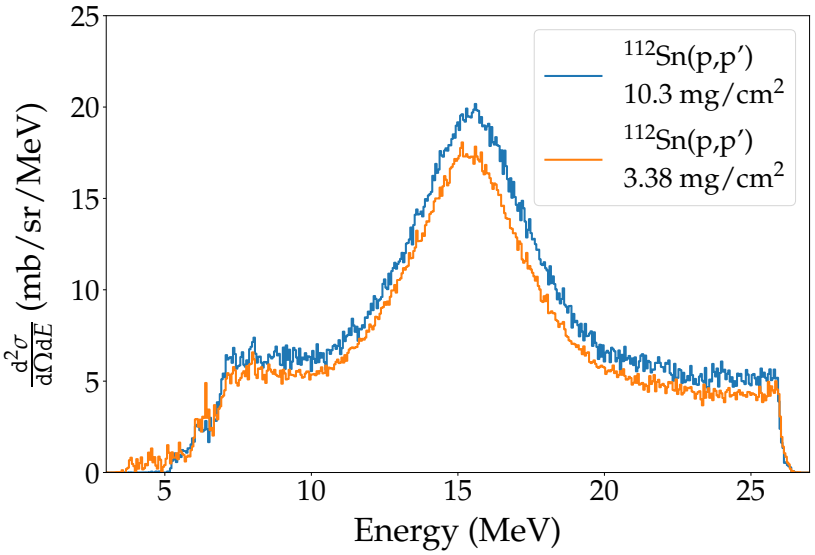

Figure 4.14: Spectra of the ^{112}Sn(p,p') reaction at 0° measured with two different targets. The enrichment was known for the thick target and unknown for the thin one.

4.8 Enrichment of the ^{112}Sn, ^{118}Sn and ^{122}Sn targets

As indicated in Table 3.3, the enrichment was not known for the ^{112}Sn, ^{118}Sn and ^{122}Sn targets. To determine the enrichment for ^{112}Sn, a second target was borrowed. However, this target was much thicker and could be measured only in achromatic mode due to its limited size. Nevertheless, the enrichment for the thin ^{112}Sn target could be determined to $\eta = 90.2(1.4)\,\%$ by normalising it to the measurement with the thick target. In Fig. 4.14 both data sets of ^{112}Sn are shown.

For ^{118}Sn and ^{122}Sn no alternative targets with known enrichment were available, so that only an estimation of the enrichment could be made. A reasonable assumption is that the cross section for all tin isotopes is similar as is the underlying structure of these isotopes. Hence, the enrichments for ^{118}Sn and ^{122}Sn can be estimated from an interpolation of the peak cross sections from the isotopes with the known enrichment. However, the peak cross section might vary due to slightly different width and centroid energy of the GDR. To investigate this issue further, a Lorentzian function was fitted to the GDR region for all tin isotopes and the width Γ_{GDR} as well as the centroid energy E_{GDR} were extracted. These parameters are shown in Fig. 4.15 as a function of the mass number. As expected, the centroid energy is systematically decreasing for heavier isotopes. The same is observed for the widths. However, the width as well as the centroid energy of ^{122}Sn are higher than expected from the seen systematics. Possible explanation for this circumstance could be that the ^{122}Sn target was ^{118}Sn in reality. During the first experimental campaign, short runs on elastic scattering and inelastic scattering at low excitation energies were performed. On the left side of Fig. 4.16 sample data for ^{118}Sn

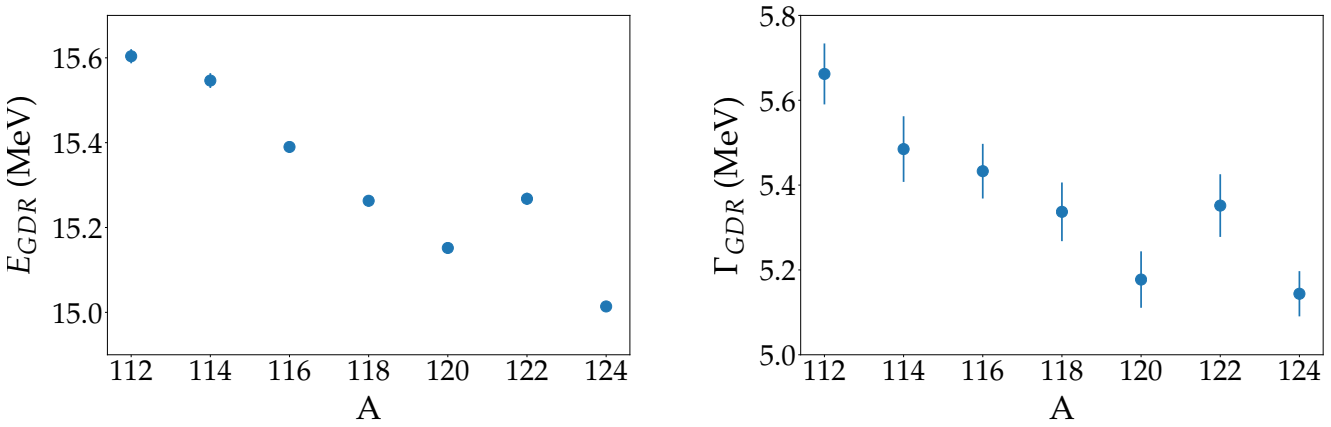

Figure 4.15: The width and centroid energy of the GDR for stable tin isotopes.

and ^{122}Sn are shown. The structures for the isotopes in question appear to be fairly different, so that the statement of ^{122}Sn being in reality ^{118}Sn must be discarded. Moreover, this figure suggests that the ^{122}Sn spectrum contains contributions from different isotopes. On the right side of Fig. 4.16 inelastic scattering data of the ^{122}Sn target are shown with two Lorentzian fits using different parametrisations. In the first fit the expected width and centroid energy for ^{122}Sn were used. In the second fit a combination of Lorentzian functions was used with fixed Γ_{GDR} and E_{GDR} parameters for the corresponding isotopes. Furthermore, each Lorentzian was weighted with the natural abundance of the respective tin isotope. As shown in the picture this function provides an excellent description for the ^{122}Sn data. This leads to the conclusion that the ^{122}Sn target had a natural composition of isotopes. Therefore these data could not be used for further analysis.

Finally, the enrichment for ^{118}Sn was estimated as follows. To account for the different centroid energy and width of the GDR, a Lorentzian function was fitted to each of the

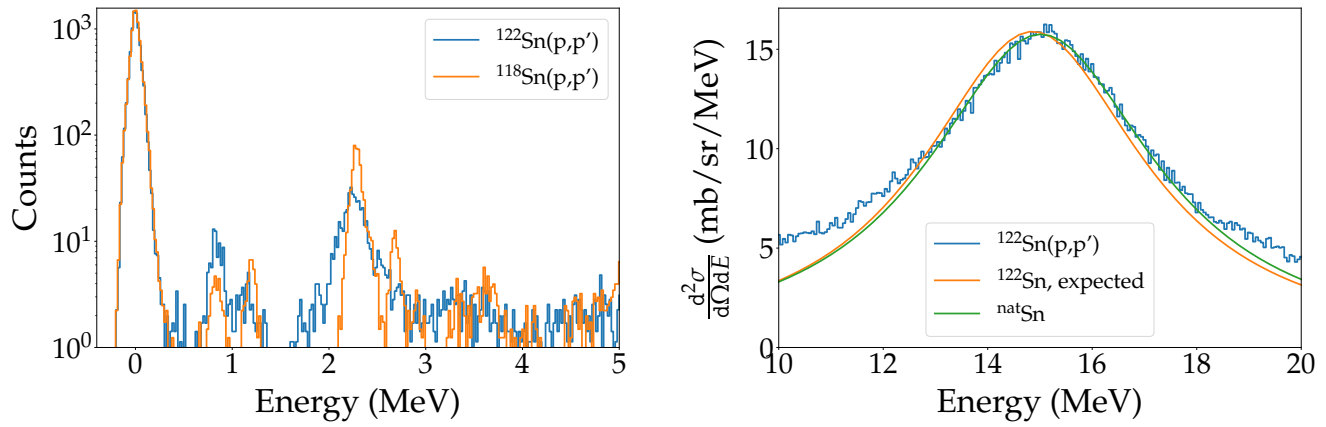

Figure 4.16: Inelastic proton scattering data at low excitation energies for the ^{118}Sn and ^{122}Sn targets (left). Spectrum of the GDR region of the ^{122}Sn target (right).

^{112,114,116,120,124}Sn isotopes and integrated thereafter. By interpolating these integrated values, the enrichment for ^{118}Sn was then determined to be $\eta = 86(7)$ %.

5 Multipole decomposition analysis

5.1 Introduction

The double differential cross sections extracted as described in the previous chapter are presented for the measured angles of 0°, 2.5° and 4.5° in Fig. 5.1. Data under 4.5° are missing for ^{114}Sn due to beam time shortage. For ^{124}Sn, data under 4.5° were only taken in the first experimental campaign in 2015. Therefore the excitation energy spectrum for this angle is only available up to about 23.5 MeV, due to different magnetic field settings. In all isotopes, the GDR can be identified around 15 MeV. In the PDR region between 6 and 10 MeV, a structure can be seen becoming gradually more pronounced for heavier isotopes culminating in ^{124}Sn, where even distinct peaks are formed. The typical decrease of the cross section with increasing angle due to dominant Coulomb excitation is apparent.

In the next step, a multipole decomposition analysis (MDA) is performed in order to extract E1 and M1 cross sections. This method is well established in the analysis of charge exchange reactions [106, 107], aiming at the extraction of the Gamow-Teller strength, but also in inelastic alpha scattering [108–110] used to study isoscalar giant resonances. It was also shown to be a reliable tool in the analysis of inelastic proton scattering data [72, 73, 111].

5.2 Theoretical angular distributions

Theoretical angular distributions of the differential cross sections for different multipolarities were calculated using the code *DWBA07* [112]. Transition amplitudes and single-particle wave functions obtained from QPM calculations were used as input. Furthermore, the parametrisation of Love and Franey [60] was employed to describe the effective nucleon-nucleon interaction. An example of the angular distributions of different multipolarities is shown in Fig. 5.2 for ^{120}Sn. The shape of the curves suggests that E1 and M1 are dominant under small angles, whereas higher multipolarities, such as E2, M2 and E3 are only relevant for larger angles. The results obtained for ^{120}Sn were also used for the MDA of all other tin isotopes, since the underlying structure for the tin isotopes studied in this work is very similar and the angular distributions of collective modes show a weak dependence on mass number [113]. The theoretical curves were, however, corrected for the kinematical effect arising from slightly different isotope masses and convoluted with the experimental angular resolution.

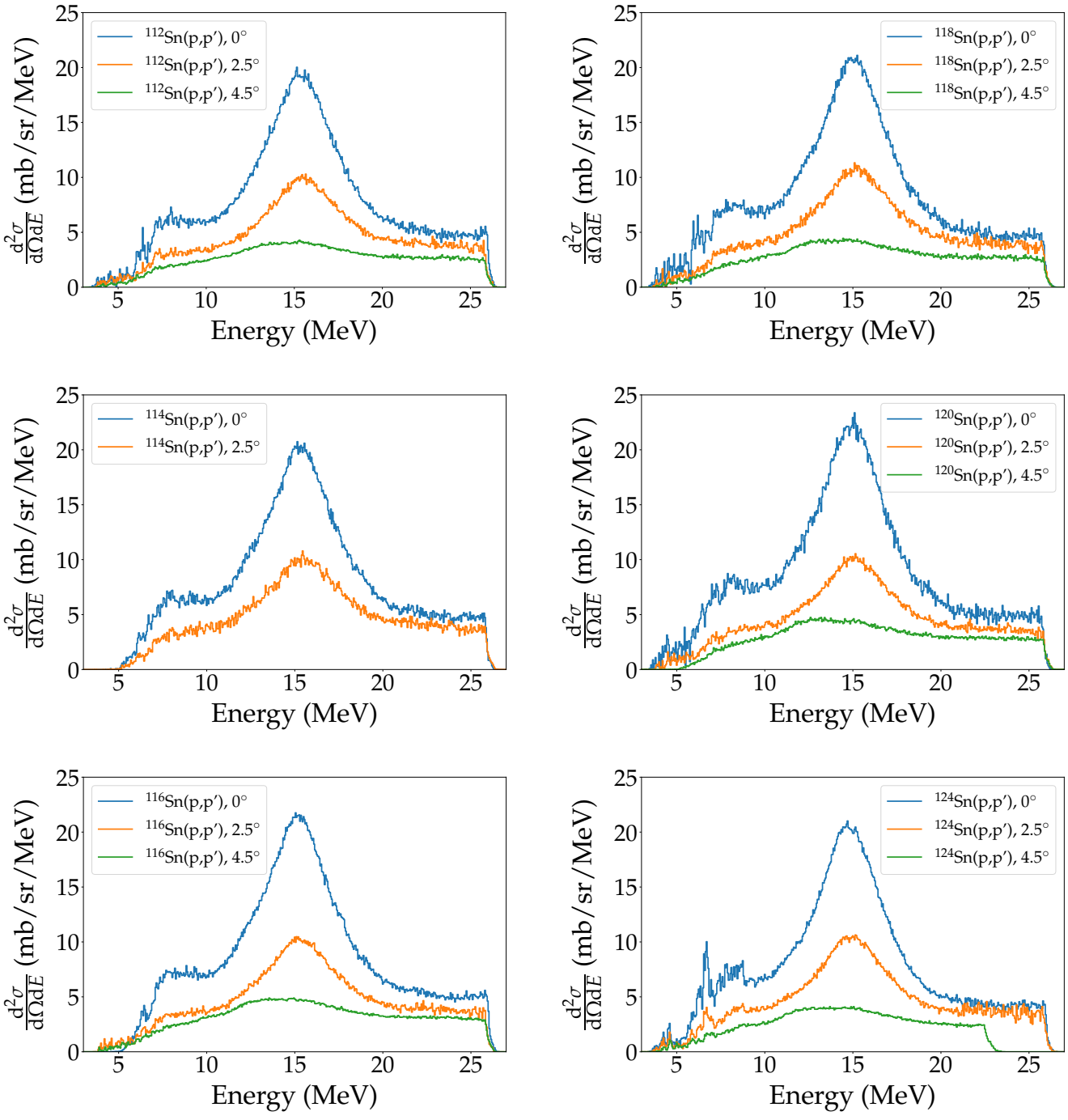

Figure 5.1: Double differential cross sections for the measured tin isotopes.

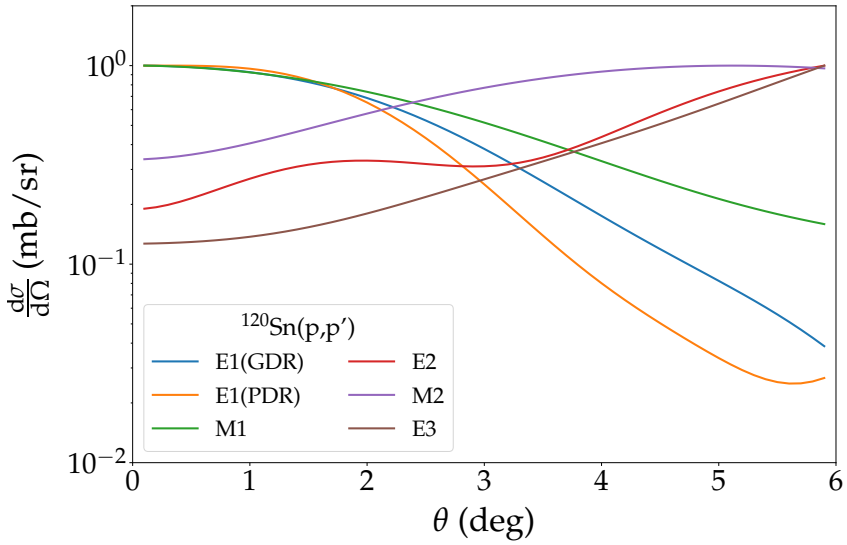

Figure 5.2: Angular distributions of different multipolarities calculated with the code *DWBA07* for ^{120}Sn. The maxima of the curves were normalised to unity.

5.3 Subtraction of the ISGMR and ISGQR

Including various multipolarities increases the complexity of the MDA. To obtain reliable results without neglecting any potentially important contributions to the experimental cross sections, the isoscalar giant monopole (ISGMR) and quadrupole (ISGQR) resonances were subtracted prior to the MDA. Information on this modes for all tin isotopes in question are available from (α,α') experiments [109]. An example for ^{120}Sn is shown in Fig. 5.3. The contribution of the ISGMR and ISGQR to the proton scattering cross sections can be estimated with the following equation

$$\frac{d\sigma}{d\Omega}(\theta, E_x) = \frac{d\sigma}{d\Omega}(\theta)_{DWBA} \frac{B(E\lambda)(E_x)_{(\alpha,\alpha')}}{B(E\lambda)_{QPM}}, \tag{5.1}$$

where $B(E\lambda)(E_x)_{(\alpha,\alpha')}$ is the strength distribution from alpha scattering experiments and $B(E\lambda)_{QPM}$ is the theoretical strength from QPM calculations with $\lambda = 0$ for ISGMR and $\lambda = 2$ for ISGQR, respectively. Here, the basic idea is to make use of the fact that the ratio of the cross section and strength are the same for theory and experiment assuming similar exhaustion of the sum rule [113]. The theoretical strength distribution was calculated within the QPM and was then utilised to calculate the cross section using the *DWBA07* code. The resulting cross sections $\frac{d\sigma}{d\Omega}(\theta)_{DWBA}$ are shown in Fig. 5.4. The ISGMR is dominant under small angles, whereas the ISGQR becomes more important with increasing angle, especially for $\theta \gtrsim 4°$. Finally, in Fig. 5.5 the proton scattering cross sections as well as the estimated contributions of the isoscalar giant monopole and quadrupole resonances are presented. The expected contributions are rather

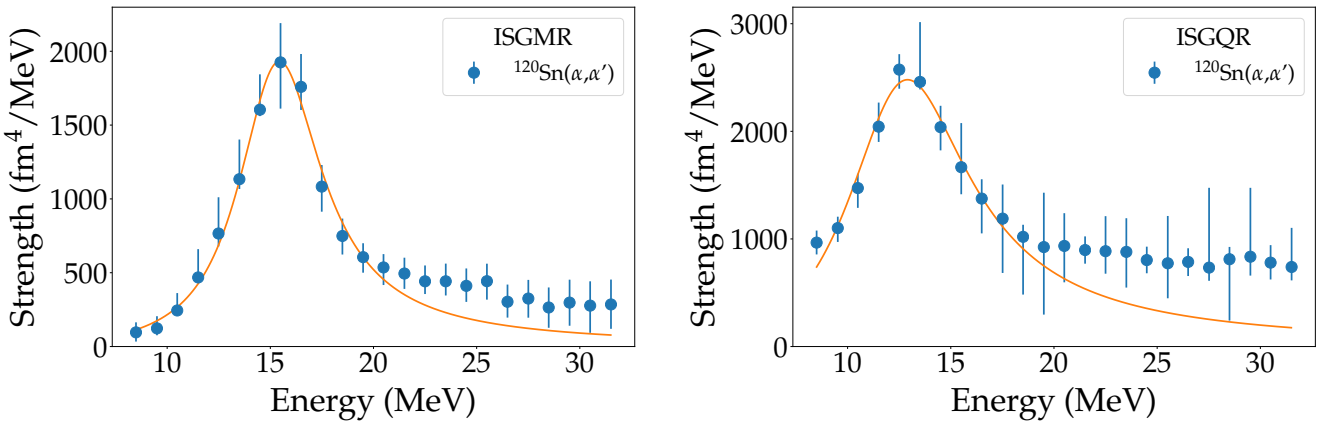

Figure 5.3: Strength distribution of the isoscalar giant monopole (left) and quadrupole (right) resonances in ^{120}Sn from alpha scattering experiments [109]. A Lorentzian fit to the experimental data is also shown.

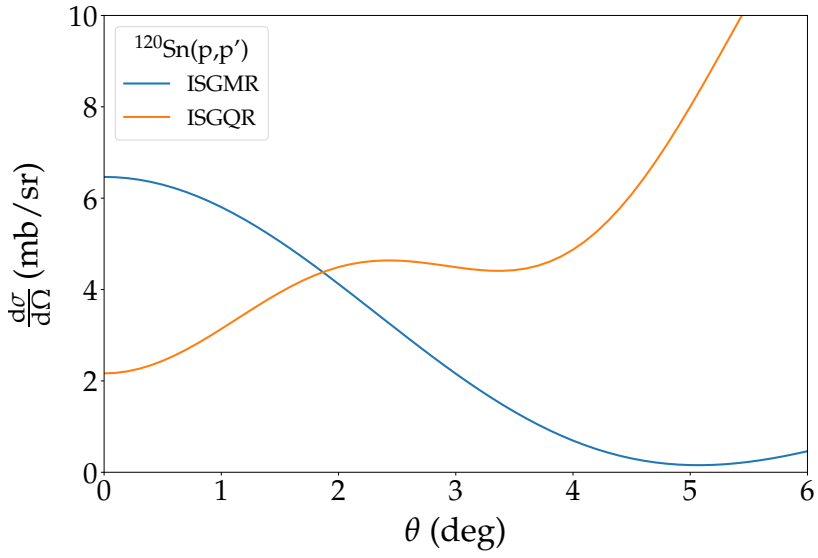

Figure 5.4: Theoretical cross section of the isoscalar giant monopole and quadrupole resonances for ^{120}Sn calculated with the *DWBA07* code.

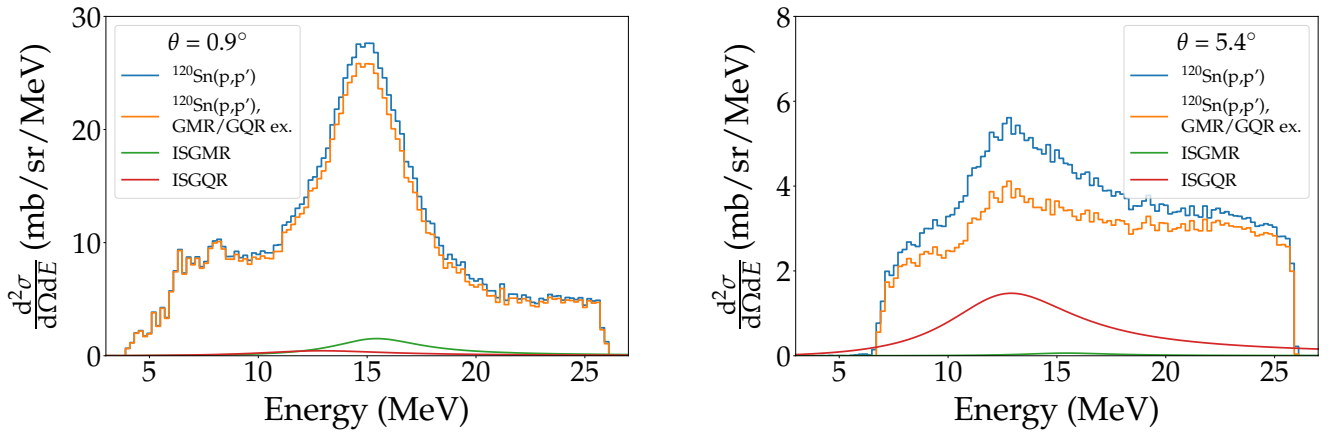

Figure 5.5: Proton scattering cross section with and without the contributions of the ISGMR and ISGQR for two different angles. The ISGMR and ISGQR contributions were estimated using Eqn. (5.1).

small for small angles. For larger angles however, a considerable contribution from the ISGQR is found. After the subtraction of the ISGMR and ISGQR contributions a bump around 13 MeV can still be seen for the 5.4° data. This suggests that the absolute cross section of the ISGQR might be underestimated, though possible contributions from higher multipolarities, such as M2 and E3, were not considered yet which could possibly explain the remaining bump. It should be noted, that only the Lorentzians as shown in Fig. 5.3 were used for subtraction, because at higher excitation energies other contributions than the giant resonances are included in the ISGMR and ISGQR strength distributions.

5.4 Background from quasi-free scattering

Quasi-free scattering (QFS) refers to reactions in which the incident projectile scatters off of a single nucleon in the target nucleus. This process occurs only at energies above the proton/neutron thresholds and needs to be accounted for in the MDA. In Ref. [96] Poltoratska determined the QFS contribution for ^{208}Pb. In a similar way the contribution from quasi-free scattering was determined in this work using ^{120}Sn spectra. ^{120}Sn was chosen, because it is the heaviest measured nucleus with data available for all three measured angles in the high excitation energy region, where possible contributions from the high-energy tail of the GDR are negligible. The data were rebinned to 1 MeV bins to reduce statistical fluctuations and angular distributions in the energy region between 22.5 and 25.5 MeV were extracted. In this energy region no contributions other than that from quasi-free scattering are expected. The angular distributions were then fitted by polynomial functions of second order. Since these were almost identical for all bins in the selected energy region, an average polynomial function was determined

$$\frac{\mathrm{d}\sigma}{\mathrm{d}\Omega}(\theta) = 5.7(3) - 1.0(2) \cdot \theta + 0.09(3) \cdot \theta^2. \tag{5.2}$$

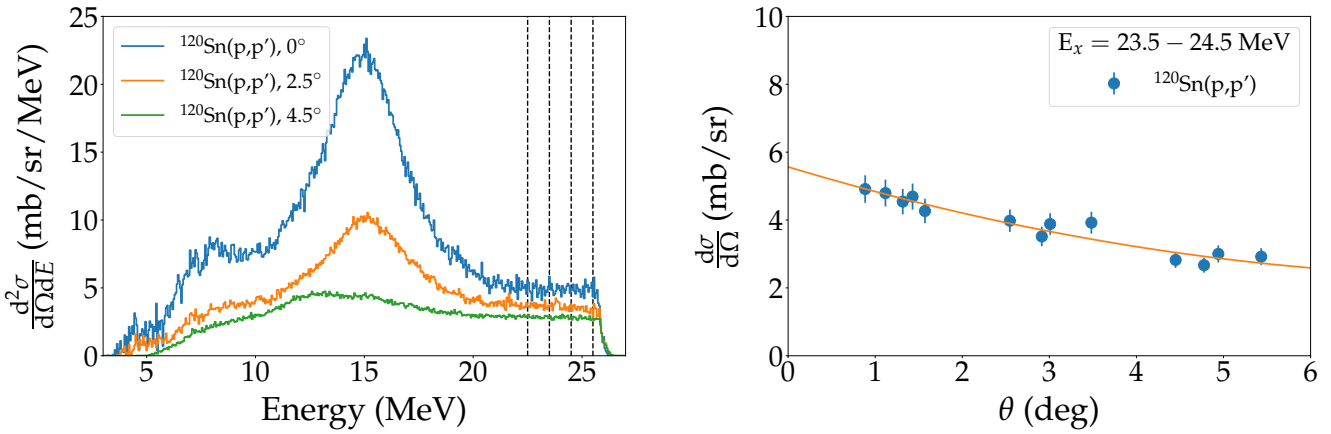

Figure 5.6: Excitation energy spectrum of ^{120}Sn for the three measured angles (left) and the corresponding angular distribution for one of the bins (right).

In Fig. 5.6 the used ^{120}Sn data are shown on the left side. The energy bins chosen for the angular distributions are indicated by dashed lines. On the right side the angular distribution for one of the bins is shown together with a polynomial fit to the data.

Though the contribution of quasi-free scattering could be derived for ^{120}Sn as described above, an analytical function describing the QFS as a function of nucleus, angle and possibly excitation energy would be desirable. Systematic studies of QFS were conducted by Kalbach [114] for different nuclei using data from (p,p′) and (p,n) experiments over a wide incident energy range. Kalbach could derive an analytical function describing the QFS as a function of nucleus, angle, excitation energy and proton energy. A comparison between the parametrisation derived in this work and the parametrisations from Poltoratska [96] and Kalbach [114] are shown in Fig. 5.7. The parametrisation of Poltoratska was initially derived from an inelastic scattering experiment on ^{208}Pb, but was kinematically corrected here to account for a possible mass dependence of the QFS. The parametrisation derived in this work is consistent with the one of Poltoratska. Although the fall off of both curves is slightly different, both show an increased cross section for smaller angles. The parametrisation of Kalbach shows a completely different trend. As data for scattering angles near 0° were not available in the systematic studies conducted by Kalbach, the derived parametrisation is to be handled with caution and is strictly valid only between 16° and 80° in the centre of mass system [114].

5.5 Results of the MDA

For the MDA all spectra were rebinned to 200 keV and the ISGMR and ISGQR contributions were subtracted as described in Section 5.3. Experimental angular distributions of the differential cross sections for each bin were then determined and the data were fitted by means of a

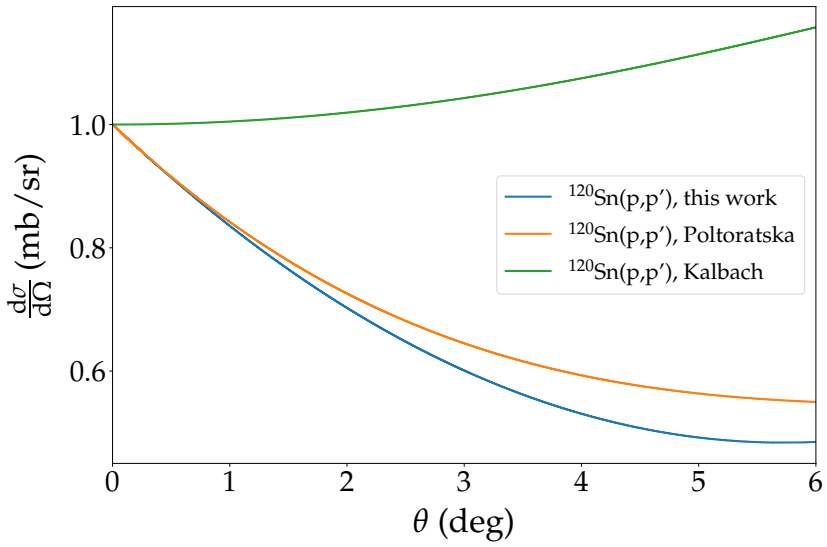

Figure 5.7: Comparison between the parametrisations of the quasi-free scattering from this work, Poltoratska [96] and Kalbach [114]. All curves were normalised to unity at 0°.

least-squares method with linear combinations of the theoretically predicted angular distributions of the differential cross sections via

$$\frac{d\sigma}{d\Omega}(\theta, E_x)_{exp} = \sum_{\pi\lambda} a^{\pi\lambda} \frac{d\sigma}{d\Omega}(\theta, E_x)^{\pi\lambda}_{theo}, \tag{5.3}$$

where $a^{\pi\lambda}$ were fit parameters. The fits were performed using the following criteria and boundary conditions:

- For each data set measured at the spectrometer angle θ_{GR}=(0°, 2.5°, 4.5°), five data points per angle and energy bin were generated by applying different gates for the vertical and horizontal angles respectively, so that in total 15 data points between 0.5° and 5° were available for the MDA
- In total six E1 transitions (three in the PDR region and three in the GDR region) with the largest B(E1) values in the QPM calculations were used, since the corresponding angular distributions show sensitivity on the Coulomb-nuclear interference
- Two M1 transitions with the largest B(M1) values in the QPM calculations were used
- The E3 transition was used as a substitute for possible higher multipole contributions, since they all show a similar shape in the studied forward-angle region
- The parametrisation determined in Section 5.4 was used for the QFS background
- All fit parameters $a^{\pi\lambda}$ had to be positive

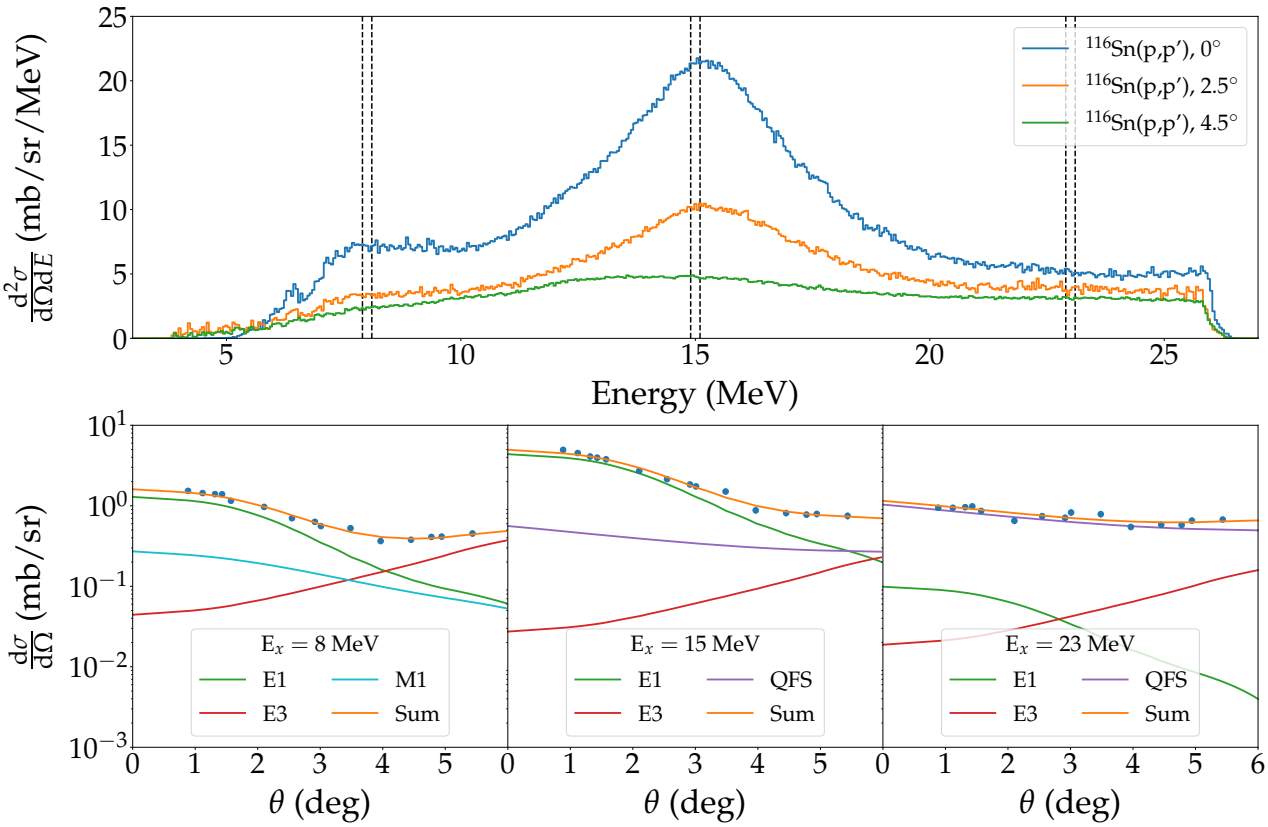

Figure 5.8: Typical result of the MDA for three different energy bins shown exemplary for ^{116}Sn. The energy bins have a width of 200 keV and are indicated by dashed lines.

The least-squares fitting procedure was carried out including all possible combinations of the theoretical angular distributions satisfying the above criteria. For each combination the chi-squared χ^2 and the reduced chi-squared $\chi^2_{red} = \chi^2/(p-n)$ values were calculated with p the number of experimental data points and n the number of fit parameters. Using $\omega = 1/\chi^2_{red}$ as a weighting parameter, weighted mean cross sections for each contribution were finally determined

$$\left\langle \frac{\mathrm{d}\sigma}{\mathrm{d}\Omega}(\theta, E_x)^{\pi\lambda} \right\rangle = \frac{\sum_i \omega_i \frac{\mathrm{d}\sigma}{\mathrm{d}\Omega}(\theta, E_x)_i^{\pi\lambda}}{\sum_i \omega_i}. \tag{5.4}$$

The corresponding uncertainty was obtained from the weighted variance

$$\sigma^2 = \frac{\sum_i \omega_i \left(\frac{\mathrm{d}\sigma}{\mathrm{d}\Omega}(\theta, E_x)_i^{\pi\lambda} - \left\langle \frac{\mathrm{d}\sigma}{\mathrm{d}\Omega}(\theta, E_x)^{\pi\lambda} \right\rangle \right)^2}{\sum_i \omega_i}. \tag{5.5}$$

In Fig. 5.8 a typical result of the MDA is shown for three different energy bins. In the low-energy region mainly contributions from E1 and M1 are found, but also minor contributions from higher multipole transitions. The GDR region is dominated by E1 transitions as expected

with minor contributions from higher multipoles and QFS background. At even higher energies, beyond the GDR region, the main contribution comes from the QFS background, though some E1 transitions stemming from the GDR tail can still be observed. Minor contributions from higher multipoles are also found. The results of the MDA for all isotopes are summarised in Fig. 5.9. The E1 contribution is similar in all isotopes. The M1 contribution deviates more strongly for the different isotopes. Due to the similar shape of the M1 curve and the curve of the QFS background, it is more difficult to distinguish these two contributions above the neutron threshold.

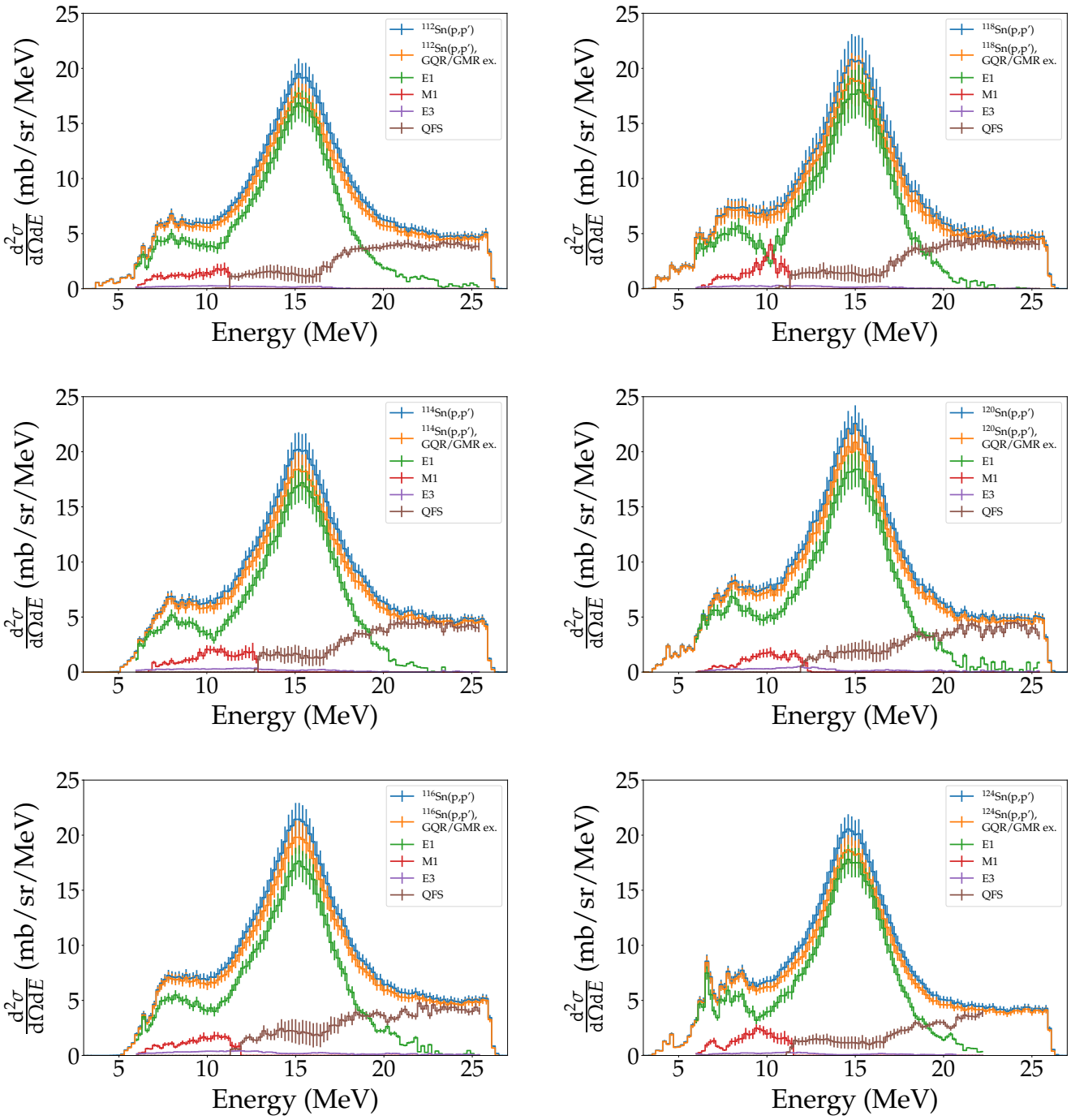

Figure 5.9: Results of the multipole decomposition analysis for the studied tin isotopes. The error bars include statistical, systematical and MDA uncertainties.

6 Results and discussion

6.1 Comparison to photoabsorption experiments

Data on the electric dipole strength for some of the tin isotopes discussed in this work are available from photoabsorption experiments. In order to compare to these data, it is necessary to convert the double differential cross sections from proton scattering to photoabsorption cross sections. For this purpose the equivalent photon method can be used which was introduced in Section 2.2. Considering only E1 contributions obtained from the MDA, Eqn. (2.30) reduces to

$$\frac{\mathrm{d}^2\sigma_{E1}}{\mathrm{d}\Omega \mathrm{d}E}(E) = \frac{1}{E}\frac{\mathrm{d}N_{E1}}{\mathrm{d}\Omega}(E,\theta)\sigma_{abs}^{E1}(E). \tag{6.1}$$

In this equation the differential virtual photon number $\frac{\mathrm{d}N_{E1}}{\mathrm{d}\Omega}(E,\theta)$ depends on the energy and the scattering angle. The experimental data on the other hand are given for an average scattering angle. To account for this, one needs to average the differential virtual photon number over the experimental solid angle. Another point to be considered is the maximum scattering angle at which the strong interaction between projectile and target nucleus starts to play a role. This can be calculated from relativistic Rutherford scattering using equation [115]

$$\theta_{lab}^{max} = \frac{Z_1 Z_2 e^2}{b\mu\beta^2\gamma}, \tag{6.2}$$

where Z_1 is the projectile charge, Z_2 the charge of the target nucleus, e the elementary charge, μ the reduced mass, β the velocity in units of speed of light, γ the Lorentz factor and b the impact parameter. The impact parameter is taken as the sum of the projectile and target nucleus radii $b = r_p + r_0 A^{1/3}$, where r_p is the proton root mean square charge radius, $r_0 = 1.25\,\mathrm{fm}$ and A is the mass number of the tin isotope. For the measured tin isotopes the maximum scattering angle was determined to $\theta_{lab}^{max} = 2.25^\circ - 2.32^\circ$ ($\theta_{cm}^{max} = 2.28^\circ - 2.35^\circ$) depending on the isotope. With the considerations discussed above, the average differential virtual photon number can be calculated as

$$\left\langle \frac{\mathrm{d}N_{E1}}{\mathrm{d}\Omega}(E,\theta) \right\rangle = \frac{\int \frac{\mathrm{d}N_{E1}}{\mathrm{d}\Omega}(E,\theta)\mathrm{d}\Omega}{\int \mathrm{d}\Omega}, \tag{6.3}$$

where the integration is performed up to the maximum angle θ_{cm}^{max}.

The photoabsorption cross sections obtained using Eqs. (6.1) and (6.3) are shown in Fig. 6.1 in comparison to data from (γ,xn) experiments. In the GDR region a fair agreement is found

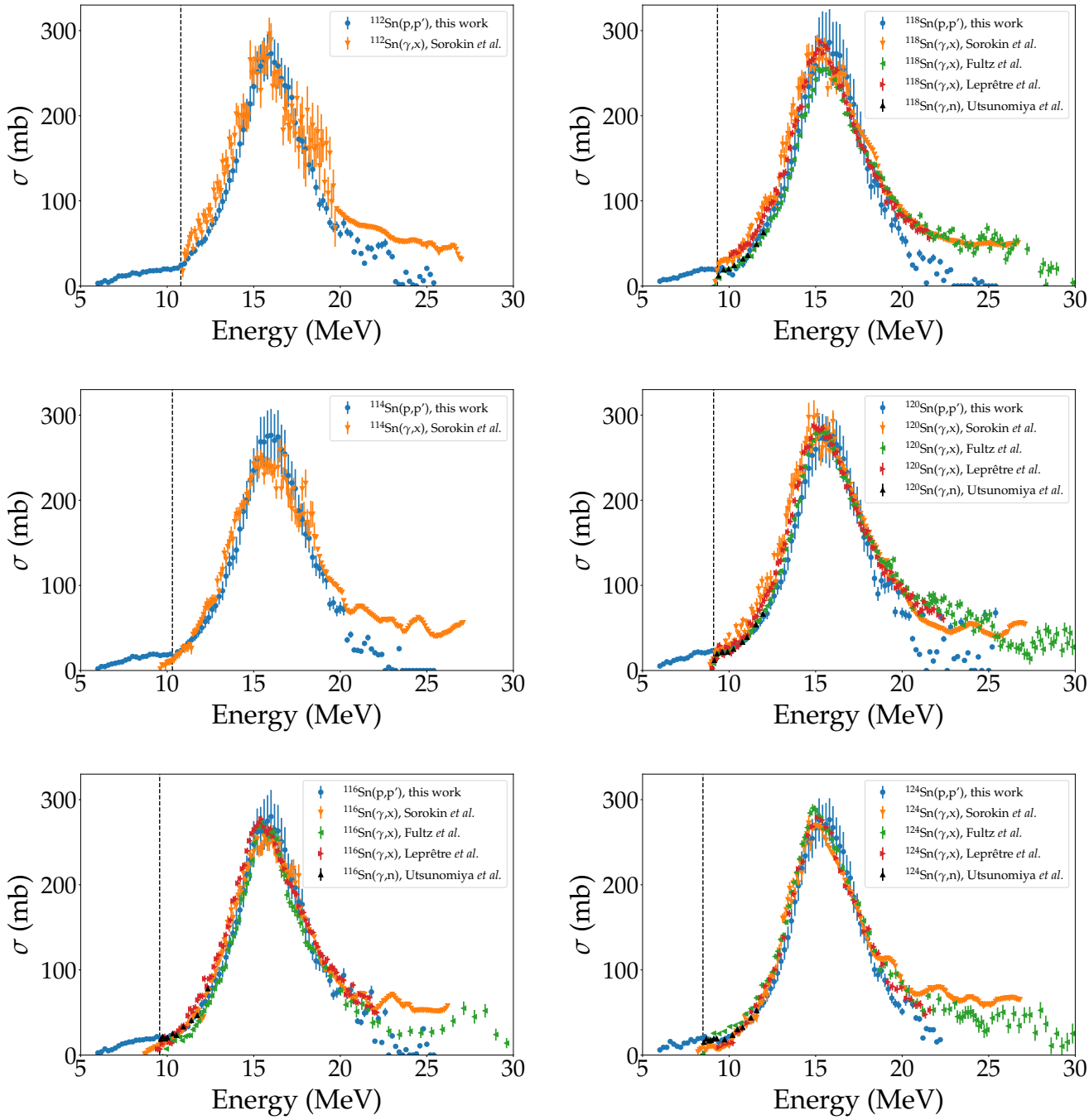

Figure 6.1: Photoabsorption cross sections obtained in this work in comparison to data from photoabsorption experiments carried out by Sorokin *et al.* [116, 117], Fultz *et al.* [118], Leprêtre *et al.* [119] and Utsunomiya *et al.* [120, 121]. The neutron threshold is indicated by dashed lines.

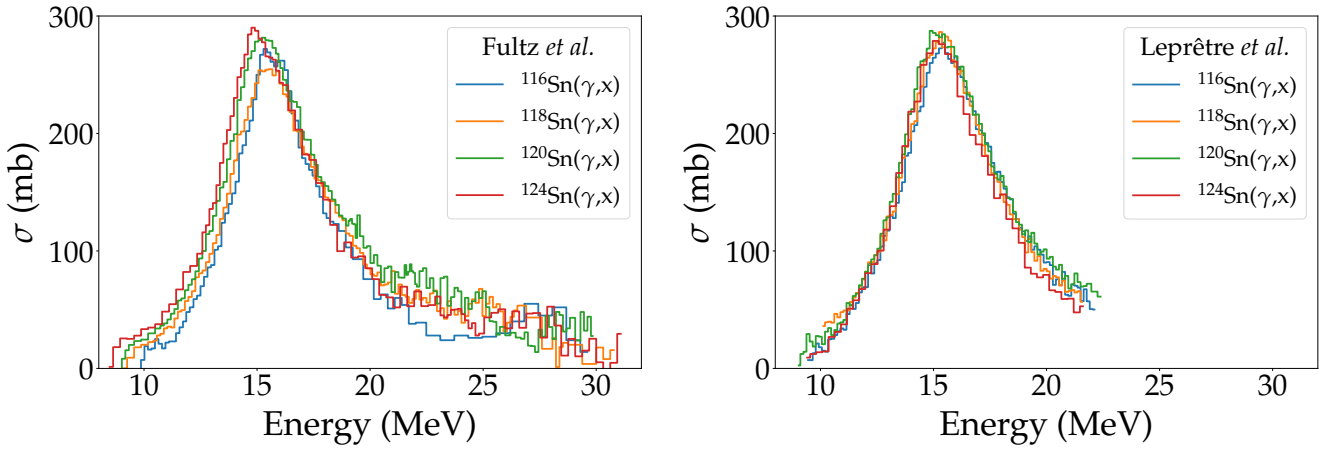

Figure 6.2: Photoabsorption cross sections measured at Livermore [118] (left) and Saclay [119] (right).

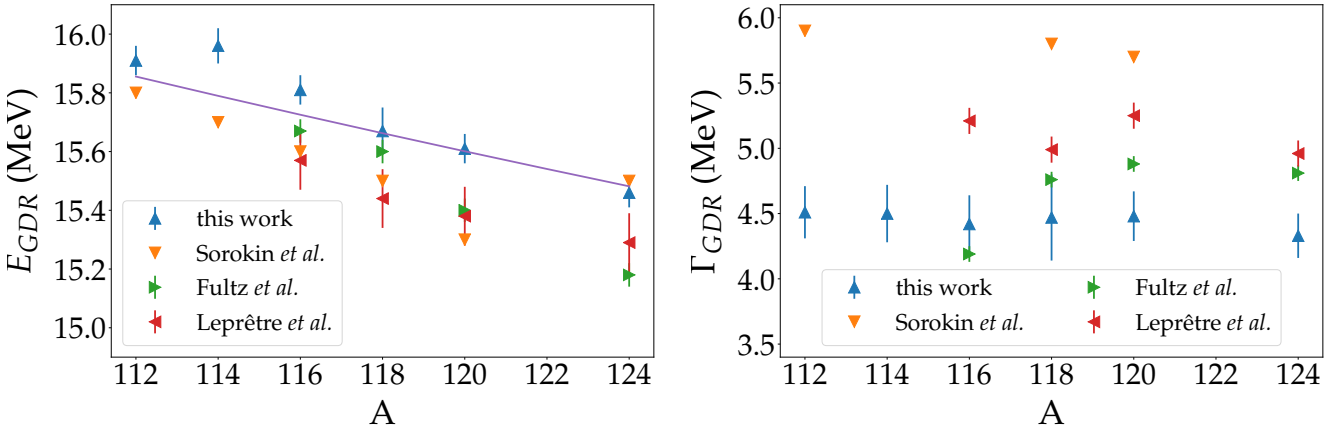

Figure 6.3: Centroid energy E_{GDR} and width Γ_{GDR} of the GDR in tin isotopes determined from different experiments. The purple line shows the calculation using Eqn. (6.4).

in most cases. Around the neutron threshold, however, larger deviations can be observed. The most recent photoabsorption experiments were performed by Utsunomiya *et al.* [120, 121] in 2009 and 2011. Data from these experiments are in good agreement for all isotopes with results obtained in this work. The data sets from photoabsorption experiments measured at Livermore [118] and Saclay [119] seem to have internal inconsistencies. On the left side of Fig. 6.2 the Livermore data are shown. It can be seen that around 23 MeV large deviations between the individual data sets occur. On the right side of Fig. 6.2 the Saclay data are shown. Here, the expected shift of the centroid energy of the GDR appears to be very small on the left tail of the GDR.

Parameters from a Lorentzian fit to the shown data are presented in Fig. 6.3 and summarised in Table 6.1. The peak cross sections σ_{GDR} agree very well within the uncertainties for all data sets. The expected decrease in the centroid energy E_{GDR} with increasing mass number A is found in all experiments, though neither the absolute values nor the slope agree between the

Table 6.1: Lorentz parameters for the GDR in tin isotopes determined from different experiments. The original data in Refs. [116, 117] were not accessible. However, data from these references were used in Table 5 of Ref. [124]. These data are shown here. Neither uncertainties, nor the fitting range were provided for these data. For all other data the fitting range was the same (13-18 MeV).

	^{112}Sn	^{114}Sn	^{116}Sn	^{118}Sn	^{120}Sn	^{124}Sn
σ_{GDR} (mb)						
this work	272 ± 16	280 ± 16	279 ± 16	290 ± 16	285 ± 16	286 ± 15
Ref. [116,117,124]	268	265	260	272	297	270
Ref. [118]	–	–	266 ± 7	255 ± 7	280 ± 8	283 ± 8
Ref. [119]	–	–	270 ± 5	278 ± 5	284 ± 5	275 ± 5
E_{GDR} (MeV)						
this work	15.91 ± 0.05	15.96 ± 0.06	15.81 ± 0.05	15.67 ± 0.08	15.61 ± 0.05	15.46 ± 0.05
Ref. [116,117,124]	15.8	15.7	15.6	15.5	15.3	15.5
Ref. [118]	–	–	15.67 ± 0.04	15.60 ± 0.04	15.40 ± 0.04	15.18 ± 0.04
Ref. [119]	–	–	15.57 ± 0.1	15.44 ± 0.1	15.38 ± 0.1	15.29 ± 0.1
Γ_{GDR} (MeV)						
this work	4.51 ± 0.20	4.50 ± 0.22	4.42 ± 0.22	4.47 ± 0.33	4.48 ± 0.19	4.33 ± 0.17
Ref. [116,117,124]	5.9	–	–	5.8	5.7	–
Ref. [118]	–	–	4.19 ± 0.06	4.76 ± 0.06	4.88 ± 0.06	4.81 ± 0.06
Ref. [119]	–	–	5.21 ± 0.1	4.99 ± 0.1	5.25 ± 0.1	4.96 ± 0.1

different experiments. The centroid energies determined in this work are found to be generally higher, yet they yield the best agreement for the centroid energy comparing with the well-known phenomenological formula [5, 122, 123]

$$E_{GDR} = 31.2A^{-1/3} + 20.6A^{-1/6}. \tag{6.4}$$

The width Γ_{GDR} is found to be quite inconsistent between the different experiments. In proton scattering it is constant within the uncertainties. Likewise, data from Fultz *et al.* [118] show a rather constant width, except for ^{116}Sn. The data from Leprêtre *et al.* [119] show a fluctuating behaviour. The width determined by Sorokin *et al.* [116, 117, 124] shows a slightly decreasing trend with increasing mass number. The absolute values determined in this work are generally lower than those found in photoabsorption experiments. However, almost all determined widths from different experiments are in disagreement with each other. Differences may be related to problems of (γ,n), (γ,2n) separation in both, Saclay [119] and Livermore [118] experiments as discussed in Ref. [124].

6.2 E1 strength distribution below the neutron threshold

Below the neutron threshold, comparison can be made with data from nuclear resonance fluorescence (NRF) experiments. For this purpose the photoabsorption cross sections determined

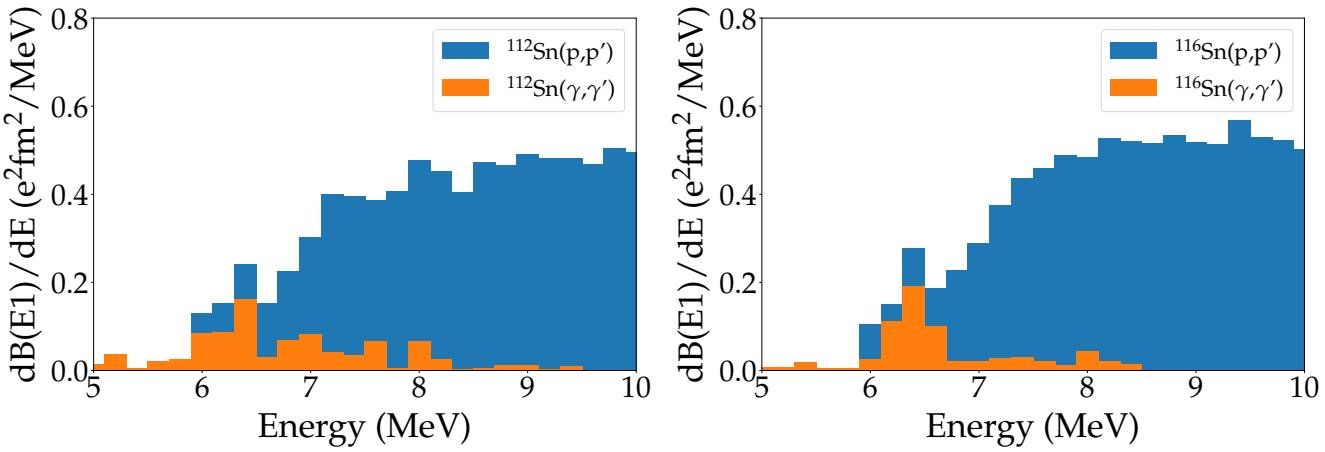

Figure 6.4: B(E1) strength distributions for ^{112}Sn and ^{116}Sn obtained in this work in comparison to results from NRF experiments [126, 127].

in the last section were converted to the corresponding B(E1) strengths using the following relation [125]

$$\frac{\mathrm{d}B(E1)}{\mathrm{d}E} = \frac{9\hbar c}{16\pi^3}\frac{\sigma_{abs}^{E1}}{E}. \tag{6.5}$$

Strength distributions from NRF experiments are available for ^{112}Sn, ^{116}Sn, ^{120}Sn and ^{124}Sn [126, 127]. For ^{120}Sn a comparison between proton scattering data and NRF data was already carried out in Ref. [73]. It was found that in proton scattering considerably more E1 strength is observed, in particular at energies close to the neutron threshold. In Fig. 6.4 B(E1) strength distributions from proton scattering are compared to results from NRF experiments for ^{112}Sn and ^{116}Sn. As in ^{120}Sn, an approximate agreement is found in the region up to 6.5 MeV, in particular if inelastic branchings (statistical decay) are included for the NRF data [73]. Above 6.5 MeV substantially more strength is found for both isotopes measured in proton scattering. There are two potential explanations for this findings. Due to the high level density in the tin isotopes much of the strength cannot be resolved in NRF experiments [128, 129] close to the neutron threshold, which leads to lower B(E1) values. Additionally, excitation strengths are usually determined under the assumption that decays to excited states are negligible. This assumption however is not always justified [130, 131] and can lead erroneously to even lower B(E1) values.

Fig. 6.5 shows results on the E1 strength from four different experiments studying the dipole response in ^{124}Sn. While (p,p′) and (γ,γ′) reactions induce predominantly isovector transitions, (^{17}O,^{17}O′γ) and (α,α′γ) experiments probe the isoscalar part. As in the cases for ^{112}Sn, ^{116}Sn and ^{120}Sn again an increasing amount of strength is found towards higher excitation energies in the proton scattering data of ^{124}Sn in contrast to the NRF data. The structure around 6.5 MeV observed in lighter tin isotopes is even more prominent in ^{124}Sn clearly seen in both

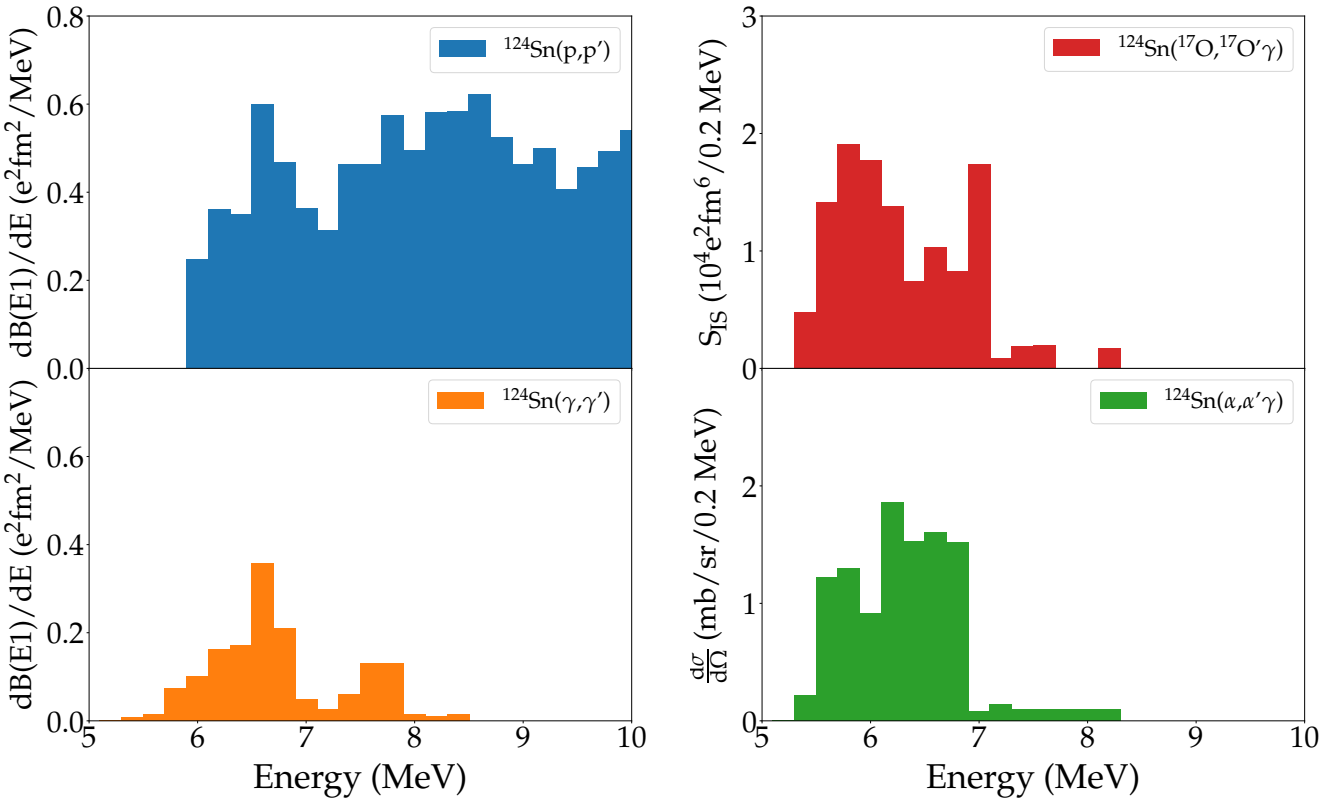

Figure 6.5: B(E1) strength distributions for ^{124}Sn obtained in this work in comparison to NRF results [127] (left) and isoscalar strength distributions obtained in an (^{17}O,^{17}O'γ) experiment [19] and differential cross section from an (α,α'γ) experiment [18] on ^{124}Sn (right).

experiments. A completely different picture yield results from the (^{17}O,^{17}O'γ) and (α,α'γ) experiments studying the isoscalar E1 strength shown on the right side of Fig. 6.5. In both experiments comparable E1 response is found in the energy region of $5.4 - 7$ MeV. However, above 7 MeV E1 transitions seem to be suppressed. From the macroscopic picture describing the PDR as a neutron-skin oscillation against an isospin saturated core, one expects mixed isoscalar and isovector excitation as seen in all four experiments below 7 MeV. Absence of isoscalar strength at higher energies indicates a dominant structure of the strength as low-energy tail of the isovector giant dipole resonance.

6.3 Electric dipole polarisability

The electric dipole polarisability can be calculated directly from the photoabsorption cross sections determined in Section 6.1 via the relation [132]

$$\alpha_D = \frac{\hbar c}{2\pi^2} \int \frac{\sigma_{abs}^{E1}}{E^2} \mathrm{d}E \tag{6.6}$$

The integration needs to be performed in principle from zero to infinity. In Ref. [89] the dipole polarisability for ^{120}Sn was extracted. Below 5 MeV data from NRF experiments were used [126], albeit the contribution to the total dipole polarisability was below 0.1 %. Between 5 and 10 MeV proton scattering data were used. Above the neutron threshold proton scattering data were averaged with data from photoabsorption experiments [118–121]. For energies above 22 MeV data from Ref. [118] were used up to 30 MeV and data from Ref. [133] to calculate the dipole polarisability up to an energy of 135 MeV.

In this work photoabsorption cross sections were determined from inelastic proton scattering in an energy region of $6 - 20$ MeV. Below 6 MeV data are available for ^{112,116,120,124}Sn from NRF experiments [126,127], but were neglected due to small contributions (< 0.5 %) . Contrary to the procedure in Ref. [89], data above the neutron threshold were not averaged. Because of the substantial deviations between the individual data sets from photoabsorption experiments as pointed out in Section 6.1 (cf. Fig. 6.2), these data sets were deemed to be unreliable, in particular when studying the isotope dependence. Hence, only photoabsorption cross sections from proton scattering were used in the energy region between 6 and 20 MeV. As no reliable data were available above 20 MeV, a different approach was chosen to calculate the dipole polarisability in this region. A QRPA [134] calculation was carried out based on the QPM (cf. Section 2.3) to reproduce the GDR and the high-energy tail of the GDR above 20 MeV. These calculations were shown to provide a very good description of GDR properties in heavy nuclei [7,70,72,135]. The obtained cross sections from QRPA were convoluted with experimental widths of the GDR as determined in Section. 6.1 and were used to calculate the dipole polarisability in the energy region between 20 and 30 MeV. The contribution in this energy region accounts for about 8 % of the total dipole polarisability. The energy region above 30 MeV was not taken into account, because of the role of the quasideuteron effect [136], as suggested in Ref. [32].

The running sums of the dipole polarisability for the tin isotopes discussed in this work are presented in Fig. 6.6. Obviously the main contribution comes from the GDR as can be seen in the figure. The contribution below the neutron threshold amounts between 8 % and 13 %, depending on the isotope.

In Ref. [32] Roca-Maza *et al.* compared the available data on the electric dipole polarisability of ^{68}Ni [137], ^{120}Sn [89] and ^{208}Pb [135] to model calculations based on nuclear density functional theory [138] to deduce information on the symmetry energy parameters. It was found that only a handful of the model calculations could reproduce the experimental dipole polarisability simultaneously for all three isotopes in question. The dipole polarisability for ^{120}Sn was taken from Ref. [89], but corrected for the quasideuteron effect, which reduced the value from $\alpha_D = 8.93 \pm 0.36\,\mathrm{fm}^3$ to $\alpha_D = 8.59 \pm 0.37\,\mathrm{fm}^3$. In this work the dipole polarisability for ^{120}Sn was determined to be even lower ($\alpha_D = 7.95 \pm 0.59\,\mathrm{fm}^3$). The reason for the smaller value comes from the fact that the Livermore data between 20 and 30 MeV is not included here due to

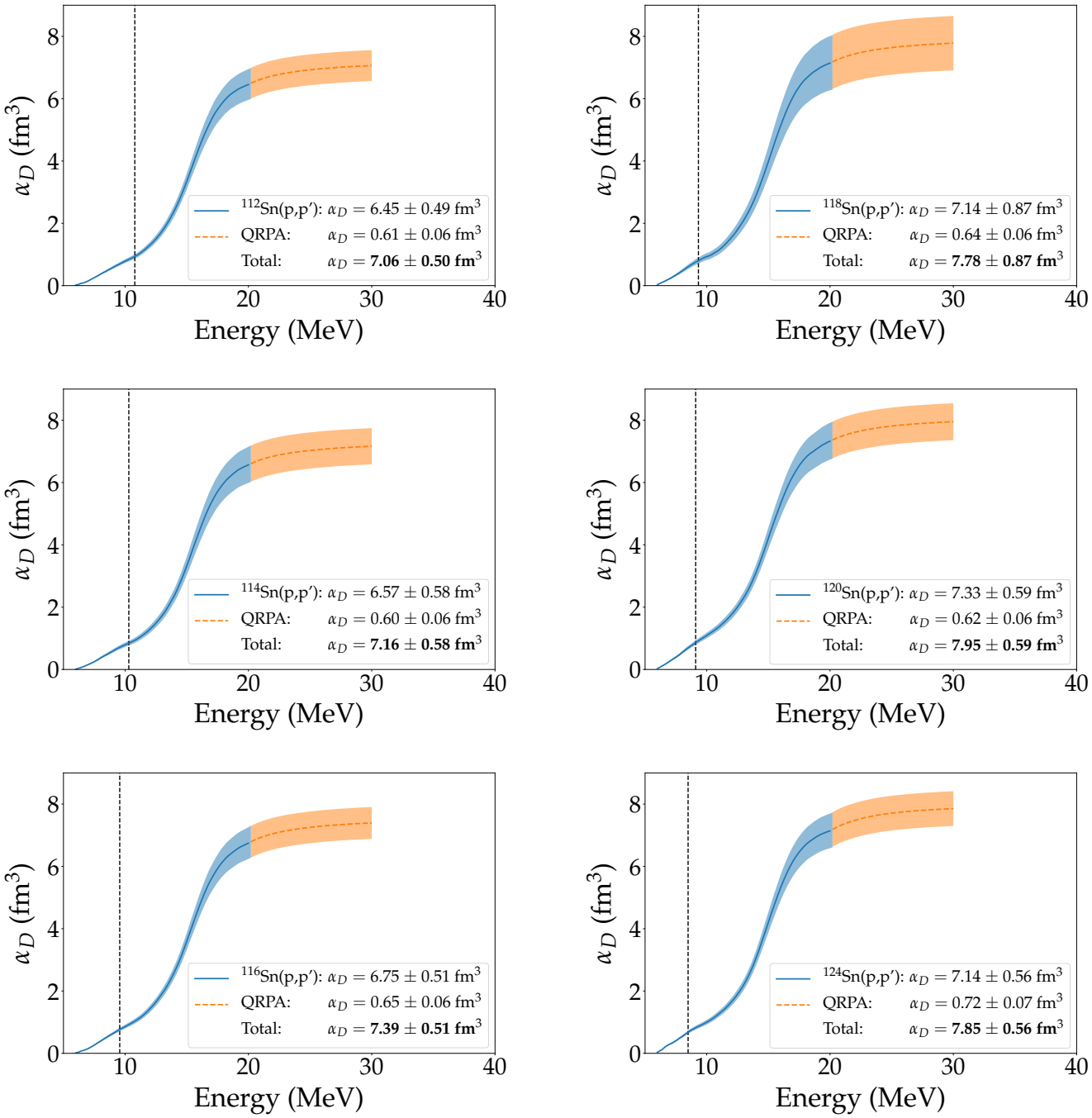

Figure 6.6: Running sums of the electric dipole polarisability for stable tin isotopes from the present data. The neutron threshold is indicated by dashed lines.

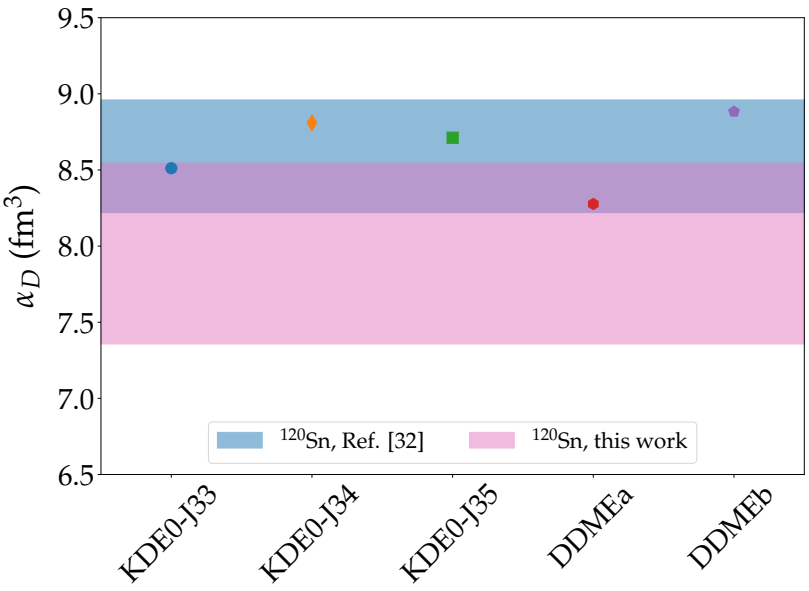

Figure 6.7: Model calculations [140–142] for the dipole polarisability of ^{120}Sn compared to the experimental value used in Ref. [32] and the one obtained in this work.

the inconsistency of the data in this region (cf. Fig. 6.2). In Fig. 6.7 the corrected dipole polarisability for ^{120}Sn used in Ref. [32] is shown together with the new value in comparison to model calculations which could reproduce the experimental dipole polarisability simultaneously for ^{68}Ni, ^{120}Sn and ^{208}Pb. Only two out of five model calculations lie within the error bars of the dipole polarisability obtained in this work. Error bars for the shown model calculations were not provided, but can be in principle estimated as described in Ref. [139].

On the left side of Fig. 6.8 the isotope dependence of the dipole polarisability is shown in comparison with an $A^{5/3}$ trend predicted by Migdal [143] in a hydrodynamical model of interpenetrating proton and neutron fluids. A free fit of the A dependence yields a slightly lower power, but compatible within the uncertainties. In Table 6.2 the dipole polarisabilities obtained in this work are summarised together with results from model calculations [144] based on the KDE0 energy density functional (EDF) [140, 141] which was one of the EDFs able to reproduce the dipole polarisability of ^{68}Ni, ^{120}Sn and ^{208}Pb simultaneously including the new value for the dipole polarisability in ^{120}Sn. On the right side of Fig. 6.8, these model calculations are compared to the experimental polarisabilities. The model calculations are shown for a reasonable range of the symmetry energy parameters $J = 30 - 34\,\mathrm{MeV}$ and $L = 20 - 60\,\mathrm{MeV}$, suggested by a summary of analyses from different sources (cf. Tab. 2 in Ref. [29]), where the parameter L covers a rather low range. The parametrisation KDE0-J30 is able to reproduce all experimental polarisabilities, while KDE0-J32 and KDE0-J33 can reproduce all polarisabilities except for ^{124}Sn. KDE0-J34 is only within the error bars of ^{118}Sn. These systematic comparison favours rather low values of the symmetry energy parameters J and L. An open question is still the case of ^{124}Sn. The polarisability for this isotope do not follow the trend seen in the lighter isotopes,

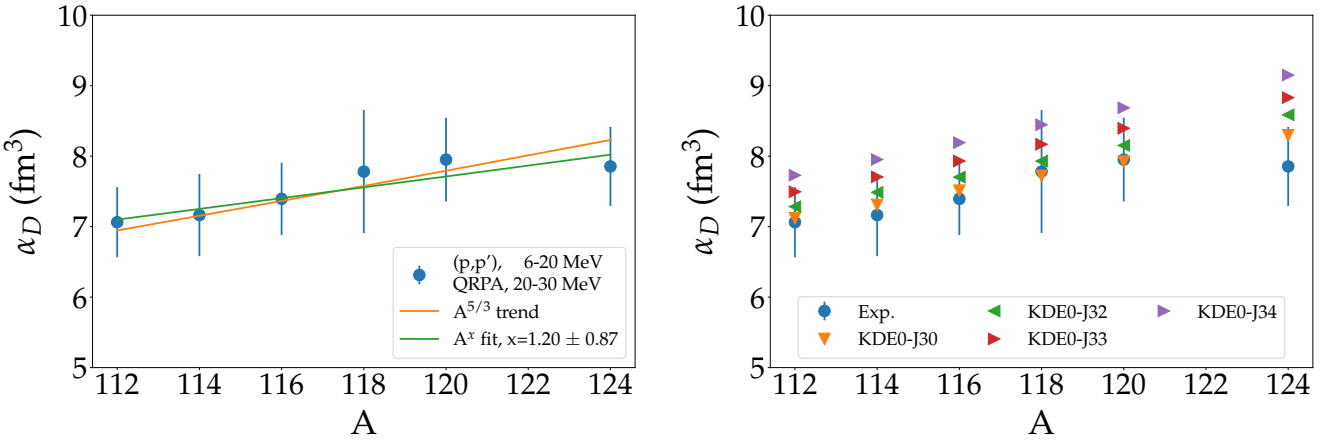

Figure 6.8: Electric dipole polarisability for stable tin isotopes including the $A^{5/3}$ trend and a fit to the data (left). Model calculations in comparison to experimental data (right).

Table 6.2: Electric dipole polarisability obtained from experiment and model calculations. Details on the used EDFs can be found in [140, 141]. All polarisabilities are given in fm^3.

	^{112}Sn	^{114}Sn	^{116}Sn	^{118}Sn	^{120}Sn	^{124}Sn
this work	7.06 ± 0.50	7.16 ± 0.58	7.39 ± 0.51	7.78 ± 0.87	7.95 ± 0.59	7.85 ± 0.56
KDE0-J30	7.12	7.31	7.51	7.72	7.92	8.30
KDE0-J32	7.28	7.49	7.70	7.93	8.15	8.59
KDE0-J33	7.49	7.71	7.93	8.17	8.40	8.83
KDE0-J34	7.73	7.95	8.19	8.45	8.69	9.15

where the polarisability increases with the neutron number. This trend is reproduced rather well by the models shown in Fig. 6.8, but no decrease in the polarisability of ^{124}Sn is predicted. In general, constraints need systematic comparison to EDFs, which is work in progress.

6.4 M1 strength distribution

The multipole decomposition analysis yielded apart of the dominant E1 contribution also considerable M1 contributions to the cross sections in the PDR region. It is possible to determine the spin M1 strength $B(M1_{\sigma\tau})$ and the corresponding electromagnetic strength $B(M1_{EM})$ using the so-called unit cross section method based on isospin symmetry of the isovector spin M1 mode and the analogue Gamow-Teller (GT) mode excited in charge exchange reactions. In the following only the essential procedure will be introduced. A more detailed description of the method can be found in Refs. [145, 146] and references therein.

The spin M1 strength is related to the isovector part of the differential cross section as follows

$$\frac{\mathrm{d}\sigma}{\mathrm{d}\Omega}(0^\circ)^{IV}_{exp} = \hat{\sigma}_{M1} F(q, E_x) B(M1_{\sigma\tau}). \tag{6.7}$$

In the inelastic proton scattering experiment discussed in this work the spin M1 excitation was predominantly of isovector nature at 0°, so that the differential cross section of the M1 contribution obtained from the MDA can be used here directly. Assuming isospin symmetry the unit cross section for the spin M1 transition in inelastic proton scattering is the same as in the case of Gamow-Teller transitions in charge exchange experiments $\hat{\sigma}_{M1} \simeq \hat{\sigma}_{GT}$. The systematics of the unit cross section $\hat{\sigma}_{GT}$ was investigated in Ref. [147], where a mass dependent formula for the unit cross section was derived

$$\hat{\sigma}_{GT} = 3.4(2)\exp[-0.40(5)(A^{1/3} - 90^{1/3})]\,\mathrm{mb/sr}, \tag{6.8}$$

valid for a projectile energy of $E_p \cong 300\,\mathrm{MeV}$. Using this formula the unit cross section can be calculated for all tin isotopes discussed in this work. The last variable in Eqn. (6.7) is the kinematical factor $F(q, E_x)$, which can be obtained from DWBA calculations as follows

$$F(q, E_x) = \frac{\frac{\mathrm{d}\sigma}{\mathrm{d}\Omega}(0, E_x)_{DWBA}}{\frac{\mathrm{d}\sigma}{\mathrm{d}\Omega}(0, 0)_{DWBA}}, \tag{6.9}$$

where E_x is the excitation energy of the spin M1 mode. For tin isotopes the kinematical factor is $F(0, E_x \approx 8\,\mathrm{MeV}) \approx 0.92$. Finally, the corresponding electromagnetic strength can be calculated neglecting isoscalar and orbital parts in the electromagnetic M1 operator

$$B(M1_{EM}) = \frac{3}{4\pi}(g_s^{IV})^2 B(M1_{\sigma\tau})\,\mu_N^2, \tag{6.10}$$

where $g_s^{IV} = \frac{1}{2}(g_s^{\pi} - g_s^{\nu})$ is the isovector gyromagnetic factor with the $g_s^{\pi} = 5.586$ and $g_s^{\nu} = -3.826$ spin g-factors [148].

In Fig. 6.9 the extracted differential electromagnetic M1 strength is shown for stable tin isotopes. As already mentioned in Section 5.5 the shape of the theoretical M1 and QFS curves are quite similar, making it difficult to distinguish between these two contributions. Therefore, particularly in the region between 11 and 13 MeV the decomposition of these two contributions in the MDA is highly uncertain. In Fig. 6.10 a direct comparison of the electromagnetic M1 strengths as well as their running sums are shown. The shape of the M1 strength is quite similar in all isotopes except for ^{118}Sn where a prominent peak is observed around 10 MeV. The running sum shows that ^{118}Sn and ^{124}Sn are slightly higher compared to other isotopes. No systematic behaviour in terms of mass number is observed. The energy range, centroid energy and total M1 strengths are summarised in Tab. 6.3.

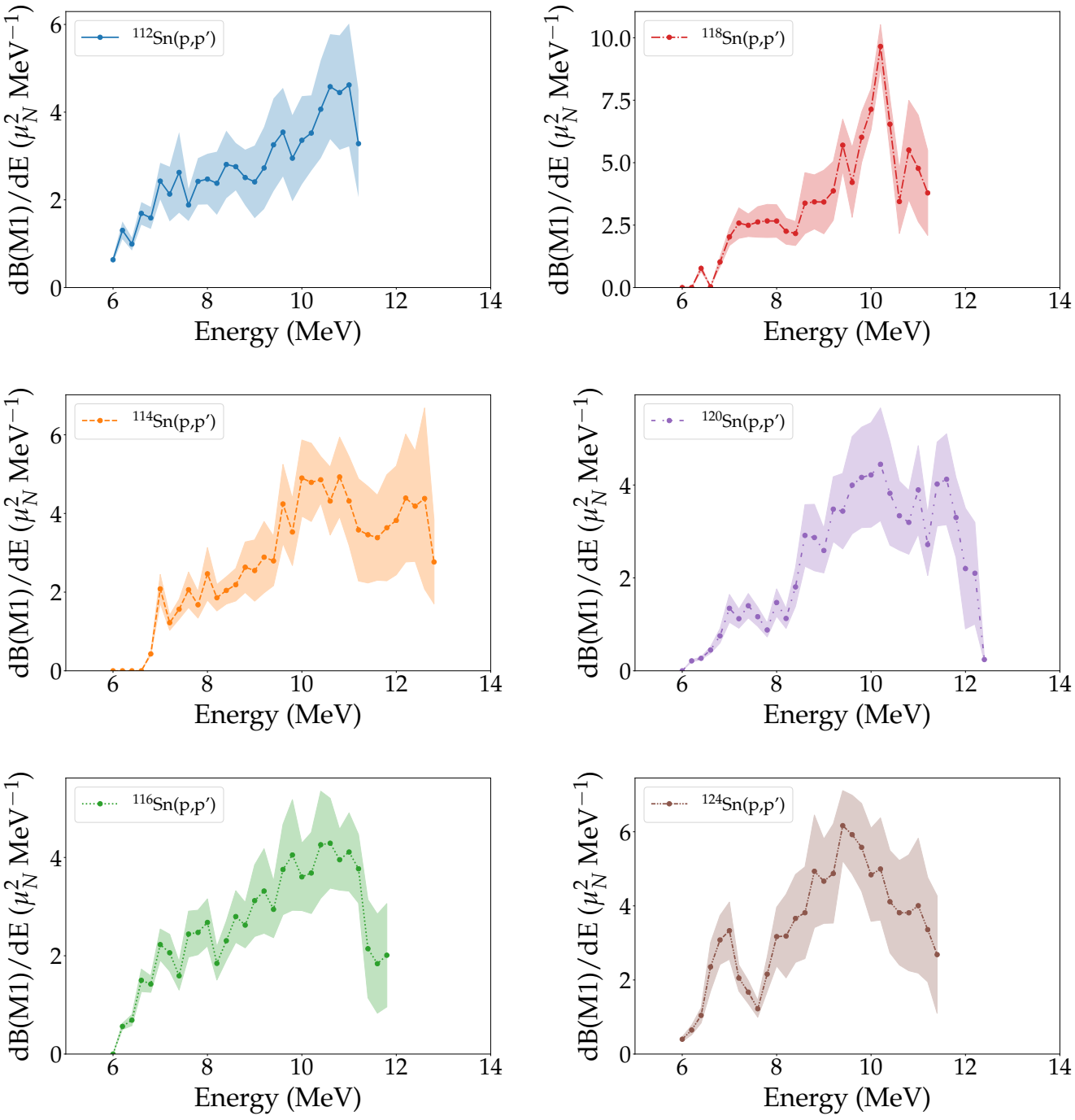

Figure 6.9: Extracted differential electromagnetic M1 strength for stable tin isotopes from the present data.

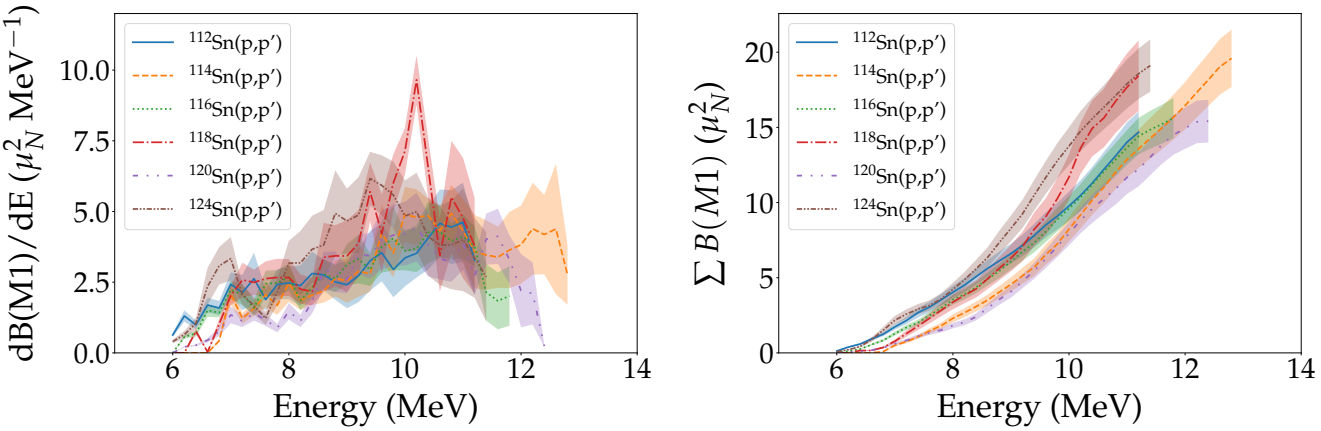

Figure 6.10: Comparison between the M1 strength distributions (left) and their running sums (right) for stable tin isotopes derived from the present data.

Table 6.3: Total M1 strength in stable tin isotopes.

	Energy range E_x (MeV)	Centroid energy E_c (MeV)	Total strength $\sum B(M1_{EM})$ (μ_N^2)
^{112}Sn	$6-11.2$	9.1 ± 0.1	14.68 ± 1.37
^{114}Sn	$6-12.8$	10.3 ± 0.1	19.59 ± 1.91
^{116}Sn	$6-11.8$	9.4 ± 0.1	15.62 ± 1.34
^{118}Sn	$6-11.2$	9.4 ± 0.1	18.44 ± 2.35
^{120}Sn	$6-12.4$	9.9 ± 0.1	15.41 ± 1.42
^{124}Sn	$6-11.4$	9.2 ± 0.1	19.11 ± 1.74

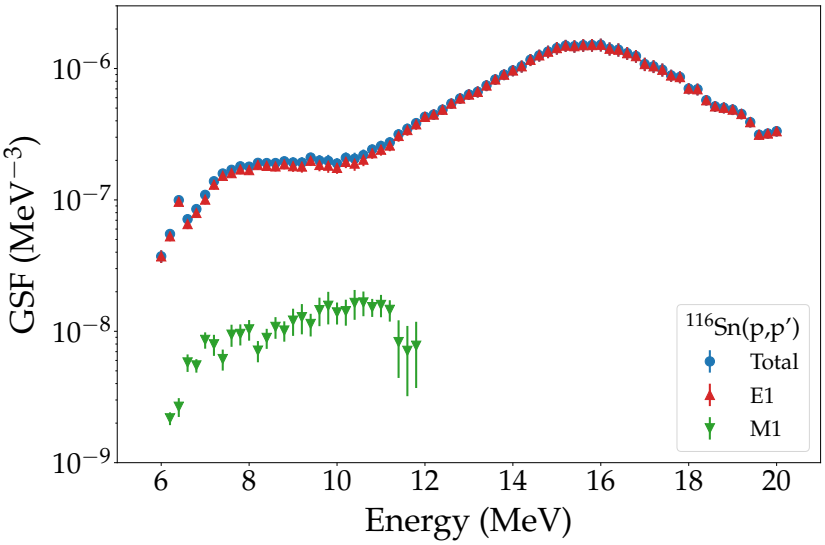

Figure 6.11: E1 and M1 contributions to the total gamma strength function of ^{116}Sn for the present data.

6.5 Gamma strength function

The gamma strength function (GSF) is related to the photoabsorption cross section via [149]

$$f^{X\lambda}(E,J) = \frac{2J_0+1}{(\pi\hbar c)^2(2J+1)} \frac{\langle \sigma_{abs}^{X\lambda} \rangle}{E^{2\lambda-1}}, \tag{6.11}$$

where $\langle \sigma_{abs}^{X\lambda} \rangle$ is the average photoabsorption cross section of an electric or magnetic transition $X \in \{E, M\}$ with multipolarity λ and E the gamma energy, which is equal to the excitation energy for absorption from the ground state. J and J_0 are the spins of the excited and ground state, respectively. Although all multipolarities are included in this equation, the E1 contribution is by far the most dominant one, though M1 can be relevant at lower energies. All higher order contributions, i.e. $\lambda > 1$, are negligible.

In Fig. 6.11 the total gamma strength function and its E1 and M1 contributions, derived from the present data, are shown for ^{116}Sn as an example. The results are similar for the other isotopes. One can see immediately the dominance of the E1 contribution, even in the region of the spin M1 resonance. The contribution from M1 is at least one order of magnitude smaller. Figure 6.12 shows the total gamma strength function obtained in this work in comparison to results from different experiments. The results are in a reasonable agreement in the region of the maximum of the GDR. Towards the neutron threshold, however, strong deviations can be found between the individual data sets as already pointed out in Section 6.1. Results from NRF experiments are generally too low as already discussed in Section 6.2. In Fig. 6.13 the low-energy part of the GSF is shown for ^{116}Sn and ^{118}Sn. For these isotopes data from (^{3}He,^{3}He'γ) and (^{3}He,$\alpha\gamma$) decay experiments are available measured at the Oslo

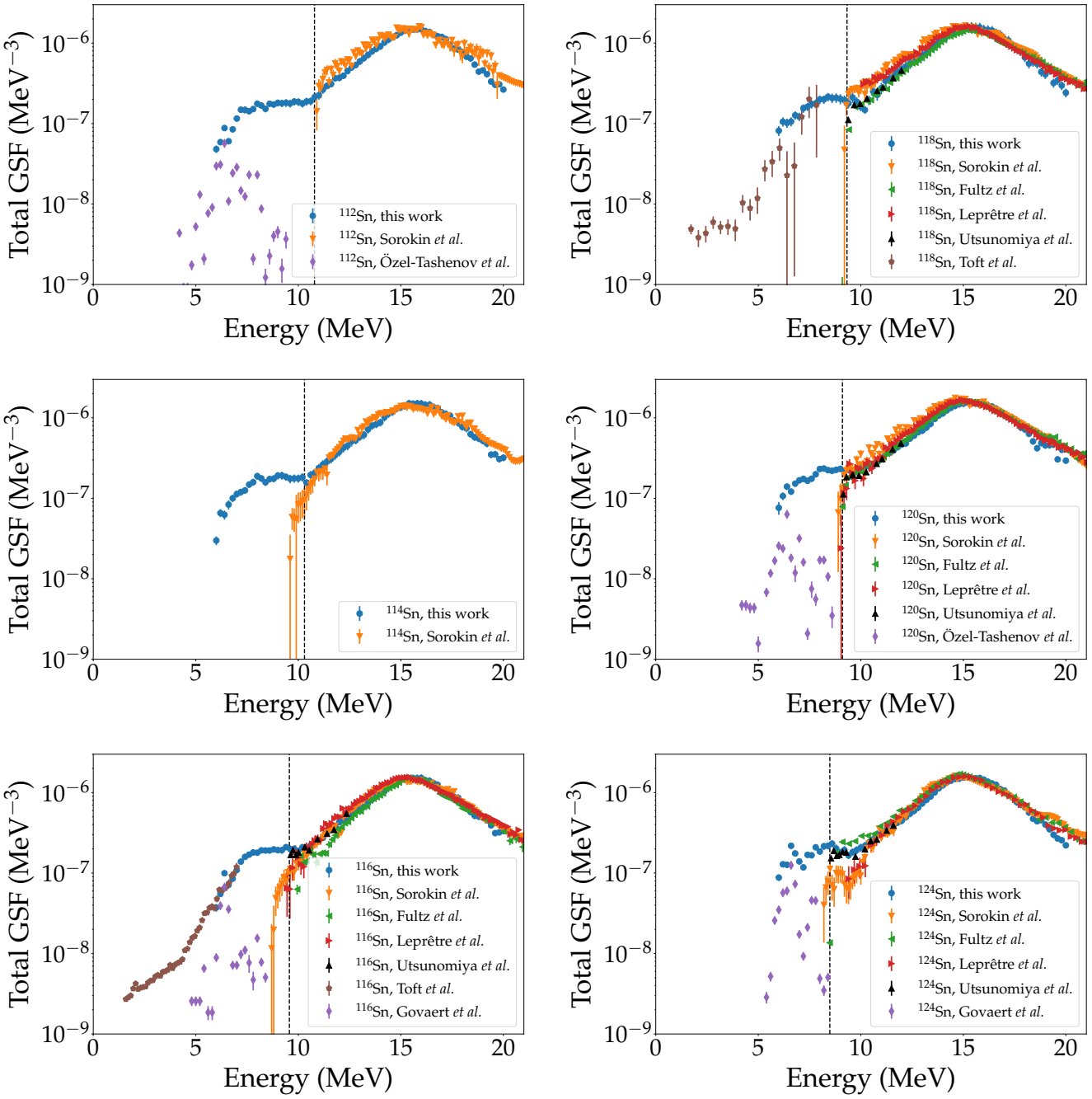

Figure 6.12: Total gamma strength functions for stable tin isotopes from present work in comparison to results from photoabsorption experiments by Sorokin *et al.* [116, 117], Fultz *et al.* [118], Leprêtre *et al.* [119], Utsunomiya *et al.* [120, 121], NRF experiments by Özel-Tashenov *et al.* [126], Govaert *et al.* [127] and (^{3}He,^{3}He'γ), (^{3}He,$\alpha\gamma$) experiments performed by the Oslo group [150–152]. The neutron threshold is indicated by dashed lines.

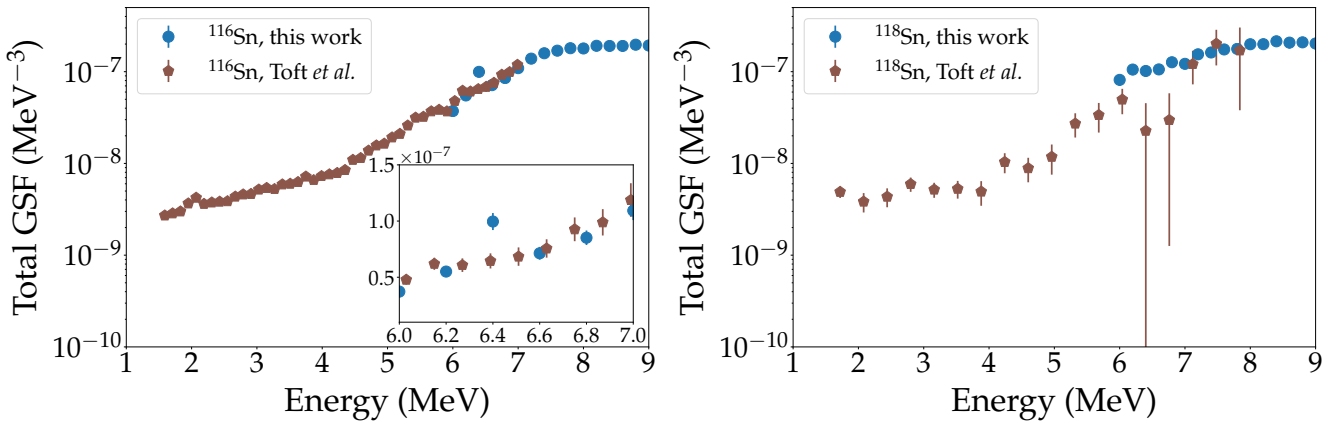

Figure 6.13: Low-energy part of the total gamma strength function for ^{116}Sn and ^{118}Sn obtained in this work in comparison to results from the Oslo group [150–152]. Results for ^{118}Sn obtained by the Oslo group were multiplied by a factor of 1.8 as suggested in [152].

Cyclotron Laboratory (OCL). These data are partly in agreement with proton scattering data in ^{118}Sn but start to deviate at lower energies. However, the uncertainties for this measurement are very large. In ^{116}Sn both data sets are in an excellent agreement. A closer look however, reveals a peak-like structure around 6.4 MeV in the proton scattering data (cf. Fig. 6.4), which is not seen in the Oslo-type experiments. This could be a hint for a violation of the Brink-Axel hypothesis. To investigate this enhancement further, the low-energy region of the GSF of the targets measured with high statistics (^{112,116,120,124}Sn) is shown in Fig. 6.14. The structure around 6.4 MeV can be seen in all isotopes and it seems to increase for heavier isotopes. It is particularly pronounced in ^{124}Sn, albeit slightly shifted by about 200 keV to higher energies. An increased amount of strength in this region is also found in studies with isoscalar probes as already discussed in Section 6.2 for ^{124}Sn.

6.6 Level densities

Level densities can be extracted from the inelastic proton scattering spectra by means of a fluctuation analysis. This method was initially developed for the analysis of β-delayed particle emission spectra [54]. Later it was also successfully applied to electron scattering data [153, 154], NRF data [155, 156] and inelastic proton scattering data [111, 157–159]. A detailed description of the method can be found in [54, 55].

Fluctuations in the measured cross section can emerge due to two different effects. If the mean level width $\langle\Gamma\rangle$ is smaller than the mean level spacing $\langle D\rangle$, fluctuations arise from the high density of unresolved states and their incoherent overlap due to the finite resolution of the used detectors. In this case one is concerned with Porter-Thomas fluctuations [160]. For even higher level densities the mean level spacing $\langle D\rangle$ becomes smaller than the mean level width $\langle\Gamma\rangle$. In this case fluctuations arise from coherent overlapping of the widths. These so-

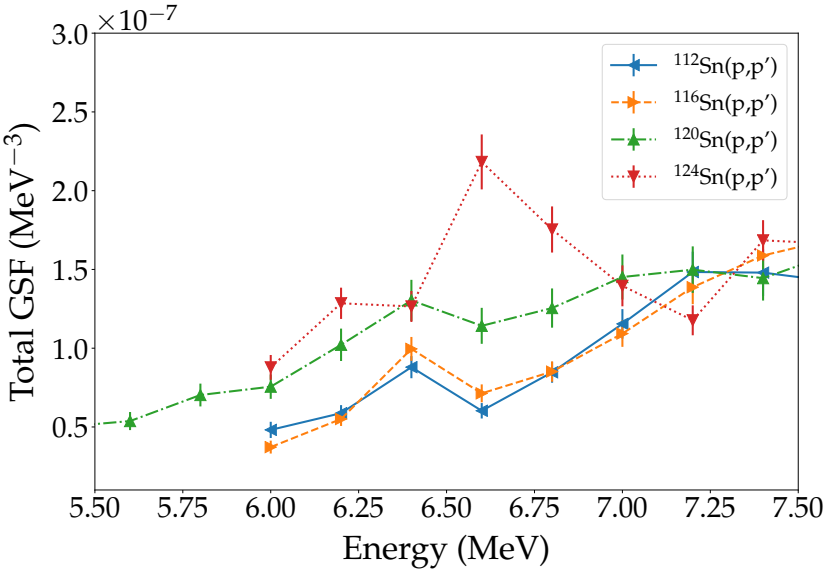

Figure 6.14: Gamma strength function of the main tin isotopes for the low-energy region. Due to higher statistics the GSF for ^{120}Sn was calculated using proton scattering data from Ref. [73].

called Ericson fluctuations [161] are then characterised by their coherence width instead of the width of the respective individual levels. Although the fluctuation analysis presented in this section is in principle applicable to both cases, very high statistics in the experimental data is necessary in the case of Ericson fluctuations [162] which limits the analysis in practise only to the Porter-Thomas regime.

In order to perform the fluctuation analysis, further assumptions concerning the level spacing and the level width need to be made. The probability to find a certain level spacing D between two neighbouring levels is assumed to be given by the Wigner distribution [163]

$$P_W(x) = \frac{\pi x}{2} \exp\left(-\frac{\pi x^2}{4}\right), \tag{6.12}$$

where $x = D/\langle D \rangle$ is the level spacing in units of its mean value. The probability to observe a width Γ of a single state is assumed to follow the Porter-Thomas distribution [160]

$$P_{PT}(x) = \frac{1}{\sqrt{2\pi x}} \exp\left(-\frac{x}{2}\right), \tag{6.13}$$

where $x = \Gamma/\langle \Gamma \rangle$ is the width in units of its mean value. Both distributions are illustrated in Fig. 6.15. The Wigner distribution shows a suppression for small spacings, which is typical for classical chaotic systems and has a maximum around the mean spacing. Such a behaviour for level spacings was confirmed in neutron resonance experiments [164]. The Porter-Thomas dis-

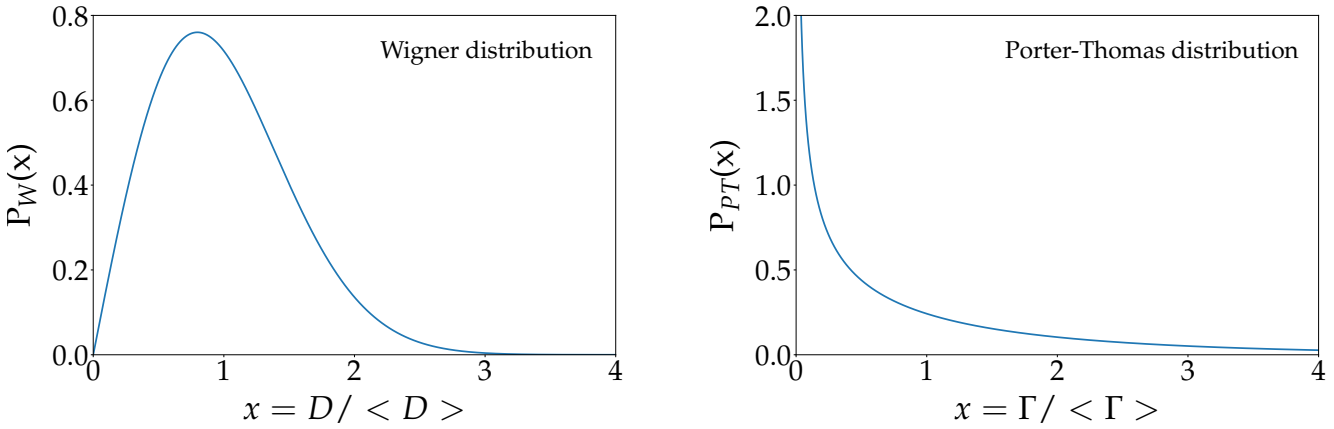

Figure 6.15: Normalised Wigner [163] (left) and Porter-Thomas [160] (right) distributions.

tribution suggests that weak transitions are strongly favoured. In experiments this is apparent by many levels having small strengths while a few have large strengths.

The steps of the fluctuation analysis for the ^{124}Sn(p,p') data are illustrated in Fig. 6.16. First, the background shown in the upper panel of the figure is subtracted from the spectrum. Here, the background consists of all contributions to the spectrum that do not belong to the excitation mode under investigation. This is taken from the MDA. In the second step the background subtracted spectrum is convoluted with a Gaussian function having a width $\Delta E_< = 2\sqrt{2\ln 2}\sigma_<$ smaller than the experimental resolution ΔE to reduce uncertainties stemming from finite statistics. It should be noted that this step can be omitted and the background subtracted spectrum can be used directly. However, in this case one has to correct the contribution stemming from counting statistics in the autocorrelation function as discussed later. A second spectrum is produced by smoothing the background subtracted spectrum with a width $\Delta E_> = 2\sqrt{2\ln 2}\sigma_>$ larger than the experimental resolution ΔE. In this way gross structures are removed from the spectrum. Both spectra convoluted with the Gaussian functions as described are shown in the middle panel of Fig. 6.16 denoted as $g_<(E_x)$ and $g_>(E_x)$. Finally, in the third panel the so-called stationary spectrum is shown defined as

$$d(E_x) = \frac{g_<(E_x)}{g_>(E_x)}. \tag{6.14}$$

The dimensionless stationary spectrum $d(E_x)$ is fluctuating around the mean value $\langle d(E_x)\rangle = 1$. One can directly infer from the intensity of the fluctuations that the level density increases with increasing excitation energy. In the low energy region the spacing is relatively small, so that larger fluctuations arise. With increasing excitation energy the spacing is decreasing which leads to reduced fluctuation intensity due to incoherent overlapping of levels. At even higher

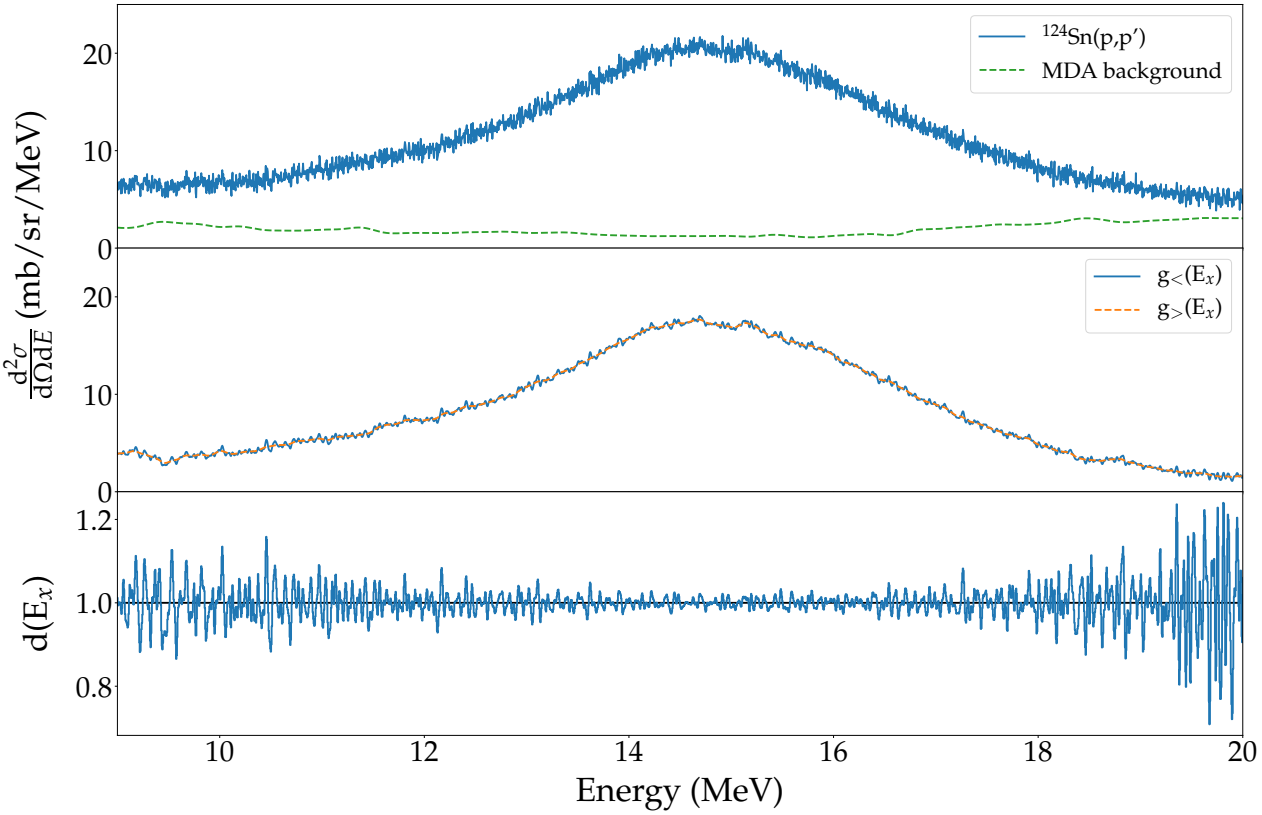

Figure 6.16: Full acceptance spectrum of the ^{124}Sn(p,p') reaction at $\theta_{lab} = 0^{\circ}$ and the background obtained from the MDA (top panel). Background subtracted de-noised $g_{<}(E_x)$ and smoothed $g_{>}(E_x)$ spectra (middle panel). Stationary spectrum $d(E_x)$ (bottom panel).

excitation energies Ericson fluctuations occur due to the coherent overlapping of levels. As a consequence the fluctuation intensity increases again.

A quantitative measure for the fluctuations observed in the stationary spectrum is the autocorrelation function

$$C(\varepsilon) = \frac{\langle \mathrm{d}(E_x)\mathrm{d}(E_x+\varepsilon)\rangle}{\langle \mathrm{d}(E_x)\rangle \langle \mathrm{d}(E_x+\varepsilon)\rangle}, \tag{6.15}$$

where ε is the offset energy. The experimental autocorrelation function can be approximated by the following analytical form [54]

$$C(\varepsilon) = 1 + \frac{\alpha \langle D\rangle}{2\sigma_< \sqrt{\pi}} \left[\exp\left(-\frac{\varepsilon^2}{4\sigma_<^2}\right) + \frac{1}{y}\exp\left(-\frac{\varepsilon^2}{4\sigma_<^2 y^2}\right) - \sqrt{\frac{8}{1+y^2}}\exp\left(-\frac{\varepsilon^2}{2\sigma_<^2(1+y^2)}\right)\right], \tag{6.16}$$

where $y = \sigma_>/\sigma_<$ and $\langle D\rangle$ the level spacing. The parameter α is the sum of the intensity variance α_I and the spacing variance α_D. If the investigated spectrum contains only one class of states, as is the case for the GDR region, where $J^\pi = 1^-$ states are dominantly excited, then the total variance α is given by the sum of the normalised Porter-Thomas and Wigner distribution variances $\alpha = \alpha_{PT} + \alpha_W = 2 + 0.273$. The situation is more complex in the PDR region, where also a considerable amount of M1 cross sections are found. In Ref. [165] a range of variances for α_D and α_I was estimated assuming different ratios of level densities and transition strengths (i.e intensities) of two classes of states N_1 and N_2. For the variance α_D it was found $\alpha_D = 0.273$ for the cases $N_1 \gg N_2$ and $N_1 \ll N_2$. For the case $N_1 = N_2$ the variance is $\alpha_D = 0.520$. In this work it was assumed that $N_1 = N_2$, since both classes of states have $J = 1$. The variance α_I can be calculated for two classes of states as follows [166]

$$\alpha_I = 3\frac{(N_1\langle I_1\rangle^2 + N_2\langle I_2\rangle^2)(N_1+N_2)}{(N_1\langle I_1\rangle + N_2\langle I_2\rangle)^2} - 1, \tag{6.17}$$

where $\langle I_i\rangle$ is the intensity of class N_i. In Fig. 6.17 the intensity variance α_I is shown as a function of $\beta = \frac{N_1\langle I_1\rangle}{N_2\langle I_2\rangle}$ for a variety of N_1/N_2 ratios. One can see that $\alpha_I \geq 2$ in all cases. For the case $N_1 = N_2$ the parameter β reduces to $\beta = \langle I_1\rangle/\langle I_2\rangle$. In the PDR region this ratio is nothing else but the ratio of the E1 and M1 cross sections, which can be obtained from the MDA.

Evaluating Eqn. (6.15) and Eqn. (6.16) at $C(\varepsilon = 0) - 1$ one obtains the following expressions

$$C(0) - 1 = \frac{\langle \mathrm{d}(E_x)^2\rangle - \langle \mathrm{d}(E_x)\rangle^2}{\langle \mathrm{d}(E_x)\rangle^2}, \tag{6.18}$$

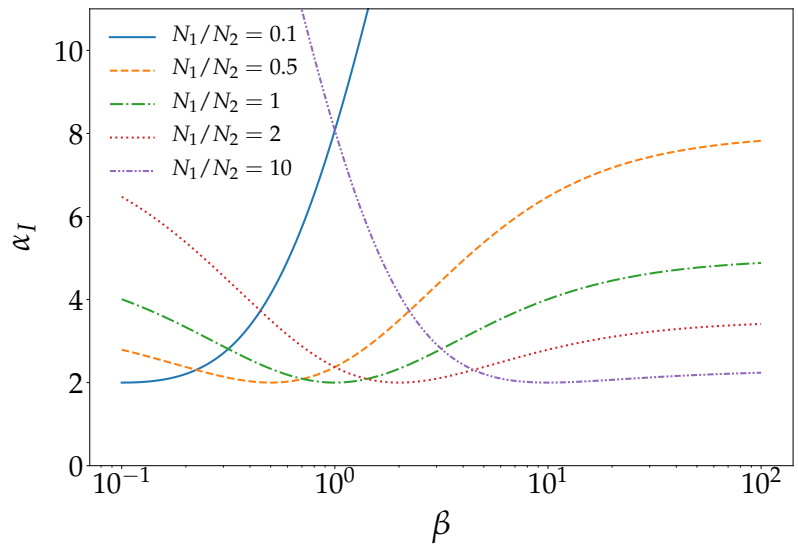

Figure 6.17: Normalised intensity variance assuming two classes of states with different ratios of levels.

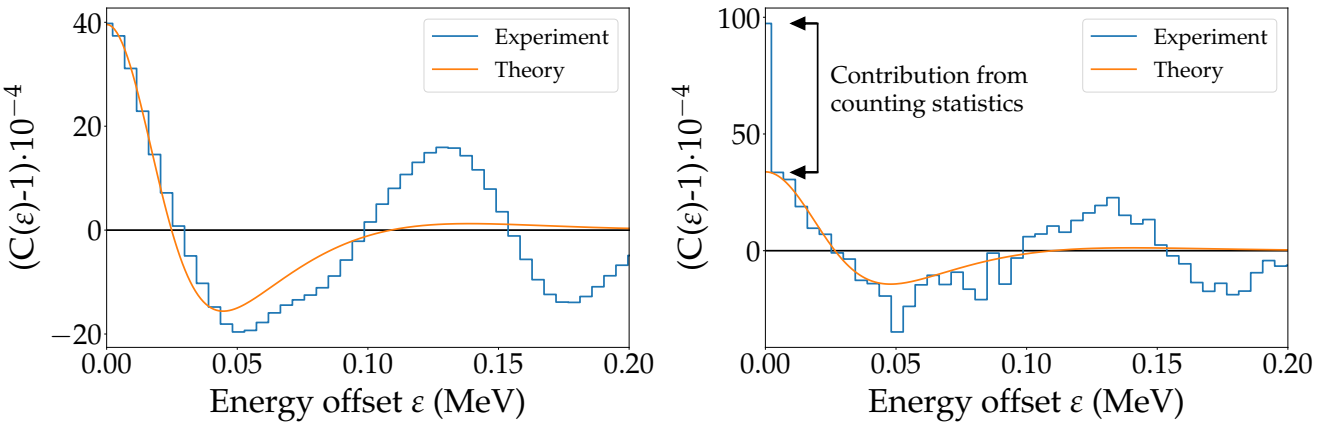

Figure 6.18: Autocorrelation function at an excitation energy of 8 MeV using a de-noised (left) and a raw (right) spectrum.

$$C(0) - 1 = \frac{\alpha \langle D \rangle}{2\sigma_< \sqrt{\pi}} \left(1 + \frac{1}{y} - \sqrt{\frac{8}{1+y^2}} \right). \tag{6.19}$$

With the knowledge of α, $\sigma_<$ and y the level spacing $\langle D \rangle$ can be directly extracted. For the case of two classes N_1 and N_2 the spacing for one of the classes is given by

$$\langle D \rangle = \frac{N_1}{N_1 + N_2} \langle D_1 \rangle, \tag{6.20}$$

which reduces to $\langle D \rangle = \langle D_1 \rangle / 2$ for $N_1 = N_2$. The level density can then be obtained from $\rho = 1/\langle D \rangle$.

In Fig. 6.18 the autocorrelation function at an excitation energy of 8 MeV is shown. On the

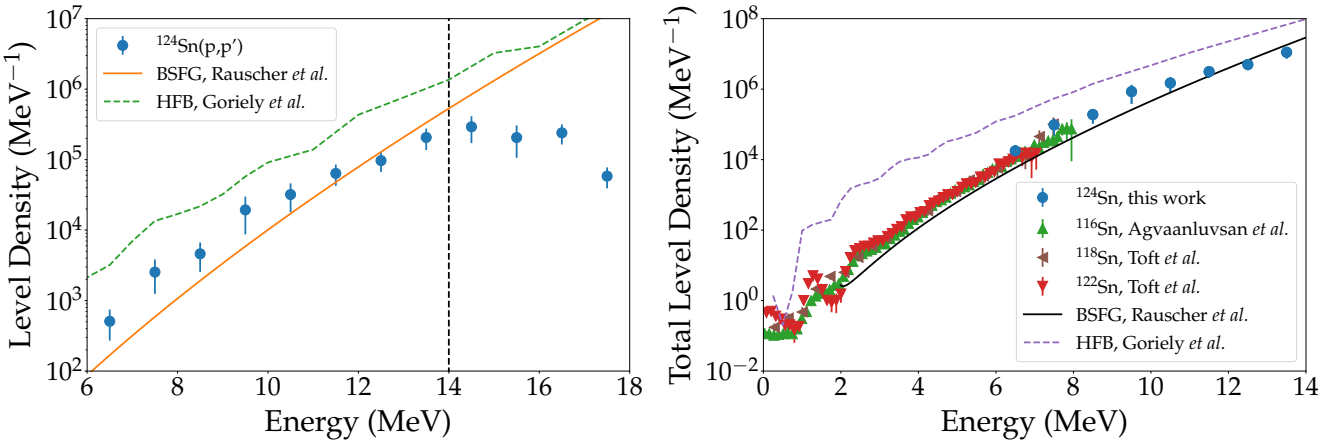

Figure 6.19: Extracted level density of ^{124}Sn for 1^- states (left) and the corresponding total level density (right) in comparison to results from Oslo experiments [150–152] and model calculations [167, 168].

left side the investigated spectrum was de-noised by convolving it with a Gaussian having the width $\sigma_<$ as described earlier, whereas on the right side the spectrum was used directly. As a consequence one can see at $\varepsilon = 0$ a significant contribution from uncorrelated statistical noise which needs to be corrected for. This can be done by fitting Eqn. (6.19) to the experimental data using the experimental resolution. Results from both techniques agree well. Pre-smoothing the spectrum with a narrow Gaussian is usually a simple and reliable method to deal with statistical noise. However, in cases where one deals with low statistics spectra it is advisable to use the investigated spectrum directly and correct the autocorrelation function for the statistical contribution explicitly. In this work pre-smoothing was used in the GDR region, while in the low-energy region up to $E_x = 10\,\mathrm{MeV}$, the statistical contribution was corrected explicitly.

In this work the level density could be extracted so far only for ^{124}Sn as the data for this isotope have by far the best statistics. The results are shown in Fig. 6.19. On the left side the level density for 1^- states is shown in comparison to the widely used back-shifted Fermi gas model (BSFG) with the parametrisation of Rauscher *et al.* [167] and a Hartree-Fock-Bogoliubov (HFB) calculation from Goriely *et al.* [168]. Neither can reproduce the experimental results accurately which lie in between of the two models. The dashed line indicates the range of applicability of the fluctuation analysis limited at higher energies due to Ericson fluctuations.

The Oslo group extracted level densities for ^{116}Sn, ^{118}Sn and ^{122}Sn from (^{3}He,^{3}He'γ) and (^{3}He,$\alpha\gamma$) experiments performed at the Oslo Cyclotron Laboratory (OCL). Although ^{124}Sn was not measured in these experiments, it is worthwhile to compare the level densities obtained in this work with the results obtained by the Oslo group as the level density should be similar in all tin isotopes due to their similar underlying structure. However, the level densities derived from the Oslo experiments represent a different spin window depending on the specific reaction. Total level densities are obtained from a normalisation to level densities from neutron

capture experiments close to the threshold. Thus the level density for 1^- states obtained in this work needs to be converted to the total level density as well in order to be able to compare the results attained in different experiments. This can be achieved by using the following equation

$$\rho_{tot}(E_x) = \frac{2\rho(E_x, J^\pi)}{f(J)}, \tag{6.21}$$

where $\rho_{tot}(E_x)$ is the total level density and $\rho(E_x, J^\pi)$ is the level density for transitions with spin J and parity π. The so-called spin distribution function $f(J)$ is given by

$$f(J) = \frac{2J+1}{2\sigma^2} \exp\left(\frac{-J(J+1)}{2\sigma^2}\right), \tag{6.22}$$

where σ is the spin cutoff parameter. It should be noted that several slightly different forms for the spin distribution function exist. Here, the definition and parametrisation from Rauscher *et al.* [167] is used.

On the right side of Fig. 6.19 the resulting total level density for ^{124}Sn is shown in comparison to results obtained by the Oslo group for ^{116}Sn, ^{118}Sn, ^{122}Sn and model calculations. The model calculations again cannot reproduce the experimental data, whereas the level densities obtained from the different experiments are in a reasonable agreement between each other within the uncertainties. The level densities extracted from the fluctuation analysis provide an independent check of the assumptions underlying the analysis of the Oslo-type data, where only the product of GSF and level density can be determined and additional assumptions are needed for a decomposition, namely a separable approach and normalisation to level densities at neutron threshold [56].

7 Summary and outlook

In this work the dipole response of the even-even stable tin isotopes $^{112-124}$Sn was investigated with inelastic proton scattering. The experiments were performed at the Research Center for Nuclear Physics (RCNP) in Osaka, Japan, using a 295 MeV proton beam. Scattered protons were measured at 0°, 2.5° and 4.5° in an excitation energy range of $5 - 26$ MeV using the Grand Raiden and Large Acceptance spectrometers.

Double differential cross sections were determined and individual contributions from different multipoles were extracted by means of a multipole decomposition analysis. The main contributions are of E1 and M1 nature. Utilising the equivalent photon method photoabsorption cross sections were extracted. The results were compared to photoabsorption experiments, where a fair agreement in the GDR peak region was found for most of the data sets. Towards the neutron threshold, however, considerable deviations were found. Recent (γ,n) experiments are in good agreement with results obtained in this work.

B(E1) strength distributions were determined and compared below the neutron threshold to NRF experiments, where data on ^{112,116,120,124}Sn are available. Considerably more strength was found for all cases in the present work, confirming previous findings for ^{120}Sn [98]. Furthermore, an accumulation of strength is found around 6.5 MeV in all tin isotopes being most prominent in ^{124}Sn. Comparison with isoscalar probes for ^{124}Sn suggest a PDR splitting into an isoscalar/isovector part, excited also by (^{17}O,^{17}O'γ) and (α,$\alpha'\gamma$) experiments and a pure isovector part excited by the (p,p') and (γ,γ') experiments.

The dipole polarisability was determined in an energy region between 6 and 30 MeV and compared to model calculations based on energy density functional theory. Most of the model calculations cannot reproduce the experimental results. The dipole polarisability obtained in this work provides new constraints for theoretical model calculations and especially on the density dependence of the symmetry energy. Model calculations in the future will benefit greatly from these new results allowing a systematic study of the dipole polarisability as a function of the neutron number.

Using the so-called unit cross section technique electromagnetic B(M1) strength distributions were determined and total M1 strength is provided for the first time for stable even-even tin isotopes $^{112-120,124}$Sn.

The total gamma strength function was determined including the E1 and M1 contributions and compared to results from NRF, photoabsorption and Oslo-type experiments. A fair agreement was found in the GDR region. The NRF results are considerably lower as already seen in B(E1) strength distributions. In the PDR region data on ^{116}Sn and ^{118}Sn are available from (^{3}He,^{3}He'γ) and (^{3}He,$\alpha\gamma$) experiments. Results for ^{116}Sn are in excellent agreement. In ^{118}Sn

good agreement is found within the uncertainties. However, a localised peak is found in all isotopes around 6.5 MeV which is not seen in (^{3}He,^{3}He'γ) and (^{3}He,$\alpha\gamma$) experiments. This could be an evidence for a violation of the Brink-Axel hypothesis.

Finally, using the so-called fluctuation analysis level densities were extracted for ^{124}Sn in an excitation energy region of $6-15$ MeV for 1^- states. These level densities were converted to the total level density and compared to results from (^{3}He,^{3}He'γ) and (^{3}He,$\alpha\gamma$) experiments, where level densities for ^{116,118,122}Sn are available. A fair agreement between these level densities is found.

The tin isotope chain is unique for systematic studies because it provides a wide mass range with little change of the underlying structure. Therefore, it is not surprising that a lot of effort is put into systematic experimental study of their properties. Analysis of dipole strength in $^{124-132}$Sn measured in Coulomb excitation at GSI is ongoing, which will provide exciting complementary results for neutron-rich tin isotopes [169]. Additional experimental studies on stable tin isotopes are planned at the NEPTUN [170] set-up at TU Darmstadt, using the total photoabsorption technique [171]. (γ, xn) experiments at the synchrotron radiation facility NewSUBARU [172] are planned promising additional data, which will allow to determine more precisely the dipole polarisability contributions between 20 and 40 MeV. Finally, new Oslo-type experiments have been performed for ^{120,124}Sn, which will shed further light at a possible violation of the Brink-Axel hypothesis below the neutron threshold.

Bibliography

[1] P. Lipas, Nucl. Phys. **82** (1966) 91 .

[2] D. Savran, T. Aumann, and A. Zilges, Prog. Part. Nucl. Phys. **70** (2013) 210 .

[3] P. Papakonstantinou, H. Hergert, V. Y. Ponomarev, and R. Roth, Phys. Rev. C **89** (2014) 034306.

[4] V. O. Nesterenko, J. Kvasil, A. Repko, W. Kleinig, and P.-G. Reinhard, Phys. Atom. Nucl. **79** (2016) 842.

[5] B. L. Berman and S. C. Fultz, Rev. Mod. Phys. **47** (1975) 713.

[6] A. Tamii, Y. Fujita, H. Matsubara, T. Adachi, J. Carter, M. Dozono, H. Fujita, K. Fujita, H. Hashimoto, K. Hatanaka, T. Itahashi, M. Itoh, T. Kawabata, K. Nakanishi, S. Ninomiya, A. Perez-Cerdan, L. Popescu, B. Rubio, T. Saito, H. Sakaguchi, Y. Sakemi, Y. Sasamoto, Y. Shimbara, Y. Shimizu, F. Smit, Y. Tameshige, M. Yosoi, and J. Zenhiro, Nucl. Instrum. Methods **605** (2009) 326 .

[7] P. von Neumann-Cosel and A. Tamii, Eur. Phys. J. A **55** (2019) 110.

[8] A. Bracco, E. Lanza, and A. Tamii, Prog. Part. Nucl. Phys. **106** (2019) 360 .

[9] S. Goriely, E. Khan, and M. Samyn, Nucl. Phys. A **739** (2004) 331 .

[10] E. Litvinova, H. Loens, K. Langanke, G. Martínez-Pinedo, T. Rauscher, P. Ring, F.-K. Thielemann, and V. Tselyaev, Nucl. Phys. A **823** (2009) 26 .

[11] I. Daoutidis and S. Goriely, Phys. Rev. C **86** (2012) 034328.

[12] J. Piekarewicz, Phys. Rev. C **73** (2006) 044325.

[13] N. Tsoneva and H. Lenske, Phys. Rev. C **77** (2008) 024321.

[14] E. Litvinova, P. Ring, V. Tselyaev, and K. Langanke, Phys. Rev. C **79** (2009) 054312.

[15] E. Litvinova, P. Ring, and V. Tselyaev, Phys. Rev. Lett. **105** (2010) 022502.

[16] D. Savran, M. Babilon, A. M. van den Berg, M. N. Harakeh, J. Hasper, A. Matic, H. J. Wörtche, and A. Zilges, Phys. Rev. Lett. **97** (2006) 172502.

[17] J. Endres, D. Savran, A. M. v. d. Berg, P. Dendooven, M. Fritzsche, M. N. Harakeh, J. Hasper, H. J. Wörtche, and A. Zilges, Phys. Rev. C **80** (2009) 034302.

[18] J. Endres, D. Savran, P. A. Butler, M. N. Harakeh, S. Harissopulos, R.-D. Herzberg, R. Krücken, A. Lagoyannis, E. Litvinova, N. Pietralla, V. Ponomarev, L. Popescu, P. Ring, M. Scheck, F. Schlüter, K. Sonnabend, V. I. Stoica, H. J. Wörtche, and A. Zilges, Phys. Rev. C **85** (2012) 064331.

[19] L. Pellegri, A. Bracco, F. Crespi, S. Leoni, F. Camera, E. Lanza, M. Kmiecik, A. Maj, R. Avigo, G. Benzoni, N. Blasi, C. Boiano, S. Bottoni, S. Brambilla, S. Ceruti, A. Giaz, B. Million, A. Morales, R. Nicolini, V. Vandone, O. Wieland, D. Bazzacco, P. Bednarczyk, M. Bellato, B. Birkenbach, D. Bortolato, B. Cederwall, L. Charles, M. Ciemala, G. D. Angelis *et al.*, Phys. Lett. B **738** (2014) 519 .

[20] A. Klimkiewicz, N. Paar, P. Adrich, M. Fallot, K. Boretzky, T. Aumann, D. Cortina-Gil, U. D. Pramanik, T. W. Elze, H. Emling, H. Geissel, M. Hellström, K. L. Jones, J. V. Kratz, R. Kulessa, C. Nociforo, R. Palit, H. Simon, G. Surówka, K. Sümmerer, D. Vretenar, and W. Waluś, Phys. Rev. C **76** (2007) 051603.

[21] J. Piekarewicz, Phys. Rev. C **83** (2011) 034319.

[22] J. Piekarewicz, B. K. Agrawal, G. Colò, W. Nazarewicz, N. Paar, P.-G. Reinhard, X. Roca-Maza, and D. Vretenar, Phys. Rev. C **85** (2012) 041302.

[23] A. Carbone, G. Colò, A. Bracco, L.-G. Cao, P. F. Bortignon, F. Camera, and O. Wieland, Phys. Rev. C **81** (2010) 041301.

[24] F. J. Fattoyev, J. Piekarewicz, and C. J. Horowitz, Phys. Rev. Lett. **120** (2018) 172702.

[25] M. B. Tsang, J. R. Stone, F. Camera, P. Danielewicz, S. Gandolfi, K. Hebeler, C. J. Horowitz, J. Lee, W. G. Lynch, Z. Kohley, R. Lemmon, P. Möller, T. Murakami, S. Riordan, X. Roca-Maza, F. Sammarruca, A. W. Steiner, I. Vidaña, and S. J. Yennello, Phys. Rev. C **86** (2012) 015803.

[26] M. Oertel, M. Hempel, T. Klähn, and S. Typel, Rev. Mod. Phys. **89** (2017) 015007.

[27] B. P. Abbott, R. Abbott, T. D. Abbott, F. Acernese, K. Ackley, C. Adams, T. Adams, P. Addesso, R. X. Adhikari, V. B. Adya, C. Affeldt, M. Afrough, B. Agarwal, M. Agathos, K. Agatsuma, N. Aggarwal, O. D. Aguiar, L. Aiello, A. Ain, P. Ajith, B. Allen, G. Allen, A. Allocca, P. A. Altin, A. Amato, A. Ananyeva, S. B. Anderson, W. G. Anderson, S. V. Angelova, S. Antier *et al.*, Phys. Rev. Lett. **119** (2017) 161101.

[28] E. R. Most, L. R. Weih, L. Rezzolla, and J. Schaffner-Bielich, Phys. Rev. Lett. **120** (2018) 261103.

[29] X. Roca-Maza and N. Paar, Prog. Part. Nucl. Phys. **101** (2018) 96 .

[30] T. Nikšić, D. Vretenar, P. Finelli, and P. Ring, Phys. Rev. C **66** (2002) 024306.

[31] X. Roca-Maza, N. Paar, and G. Colò, J. Phys. G **42** (2015) 034033.

[32] X. Roca-Maza, X. Viñas, M. Centelles, B. K. Agrawal, G. Colò, N. Paar, J. Piekarewicz, and D. Vretenar, Phys. Rev. C **92** (2015) 064304.

[33] K. Heyde, P. von Neumann-Cosel, and A. Richter, Rev. Mod. Phys. **82** (2010) 2365.

[34] K. Langanke, G. Martínez-Pinedo, P. von Neumann-Cosel, and A. Richter, Phys. Rev. Lett. **93** (2004) 202501.

[35] K. Langanke, G. Martínez-Pinedo, B. Müller, H.-T. Janka, A. Marek, W. R. Hix, A. Juodagalvis, and J. M. Sampaio, Phys. Rev. Lett. **100** (2008) 011101.

[36] H. P. Loens, K. Langanke, G. Martínez-Pinedo, and K. Sieja, Eur. Phys. J. A **48** (2012) 34.

[37] T. Otsuka, T. Suzuki, R. Fujimoto, H. Grawe, and Y. Akaishi, Phys. Rev. Lett. **95** (2005) 232502.

[38] F. Osterfeld, Rev. Mod. Phys. **64** (1992) 491.

[39] J. D. Vergados, H. Ejiri, and F. Simkovic, Rep. Prog. Phys. **75** (2012) 106301.

[40] G. A. Bartholomew, E. D. Earle, A. J. Ferguson, J. W. Knowles, and M. A. Lone, *Gamma-Ray Strength Functions*, Springer US, Boston (1973).

[41] M. Arnould, S. Goriely, and K. Takahashi, Phys. Rep. **450** (2007) 97 .

[42] M. Chadwick, M. Herman, P. Obložinský, M. Dunn, Y. Danon, A. Kahler, D. Smith, B. Pritychenko, G. Arbanas, R. Arcilla, R. Brewer, D. Brown, R. Capote, A. Carlson, Y. Cho, H. Derrien, K. Guber, G. Hale, S. Hoblit, S. Holloway, T. Johnson, T. Kawano, B. Kiedrowski, H. Kim, S. Kunieda, N. Larson, L. Leal, J. Lestone, R. Little, E. McCutchan *et al.*, Nucl. Data Sheets **112** (2011) 2887 , special Issue on ENDF/B-VII.1 Library.

[43] M. Salvatores and G. Palmiotti, Prog. Part. Nucl. Phys. **66** (2011) 144 .

[44] D. Brink, Ph.D. thesis, Oxford University (1955).

[45] P. Axel, Phys. Rev. **126** (1962) 671.

[46] J. Ritman, F.-D. Berg, W. Kühn, V. Metag, R. Novotny, M. Notheisen, P. Paul, M. Pfeiffer, O. Schwalb, H. Löhner, L. Venema, A. Gobbi, N. Herrmann, K. D. Hildenbrand, J. Mösner, R. S. Simon, K. Teh, J. P. Wessels, and T. Wienold, Phys. Rev. Lett. **70** (1993) 533.

[47] A. Bracco, F. Camera, M. Mattiuzzi, B. Million, M. Pignanelli, J. J. Gaardhøje, A. Maj, T. Ramsøy, T. Tveter, and Z. Źelazny, Phys. Rev. Lett. **74** (1995) 3748.

[48] A. C. Larsen, M. Guttormsen, R. Chankova, F. Ingebretsen, T. Lönnroth, S. Messelt, J. Rekstad, A. Schiller, S. Siem, N. U. H. Syed, and A. Voinov, Phys. Rev. C **76** (2007) 044303.

[49] C. T. Angell, S. L. Hammond, H. J. Karwowski, J. H. Kelley, M. Krtička, E. Kwan, A. Makinaga, and G. Rusev, Phys. Rev. C **86** (2012) 051302.

[50] E. Litvinova and N. Belov, Phys. Rev. C **88** (2013) 031302.

[51] R. Schwengner, S. Frauendorf, and A. C. Larsen, Phys. Rev. Lett. **111** (2013) 232504.

[52] B. A. Brown and A. C. Larsen, Phys. Rev. Lett. **113** (2014) 252502.

[53] A. Schiller, A. Voinov, E. Algin, J. Becker, L. Bernstein, P. Garrett, M. Guttormsen, R. Nelson, J. Rekstad, and S. Siem, Phys. Lett. B **633** (2006) 225 .

[54] B. Jonson, E. Hagberg, P. G. Hansen, P. Hornshøj, and P. Tidemand-Petersson, 3rd International Conference on Nuclei Far from Stability (1976) 22 p.

[55] P. Hansen, B. Jonson, and A. Richter, Nucl. Phys. A **518** (1990) 13 .

[56] A. Schiller, L. Bergholt, M. Guttormsen, E. Melby, J. Rekstad, and S. Siem, Nucl. Instrum. Methods **447** (2000) 498 .

[57] G. R. Satchler, *Direct Nuclear Reactions*, Oxford University Press, New York (1983).

[58] K. Amos, P. J. Dortmans, H. V. von Geramb, S. Karataglidis, and J. Raynal, Adv. Nucl. Phys. **25** (2000) 275.

[59] A. Winther and K. Alder, Nucl. Phys. A **319** (1979) 518 .

[60] W. G. Love and M. A. Franey, Phys. Rev. C **24** (1981) 1073.

[61] E. Rutherford, Philos. Mag. **21** (1911) 669.

[62] E. Fermi, Z. Phys. **29** (1924) 315.

[63] C. F. v. Weizsäcker, Z. Phys. **88** (1934) 612.

[64] E. J. Williams, Phys. Rev. **45** (1934) 729.

[65] E. J. Williams, Kong. Dan. Vid. Sel. Mat. Fys. Med. **13N4** (1935) 1.

[66] J. D. Jackson, *Classical Electrodynamics*, Wiley, New York (1975).

[67] C. A. Bertulani and G. Baur, Phys. Rep. **163** (1988) 299 .

[68] S. Bassauer, *Aufbau und Test der Elektronik für ein Elektronenstreukoinzidenzexperiment und Vergleich der Photoabsorptionsquerschnitte in relativistischer Protonenstreuung mit elektromagnetischen Proben*, Master's thesis, TU Darmstadt (2014).

[69] C. Bertulani and A. Nathan, Nucl. Phys. A **554** (1993) 158 .

[70] N. Ryezayeva, T. Hartmann, Y. Kalmykov, H. Lenske, P. von Neumann-Cosel, V. Y. Ponomarev, A. Richter, A. Shevchenko, S. Volz, and J. Wambach, Phys. Rev. Lett. **89** (2002) 272502.

[71] B. Reitz, A. van den Berg, D. Frekers, F. Hofmann, M. de Huu, Y. Kalmykov, H. Lenske, P. von Neumann-Cosel, V. Ponomarev, S. Rakers, A. Richter, G. Schrieder, K. Schweda, J. Wambach, and H. Wörtche, Phys. Lett. B **532** (2002) 179 .

[72] I. Poltoratska, P. von Neumann-Cosel, A. Tamii, T. Adachi, C. A. Bertulani, J. Carter, M. Dozono, H. Fujita, K. Fujita, Y. Fujita, K. Hatanaka, M. Itoh, T. Kawabata, Y. Kalmykov, A. M. Krumbholz, E. Litvinova, H. Matsubara, K. Nakanishi, R. Neveling, H. Okamura, H. J. Ong, B. Özel-Tashenov, V. Y. Ponomarev, A. Richter, B. Rubio, H. Sakaguchi, Y. Sakemi, Y. Sasamoto, Y. Shimbara, Y. Shimizu *et al.*, Phys. Rev. C **85** (2012) 041304.

[73] A. Krumbholz, P. von Neumann-Cosel, T. Hashimoto, A. Tamii, T. Adachi, C. Bertulani, H. Fujita, Y. Fujita, E. Ganioglu, K. Hatanaka, C. Iwamoto, T. Kawabata, N. Khai, A. Krugmann, D. Martin, H. Matsubara, R. Neveling, H. Okamura, H. Ong, I. Poltoratska, V. Ponomarev, A. Richter, H. Sakaguchi, Y. Shimbara, Y. Shimizu, J. Simonis, F. Smit, G. Susoy, J. Thies, T. Suzuki *et al.*, Phys. Lett. B **744** (2015) 7 .

[74] C. Bertulani and V. Ponomarev, Phys. Rep. **321** (1999) 139 .

[75] V. G. Soloviev, *Theory of Atomic Nuclei: Quasiparticles and Phonons*, IOP Publishing, Bristol (1992).

[76] J. Bardeen, L. N. Cooper, and J. R. Schrieffer, Phys. Rev. **108** (1957) 1175.

[77] A. Tamii, *Spin-flip excitations studied by high-resolution (p,p') scattering experiment at foward angles*, Seminar, TU Darmstadt (2005).

[78] Y. Masuda, T. Kitagaki, K. Hatanaka, M. Higuchi, S. Ishimoto, Y. Kiyanagi, K. Morimoto, S. Muto, and M. Yoshimura, Phys. Rev. Lett. **89** (2002) 284801.

[79] T. Shimoda, H. Miyatake, and S. Morinobu, Nucl. Instrum. Methods **70** (1992) 320 .

[80] H. Sakai, H. Okamura, H. Otsu, T. Wakasa, S. Ishida, N. Sakamoto, T. Uesaka, Y. Satou, S. Fujita, and K. Hatanaka, Nucl. Instrum. Methods **369** (1996) 120 .

[81] K. Hatanaka, K. Takahisa, H. Tamura, M. Sato, and I. Miura, Nucl. Instrum. Methods **384** (1997) 575 .

[82] M. Tanaka, *Annual Report*, Technical report, RCNP (1991).

[83] R. Geller, *Electron Cyclotron Resonance Ion Sources and ECR Plasmas*, IOP Publishing (1996).

[84] M. Fujiwara, H. Akimune, I. Daito, H. Fujimura, Y. Fujita, K. Hatanaka, H. Ikegami, I. Katayama, K. Nagayama, N. Matsuoka, S. Morinobu, T. Noro, M. Yoshimura, H. Sakaguchi, Y. Sakemi, A. Tamii, and M. Yosoi, Nucl. Instrum. Methods **422** (1999) 484 .

[85] N. Matsuoka, K. Hatanaka, S. Morinobu, T. Noro, A. Okihana, and K. Sagara, *Annual Report*, Technical report, RCNP (1991).

[86] H. Fujita, Y. Fujita, G. Berg, A. Bacher, C. Foster, K. Hara, K. Hatanaka, T. Kawabata, T. Noro, H. Sakaguchi, Y. Shimbara, T. Shinada, E. Stephenson, H. Ueno, and M. Yosoi, Nucl. Instrum. Methods **484** (2002) 17 .

[87] T. Noro, Y. Mizuno, H. Togawa, S. Hirata, N. Matsuoka, O. Kamigaito, F. Hiei, Y. Sakemi, H. Akimune, and T. Takahashi, *Annual Report*, Technical report, RCNP (1990).

[88] M. Yosoi, H. Akimune, I. Daito, M. Fujiwara, S. Hirata, T. Inomata, O. Kamigaito, M. Kawabata, T. Noro, Y. Sakemi, T. Takahashi, A. Tamii, S. Toyama, A. Yamagoshi, M. Yoshimura, and H. Sakaguchi, AIP Conf. Proc. **343** (1995) 157.

[89] T. Hashimoto, A. M. Krumbholz, P.-G. Reinhard, A. Tamii, P. von Neumann-Cosel, T. Adachi, N. Aoi, C. A. Bertulani, H. Fujita, Y. Fujita, E. Ganioğlu, K. Hatanaka, E. Ideguchi, C. Iwamoto, T. Kawabata, N. T. Khai, A. Krugmann, D. Martin, H. Matsubara, K. Miki, R. Neveling, H. Okamura, H. J. Ong, I. Poltoratska, V. Y. Ponomarev, A. Richter, H. Sakaguchi, Y. Shimbara, Y. Shimizu, J. Simonis *et al.*, Phys. Rev. C **92** (2015) 031305.

[90] A. Tamii, *Polarization transfer observables for proton inelastic scattering from ^{12}C at zero degrees*, Doctoral thesis, Kyoto University (1999).

[91] *Physics Analysis Workstation*, http://paw.web.cern.ch/paw/, accessed: 05.04.2019.

[92] *Anaconda Distribution*, https://www.anaconda.com/distribution/, accessed: 05.04.2019.

[93] G. F. Knoll, *Radiation Detection and Measurement*, Wiley, New York (2010).

[94] T. Kawabata, *Polarization transfer in the $^{16}O(p,p')$ reaction at forward angles and structure of the spin-dipole resonances* (2002), Doctoral thesis, Kyoto University (2002).

[95] H. Matsubara, *Isoscalar and isovector spin-M1 transitions from the even-even, $N = Z$ nuclei across the sd-shell region* (2010), Doctoral thesis, Osaka University (2010).

[96] I. Poltoratska, *Complete dipole response in ^{208}Pb from high-resolution polarized proton scattering at 0°*, Doctoral thesis D17, TU Darmstadt (2011).

[97] C. Iwamoto, *Pygmy Dipole Resonance and M1 Resonance in ^{90}Zr*, Doctoral thesis, Konan University (2012).

[98] A. M. Krumbholz, *Low-energy electric dipole response of ^{120}Sn from polarized proton scattering*, Doctoral thesis D17, TU Darmstadt (2014).

[99] A. Krugmann, *Off-Yrast low-spin structure of deformed nuclei at mass number $A \approx 150$*, Doctoral thesis D17, TU Darmstadt (2014).

[100] G. Steinhilber, *Simulation der Elektronenoptik des QCLAM-Spektrometers mit CST Studio Suite und Analyse von inelastischen Protonenstreudaten von Zr-Isotopen unter extremen Vorwärtswinkeln*, Master's thesis, TU Darmstadt (2016).

[101] I. Ou, *Study of γ rays emitted from giant resonances of ^{12}C and ^{16}O* (2017), Doctoral thesis, Okayama University (2017).

[102] *KINMAT*, iThemba Laboratory for Accelerator Based Sciences, Faure, South Africa, unpublished.

[103] J. Kelley, J. Purcell, and C. Sheu, Nucl. Phys. A **968** (2017) 71 .

[104] H. Fujita, G. Berg, Y. Fujita, K. Hatanaka, T. Noro, E. Stephenson, C. Foster, H. Sakaguchi, M. Itoh, T. Taki, K. Tamura, and H. Ueno, Nucl. Instrum. Methods **469** (2001) 55 .

[105] N. Fujita, H. Sakaguchi, Y. Maeda, A. Nonaka, H. Okamura, A. Tamii, J. Zenihiro, H. Matsubara, D. Ishikawa, T. Terashima, and Y. Yasuda, *Annual Report*, Technical report, RCNP (2008).

[106] T. Wakasa, H. Sakai, H. Okamura, H. Otsu, N. Sakamoto, T. Uesaka, Y. Satou, S. Fujita, S. Ishida, M. Greenfield, N. Koori, A. Okihana, and K. Hatanaka, Nucl. Phys. A **599** (1996) 217 , Proceedings of the Groningen Conference on Giant Resonances.

[107] T. Wakasa, H. Sakai, H. Okamura, H. Otsu, S. Fujita, S. Ishida, N. Sakamoto, T. Uesaka, Y. Satou, M. B. Greenfield, and K. Hatanaka, Phys. Rev. C **55** (1997) 2909.

[108] B. Bonin, N. Alamanos, B. Berthier, G. Bruge, H. Faraggi, D. Legrand, J. Lugol, W. Mittig, L. Papineau, A. Yavin, D. Scott, M. Levine, J. Arvieux, L. Farvacque, and M. Buenerd, Nucl. Phys. A **430** (1984) 349 .

[109] T. Li, U. Garg, Y. Liu, R. Marks, B. K. Nayak, P. V. Madhusudhana Rao, M. Fujiwara, H. Hashimoto, K. Nakanishi, S. Okumura, M. Yosoi, M. Ichikawa, M. Itoh, R. Matsuo, T. Terazono, M. Uchida, Y. Iwao, T. Kawabata, T. Murakami, H. Sakaguchi, S. Terashima,

Y. Yasuda, J. Zenihiro, H. Akimune, K. Kawase, and M. N. Harakeh, Phys. Rev. C **81** (2010) 034309.

[110] M. Itoh, S. Kishi, H. Sakaguchi, H. Akimune, M. Fujiwara, U. Garg, K. Hara, H. Hashimoto, J. Hoffman, T. Kawabata, K. Kawase, T. Murakami, K. Nakanishi, B. K. Nayak, S. Terashima, M. Uchida, Y. Yasuda, and M. Yosoi, Phys. Rev. C **88** (2013) 064313.

[111] D. Martin, P. von Neumann-Cosel, A. Tamii, N. Aoi, S. Bassauer, C. A. Bertulani, J. Carter, L. Donaldson, H. Fujita, Y. Fujita, T. Hashimoto, K. Hatanaka, T. Ito, A. Krugmann, B. Liu, Y. Maeda, K. Miki, R. Neveling, N. Pietralla, I. Poltoratska, V. Y. Ponomarev, A. Richter, T. Shima, T. Yamamoto, and M. Zweidinger, Phys. Rev. Lett. **119** (2017) 182503.

[112] J. Raynal, *DWBA07*, NEA Computer Program Services, NEA-1209/08.

[113] V. Y. Ponomarev, priv. communication, TU Darmstadt (2018).

[114] C. Kalbach, Phys. Rev. C **41** (1990) 1656.

[115] M. N. Harakeh and A. van der Woude, *Giant Resonances*, Oxford University Press Inc., New York (2001).

[116] Y. I. Sorokin and B. A. Yur'ev, Yad. Fiz. **20** (1974) 233.

[117] Y. I. Sorokin and B. A. Yur'ev, Izv. AN. SSSR, Ser. Fiz. **39** (1975) 114.

[118] S. C. Fultz, B. L. Berman, J. T. Caldwell, R. L. Bramblett, and M. A. Kelly, Phys. Rev. **186** (1969) 1255.

[119] A. Leprêtre, H. Beil, R. Bergère, P. Carlos, A. D. Miniac, A. Veyssière, and K. Kernbach, Nucl. Phys. A **219** (1974) 39 .

[120] H. Utsunomiya, S. Goriely, M. Kamata, T. Kondo, O. Itoh, H. Akimune, T. Yamagata, H. Toyokawa, Y. W. Lui, S. Hilaire, and A. J. Koning, Phys. Rev. C **80** (2009) 055806.

[121] H. Utsunomiya, S. Goriely, M. Kamata, H. Akimune, T. Kondo, O. Itoh, C. Iwamoto, T. Yamagata, H. Toyokawa, Y.-W. Lui, H. Harada, F. Kitatani, S. Goko, S. Hilaire, and A. J. Koning, Phys. Rev. C **84** (2011) 055805.

[122] M. Goldhaber and E. Teller, Phys. Rev. **74** (1948) 1046.

[123] H. Steinwedel, J. H. D. Jensen, and P. Jensen, Phys. Rev. **79** (1950) 1019.

[124] V. V. Varlamov, B. S. Ishkhanov, V. N. Orlin, and V. A. Chetvertkova, Bull. Rus. Acad. Sci. **74** (2010) 833.

[125] J. R. Beene, F. E. Bertrand, D. J. Horen, R. L. Auble, B. L. Burks, J. Gomez del Campo, M. L. Halbert, R. O. Sayer, W. Mittig, Y. Schutz, J. Barrette, N. Alamanos, F. Auger, B. Fernandez, A. Gillibert, B. Haas, and J. P. Vivien, Phys. Rev. C **41** (1990) 920.

[126] B. Özel-Tashenov, J. Enders, H. Lenske, A. M. Krumbholz, E. Litvinova, P. von Neumann-Cosel, I. Poltoratska, A. Richter, G. Rusev, D. Savran, and N. Tsoneva, Phys. Rev. C **90** (2014) 024304.

[127] K. Govaert, F. Bauwens, J. Bryssinck, D. De Frenne, E. Jacobs, W. Mondelaers, L. Govor, and V. Y. Ponomarev, Phys. Rev. C **57** (1998) 2229.

[128] R. Schwengner, G. Rusev, N. Benouaret, R. Beyer, M. Erhard, E. Grosse, A. R. Junghans, J. Klug, K. Kosev, L. Kostov, C. Nair, N. Nankov, K. D. Schilling, and A. Wagner, Phys. Rev. C **76** (2007) 034321.

[129] D. Savran, M. Fritzsche, J. Hasper, K. Lindenberg, S. Müller, V. Y. Ponomarev, K. Sonnabend, and A. Zilges, Phys. Rev. Lett. **100** (2008) 232501.

[130] J. Isaak, D. Savran, M. Krtička, M. Ahmed, J. Beller, E. Fiori, J. Glorius, J. Kelley, B. Löher, N. Pietralla, C. Romig, G. Rusev, M. Scheck, L. Schnorrenberger, J. Silva, K. Sonnabend, A. Tonchev, W. Tornow, H. Weller, and M. Zweidinger, Phys. Lett. B **727** (2013) 361 .

[131] B. Löher, D. Savran, T. Aumann, J. Beller, M. Bhike, N. Cooper, V. Derya, M. Duchêne, J. Endres, A. Hennig, P. Humby, J. Isaak, J. Kelley, M. Knörzer, N. Pietralla, V. Ponomarev, C. Romig, M. Scheck, H. Scheit, J. Silva, A. Tonchev, W. Tornow, F. Wamers, H. Weller, V. Werner, and A. Zilges, Phys. Lett. B **756** (2016) 72 .

[132] O. Bohigas, N. V. Giai, and D. Vautherin, Phys. Lett. B **102** (1981) 105 .

[133] A. Leprêtre, H. Beil, R. Bergère, P. Carlos, J. Fagot, A. D. Miniac, and A. Veyssière, Nucl. Phys. A **367** (1981) 237 .

[134] The QRPA calculations were kindly provided by V. Y. Ponomarev.

[135] A. Tamii, I. Poltoratska, P. von Neumann-Cosel, Y. Fujita, T. Adachi, C. A. Bertulani, J. Carter, M. Dozono, H. Fujita, K. Fujita, K. Hatanaka, D. Ishikawa, M. Itoh, T. Kawabata, Y. Kalmykov, A. M. Krumbholz, E. Litvinova, H. Matsubara, K. Nakanishi, R. Neveling, H. Okamura, H. J. Ong, B. Özel-Tashenov, V. Y. Ponomarev, A. Richter, B. Rubio, H. Sakaguchi, Y. Sakemi, Y. Sasamoto, Y. Shimbara *et al.*, Phys. Rev. Lett. **107** (2011) 062502.

[136] K. Schelhaas, J. Henneberg, M. Sanzone-Arenhövel, N. Wieloch-Laufenberg, U. Zurmühl, B. Ziegler, M. Schumacher, and F. Wolf, Nucl. Phys. A **489** (1988) 189 .

[137] D. M. Rossi, P. Adrich, F. Aksouh, H. Alvarez-Pol, T. Aumann, J. Benlliure, M. Böhmer, K. Boretzky, E. Casarejos, M. Chartier, A. Chatillon, D. Cortina-Gil, U. Datta Pramanik, H. Emling, O. Ershova, B. Fernandez-Dominguez, H. Geissel, M. Gorska, M. Heil, H. T. Johansson, A. Junghans, A. Kelic-Heil, O. Kiselev, A. Klimkiewicz, J. V. Kratz, R. Krücken, N. Kurz, M. Labiche, T. Le Bleis, R. Lemmon *et al.*, Phys. Rev. Lett. **111** (2013) 242503.

[138] M. Bender, P.-H. Heenen, and P.-G. Reinhard, Rev. Mod. Phys. **75** (2003) 121.

[139] J. Erler and P.-G. Reinhard, J. Phys. G **42** (2015) 034026.

[140] B. K. Agrawal, S. Shlomo, and V. K. Au, Phys. Rev. C **72** (2005) 014310.

[141] C. Mondal, B. K. Agrawal, M. Centelles, G. Colò, X. Roca-Maza, N. Paar, X. Viñas, S. K. Singh, and S. K. Patra, Phys. Rev. C **93** (2016) 064303.

[142] G. A. Lalazissis, T. Nikšić, D. Vretenar, and P. Ring, Phys. Rev. C **71** (2005) 024312.

[143] A. B. Migdal, J. Exp. Theor. Phys. USSR **15** (1945) 81.

[144] The model calculations were kindly provided by X. Roca-Maza.

[145] J. H. Birkhan, *Elektrische Dipol-Polarisierbarkeit und Spin-M1-Stärke aus ^{48}Ca(p,p')-Daten unter 0°*, Doctoral thesis D17, TU Darmstadt (2015).

[146] J. Birkhan, H. Matsubara, P. von Neumann-Cosel, N. Pietralla, V. Y. Ponomarev, A. Richter, A. Tamii, and J. Wambach, Phys. Rev. C **93** (2016) 041302.

[147] M. Sasano, H. Sakai, K. Yako, T. Wakasa, S. Asaji, K. Fujita, Y. Fujita, M. B. Greenfield, Y. Hagihara, K. Hatanaka, T. Kawabata, H. Kuboki, Y. Maeda, H. Okamura, T. Saito, Y. Sakemi, K. Sekiguchi, Y. Shimizu, Y. Takahashi, Y. Tameshige, and A. Tamii, Phys. Rev. C **79** (2009) 024602.

[148] *The NIST Reference on Constants, Units, and Uncertainty*, https://physics.nist.gov/cuu/Constants/index.html, accessed: 23.08.2019.

[149] R. Capote, M. Herman, P. Obložinský, P. Young, S. Goriely, T. Belgya, A. Ignatyuk, A. Koning, S. Hilaire, V. Plujko, M. Avrigeanu, O. Bersillon, M. Chadwick, T. Fukahori, Z. Ge, Y. Han, S. Kailas, J. Kopecky, V. Maslov, G. Reffo, M. Sin, E. Soukhovitskii, and P. Talou, Nucl. Data Sheets **110** (2009) 3107 , Special Issue on Nuclear Reaction Data.

[150] U. Agvaanluvsan, A. C. Larsen, M. Guttormsen, R. Chankova, G. E. Mitchell, A. Schiller, S. Siem, and A. Voinov, Phys. Rev. C **79** (2009) 014320.

[151] H. K. Toft, A. C. Larsen, U. Agvaanluvsan, A. Bürger, M. Guttormsen, G. E. Mitchell, H. T. Nyhus, A. Schiller, S. Siem, N. U. H. Syed, and A. Voinov, Phys. Rev. C **81** (2010) 064311.

[152] H. K. Toft, A. C. Larsen, A. Bürger, M. Guttormsen, A. Görgen, H. T. Nyhus, T. Renstrøm, S. Siem, G. M. Tveten, and A. Voinov, Phys. Rev. C **83** (2011) 044320.

[153] S. Müller, F. Beck, D. Meuer, and A. Richter, Phys. Lett. B **113** (1982) 362 .

[154] G. Kilgus, G. Kühner, S. Müller, A. Richter, and W. Knüpfer, Z. Phys. A **326** (1987) 41.

[155] J. Enders, N. Huxel, P. von Neumann-Cosel, and A. Richter, Phys. Rev. Lett. **79** (1997) 2010.

[156] J. Enders, N. Huxel, U. Kneissl, P. von Neumann-Cosel, H. H. Pitz, and A. Richter, Phys. Rev. C **57** (1998) 996.

[157] I. Poltoratska, R. W. Fearick, A. M. Krumbholz, E. Litvinova, H. Matsubara, P. von Neumann-Cosel, V. Y. Ponomarev, A. Richter, and A. Tamii, Phys. Rev. C **89** (2014) 054322.

[158] S. Bassauer, P. von Neumann-Cosel, and A. Tamii, Phys. Rev. C **94** (2016) 054313.

[159] S. Bassauer, P. von Neumann-Cosel, and A. Tamii, EPJ Web Conf. **178** (2018) 03008.

[160] C. E. Porter and R. G. Thomas, Phys. Rev. **104** (1956) 483.

[161] T. Ericson, Adv. Phys. **9** (1960) 425.

[162] B. Reitz, *Weiterentwicklung des Detektorsystems am QCLAM–Spektrometer des S–DALINAC und Untersuchung der Reaktionen ^{48}Ca(e,e') und ^{58}Ni(e,e') unter 180°*, Doctoral thesis D17, TU Darmstadt (2000).

[163] E. P. Wigner, *Results and theory of resonance absorption*, Oak Ridge Natl. Lab. Rept. ORNL-2309 (1957).

[164] R. U. Haq, A. Pandey, and O. Bohigas, Phys. Rev. Lett. **48** (1982) 1086.

[165] S. Müller, *Untersuchung transversaler elektrischer Dipolanregungen in ^{90}Zr und Bestimmung von Protonen und Neutronen Spin-Flip Amplituden in der Anregung des $J^\pi = 1^+$ Zustands bei $E_x = 5.846$ MeV in ^{208}Pb mit unelastischer Elektronenstreuung* (1983), Doctoral thesis D17, TH Darmstadt (1983).

[166] N. Huxel, *Die Scissors Mode in Kernen der Seltenen Erden mit ungerader Massenzahl*, Doctoral thesis D17, TU Darmstadt (1997).

[167] T. Rauscher, F.-K. Thielemann, and K.-L. Kratz, Phys. Rev. C **56** (1997) 1613.

[168] S. Goriely, S. Hilaire, and A. J. Koning, Phys. Rev. C **78** (2008) 064307.

[169] GSI Experiment S412, spokepersons T. Aumann and K. Boretzky.

[170] K. Lindenberg, *Development and Construction of the Low-Energy Photon Tagger NEPTUN*, Doctoral thesis D17, TU Darmstadt (2008).

[171] J. Ahrens, H. Borchert, K. Czock, H. Eppler, H. Gimm, H. Gundrum, M. Kröning, P. Riehn, G. S. Ram, A. Zieger, and B. Ziegler, Nucl. Phys. A **251** (1975) 479 .

[172] S. Hashimoto, Y. Shoji, Y. Fukuda, S. Miyamoto, M. Niibe, and A. Ando, in *PACS2001. Proceedings of the 2001 Particle Accelerator Conference (Cat. No.01CH37268)*, volume 4, pages 2692–2694.

Danksagung

An dieser Stelle möchte ich mich sehr herzlich bei allen bedanken, die mich bei der Anfertigung dieser Arbeit unterstützt und mir mit Rat und Tat beiseite gestanden haben.

Zuallererst möchte ich mich bei Prof. Dr. Peter von Neumann-Cosel bedanken, der mir die Gelegenheit gab an diesem interessanten Thema zu arbeiten und mir stets für Fragen und Diskussionen zur Verfügung stand. Außerdem bin ich ihm dankbar für die vielen Möglichkeiten an diversen Konferenzen und Tagungen teilnehmen zu dürfen, wo ich meine Forschungsergebnisse vor internationalem Publikum präsentieren konnte.

Ich danke Prof. Dr. Thomas Aumann, der sich freundlicherweise bereit erklärt hat das Korreferat zu übernehmen.

I would like to thank all participants of the experimental campaigns E421 and E422. Without their help and commitment it would have been impossible to perform the proton scattering experiments. I would like to thank especially Prof. Dr. Atsushi Tamii with whom I had many helpful discussions and whose comments concerning the data analysis were indispensable. I would like to thank Prof. Dr. Yoshitaka Fujita who helped me a lot with the preparation of the tin targets. I am also particularly thankful to Prof. Dr. Nobuyuki Kobayashi for his commitment to the realisation of the experiments.

Furthermore, I am thankful to Prof. Dr. Carlos Bertulani for very helpful discussions and for providing me his code on the equivalent photon method.

I would also like to thank Prof. Dr. Xavier Roca-Maza who provided me with the model calculations for the dipole polarisability.

Ich danke auch Dr. Vladimir Ponomarev für die theoretischen Rechnungen und viele hilfreiche Diskussionen.

Insbesondere danke ich auch Dr. Andreas Krugmann für die vielen anregenden Diskussionen rund um die Protonenstreuung.

Ich danke auch Dr. Johann Isaak für viele fruchtbare Diskussionen.

Ich möchte mich bei meinen Bürokollegen M.Sc. Maxim Singer, M.Sc. Antonio D'Alessio, B.Sc. Isabelle Brandherm und B.Sc. Maximilian Spall ganz herzlich für das angenehme Arbeit-

sklima bedanken.

Für das Korrekturlesen dieser Arbeit möchte ich mich bei M.Sc. Antonio D'Alessio, B.Sc. Isabelle Brandherm, M.Sc. Gerhart Steinhilber und M.Sc. Tobias Klaus bedanken.

Für die täglichen entspannten Kaffee- und Kartenrunden bedanke ich mich bei M.Sc. Tobias Klaus, M.Sc. Ilja Homm und M.Sc. Markus Wunderle.

Schließlich möchte ich mich bei meiner Familie bedanken. Ohne die stetige Unterstützung meiner Eltern Nikolai Bassauer und Valentina Bassauer, sowie meines Bruders B.Sc. Eugen Bassauer wäre diese Arbeit nicht möglich gewesen.

Publications

1. **S. Bassauer**, P. von Neumann-Cosel and A. Tamii, Phys. Rev. C **94** (2016)
2. C. Kremer, S. Aslanidou, **S. Bassauer**, A. Krugmann, N. Pietralla, V. Ponomarev, M. Singer, P. von Neumann-Cosel and M. Zweidinger, Conf. Series **724** (2016)
3. C. Kremer, S. Aslanidou, **S. Bassauer**, M. Hilcker, A. Krugmann, P. von Neumann-Cosel, T. Otsuka, N. Pietralla, V. Yu. Ponomarev, N. Shimizu, M. Singer, G. Steinhilber, T. Togashi, Y. Tsunoda, V. Werner and M. Zweidinger, Phys. Rev. Lett. **117** (2016)
4. P. von Neumann-Cosel, **S. Bassauer** and D. Martin, JPS Conf. Proc. **14** (2017)
5. **S. Bassauer**, P. von Neumann-Cosel and A. Tamii, EPJ Web Conf. **146** (2017)
6. J. Birkhan, M. Miorelli, S. Bacca, **S. Bassauer**, C. A. Bertulani, G. Hagen, H. Matsubara, P. von Neumann-Cosel, T. Papenbrock, N. Pietralla, V. Yu. Ponomarev, A. Richter, A. Schwenk and A. Tamii, Phys. Rev. Lett. **118** (2017)
7. D. Martin, P. von Neumann-Cosel, A. Tamii, N. Aoi, **S. Bassauer**, C. A. Bertulani, J. Carter, L. Donaldson, H. Fujita, Y. Fujita, T. Hashimoto, K. Hatanaka, T. Ito, A. Krugmann, B. Liu, Y. Maeda, K. Miki, R. Neveling, N. Pietralla, I. Poltoratska, V. Yu. Ponomarev, A. Richter, T. Shima, T. Yamamoto and M. Zweidinger, Phys. Rev. Lett. **119** (2017)
8. **S. Bassauer**, P. von Neumann-Cosel and A. Tamii, EPJ Web Conf. **178** (2018)
9. P. von Neumann-Cosel, **S. Bassauer**, D. Martin and A. Tamii, EPJ Web Conf. **178** (2018)
10. F. C. L. Crespi, A. Bracco, A. Tamii, N. Blasi, F. Camera, O. Wieland, N. Aoi, D. Balabanski, **S. Bassauer**, A. S. Brown, M. P. Carpenter, J. J. Carroll, M. Ciemala, A. Czeszumska, P. J. Davies, L. Donaldson, Y. Fang, H. Fujita, G. Gey, T. H. Hoang, N. Ichige, E. Ideguchi, A. Inoue, J. Isaak, C. Iwamoto, D. G. Jenkins, O. H. Jin, T. Klaus, N. Kobayashi, T. Koike, M. Krzysiek, M. Kumar Raju, M. Liu, A. Maj, D. Montanari, L. Morris, S. Noji, S. G. Pickstone, D. Savran, M. Spieker, G. Steinhilber, C. Sullivan, B. Wasilewska, V. Werner, T. Yamamoto, Y. Yamamoto, X. Zhou and S. Zhu, Journal of Physics: Conf. Series **1014** (2018)